DISCLAIMER

SANDIA REPORT
SAND2025-06637
Printed May 2025

Sandia National Laboratories

Development and Validation of Dense Discrete Phase Flow Models for Concentrating Solar Power Particle Receivers

Brantley H. Mills
Eldwin Djajadiwinata
Rageh Saeed
Flint Pierce
Hany Al-Ansary
Nader S. Saleh

Prepared by
Sandia National Laboratories
Albuquerque, New Mexico
87185 and Livermore,
California 94550

Issued by Sandia National Laboratories, operated for the United States Department of Energy by National Technology & Engineering Solutions of Sandia, LLC.

Available to DOE and DOE contractors from
U.S. Department of Energy
Office of Scientific and Technical Information
P.O. Box 62
Oak Ridge, TN 37831

Telephone: (865) 576-8401
Facsimile: (865) 576-5728
E-Mail: reports@osti.gov
Online ordering: http://www.osti.gov/scitech

Available to the public from
U.S. Department of Commerce
National Technical Information Service
5301 Shawnee Rd
Alexandria, VA 22312

Telephone: (800) 553-6847
Facsimile: (703) 605-6900
E-Mail: orders@ntis.gov
Online order: https://classic.ntis.gov/help/order-methods/

ABSTRACT

This report summarizes a recent project aimed at developing and validating the necessary tools to enable more accurate modeling of denser and more complex particle flows in next-generation particle receivers used in concentrating solar power towers. A newly developed CFD/DEM simulation capability was created by coupling existing the modeling and simulation tools Sierra and LAMMPS. This new capability permitted the inclusion of additional physics for particle drag and particle collisions to model complex flow features expected in next generation receivers. Two verification tests were executed to evaluate the new modeling capability: a test to ensure conservation of momentum after particle collisions and a test to ensure appropriate qualitative behavior in two closely interacting particles with drag (a modified drafting-kissing-tumbling problem). A model sensitivity study was executed with the new capability to assess the impact of the uncertainty in DEM model parameters with quantities of interest (QoI) for an obstructed flow particle receiver: particle velocity after an obstruction and particle curtain opacity. An experimental campaign was undertaken to measure the relevant QoI for an obstructed flow particle receiver that could be leveraged for validation of the modeling capability. Models of these experiments were created using the new simulation capability and evaluated using the measured QoI. Two commercial modeling capabilities were also evaluated for this application space using the ANSYS® code suite.

ACKNOWLEDGEMENTS

I would like to sincerely thank my co-authors for all their contributions to this report. Flint Pierce provided much needed guidance on the project direction and led the development of the new modeling capability. Rageh Saeed and Eldwin Djajadiwinata lead the experimental campaign and evaluated commercial modeling capabilities. Hany Al-Ansary provided much needed expertise and guidance on the project.

I would also like to extend my thanks to the business team at Sandia including Roberta Gonzalez and Letty Bermudez. Without their help, this project would not have been possible.

Thanks also goes out to the project managers at the Solar Energy Technology Office (SETO) at the Department of Energy (DOE). This includes Kamala Raghavan (lead project manager), Rajgopal Vijaykumar, and Matt Bauer. They provided much needed guidance throughout the project.

Finally, I would like to extend my thanks to Chris Bowen who provided valuable feedback about the technical content.

CONTENTS

LIST OF FIGURES

LIST OF TABLES

This page left blank

ACRONYMS AND TERMS

Acronym/Term	Definition
CFD	Computational Fluid Dynamics
CoM	Conservation of Momentum
CoR	Coefficient of Restitution
CSP	Concentrating Solar Power
DEM	Discrete Element Method
DoE	Design of Experiments
DKT	Drafting, Kissing, and Tumbling
DO	Discrete Ordinates
FLD	Fast Lubrication Dynamics
FPL	Friction Packing Limit
FPR	Falling Particle Receiver
KSU	King Saud University
LAMMPS	Large-scale Atomic/Molecular Massively Parallel Simulator
PHR	Particle Heating Receiver
PIEP	Pairwise Interaction Extended Point-particle
PP	Perforated Plate
PPP	Perforated Plate (parallel holes)
PPS	Perforate Plate (staggered holes)
QoI	Quantity of Interest
RANS	Reynolds-averaged Navier Stokes
ROM	Reduced Order Model
SOAR	Static Angle of Repose
SC	Specularity Coefficient
SDL	Standard Drag Law
TFM	Two Fluid Model
WM	Wire Mesh

This page left blank

1. INTRODUCTION

With the continued focus on the particle pathway for third-generation (Gen3) concentrating solar power (CSP) technology [1], additional importance is placed on the ability to accurately model particle flows in particle-based CSP components. A critical component contributing to the success of future utility-scale CSP particle plants targeting a levelized cost of electricity (LCOE) of $0.05/kWh is the particle receiver and its thermal performance [2]. Falling particle receivers (FPRs) are a leading contender for receiver designs, and modeling efforts of those designs have historically leveraged low particle volume fractions to simplify the physics. However, the latest designs for FPRs, such as those used in the Generation 3 Particle Pilot Plant (G3P3) project [3], feature obstructions in the flow path that slow the particle descent through the cavity and increase particle volume fractions, violating previous modeling assumptions. This report summarizes a recent project aimed at developing and validating the necessary tools to enable more accurate modeling of these denser and more complex particle flows in next-generation receivers.

The G3P3 project uses particle obstructions in the FPR design for the G3P3-USA system [4] to be built at Sandia National Laboratories (Sandia) and in the sister G3P3-KSA system [5] to be built in Saudi Arabia. While both systems obstruct the falling particles in the receiver cavity, each design uses a different technique. The G3P3-USA FPR uses discrete catch-and-release particle troughs (also referred to as a multistage design), and the G3P3-KSA FPR uses an obstructed flow concept with periodic ceramic impediments (c.f. Figure 1). Both of these approaches necessitated additional physical models over traditional modeling strategies [4, 6] to ensure adequate treatment of the particle drag and particle-to-particle collisions. New constitutive relationships and modeling approaches for these additional physics have been identified in the literature and were implemented into existing high-performance computing (HPC) simulation capabilities at Sandia. However, in addition to implementation, these new modeling strategies necessitated validation to confirm their applicability and accuracy.

Figure 1. Multistage particle trough obstruction (left; G3P3-USA) and the perforated plate obstruction (right; G3P3-KSA)

Sandia and King Saud University (KSU) were uniquely positioned to build the necessary modeling capability and collect the requisite validation evidence for these receiver concepts. Sandia's in-house HPC simulation capabilities (i.e., the SIERRA code suite) have been leveraged during the development of G3P3-USA to predict the thermal performance of the FPR design. With direct

access to the source code, the new modeling capabilities for dense particulate flow were integrated into these existing simulation capabilities. Likewise experimental facilities existed for obstructed flow receivers at KSU that significantly minimized the expense of collecting validation data. Specifically, KSU's facility featured a continuous circulating particle loop with an integrated particle image velocimetry (PIV) system to measure instantaneous particle velocities. Additionally, the facility also included a receiver test section using a translucent back wall suitable for measuring the particle curtain opacity. These metrics were important values that affect an FPR's thermal performance making them well suited for validating models.

Various modeling strategies exist to predict the thermal performance of falling particle receivers. A method that frequently appears in the literature [4, 6] utilizes a discrete particle framework tightly coupled with an air continuum referred to as a Lagrangian/Eulerian approach. This method is often coupled with a discrete-ordinates (DO) or Monte Carlo (MC) radiation model to also simulate the concentrated solar irradiation from the heliostat field and thermal radiation from the receiver walls to the environment. By taking advantage of the low volume fractions in traditional FPRs, various physical interactions between the particles have been historically omitted reducing the computational expense and complexity. However, with the inclusion of particle obstructions in new FPR designs creating denser particulate flow regions, these simplifications were no longer applicable. Figure 2 depicts the various physics necessary to appropriately model flows in next-generation particle receivers highlighting the two key areas of additional physics in red that were needed in present simulation capabilities for denser particle flows.

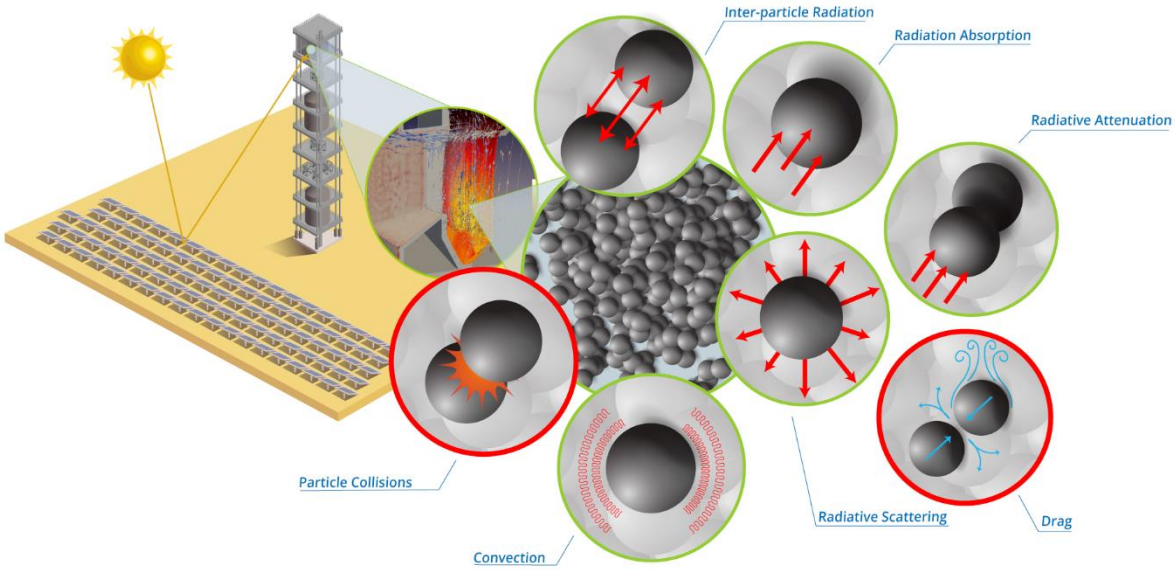

Figure 2. Depiction of the relevant particle physics in next-generation FPRs. Improved physics to be incorporated into HPC codes are highlighted in red circles.

New constitutive relationships and modeling approaches for particle drag and particle-to-particle collisions were implemented within the SIERRA codebase to simulate appropriate particle dynamics in the first phase of this project. First, an open-source molecular dynamics code developed at Sandia called the Large-scale Atomic/Molecular Massively Parallel Simulator (LAMMPS) [7] was coupled to the existing low Mach number, computational fluid dynamics (CFD) package within SIERRA. Then, granular discrete element method (DEM) models within LAMMPS were applied to the Lagrangian

particles to capture the particle-to-particle collisions. This approach provided the most accurate collision model, capturing translation and rotation of individual particles including the frictional forces between them. Incorporating DEM-based collision models also enables more accurate treatment of collisions with the surfaces of the particle obstructions compared with simple elastic collision models. Additionally, fast lubrication dynamics (FLD) [8] models were superimposed on standard drag models for spherical particles approximating additional dissipative forces from close proximity particles within an interstitial fluid. After implementation of these new physical models, additional verification tests were performed, and a model sensitivity study was executed to evaluate the relevance of DEM parameters of quantities of interest (QoI) for this application.

Concurrently with the model development, KSU collected validation data for relevant obstructed flow receiver designs. Models of those experiments were then developed for subsequent model validation. The second phase of this project then attempted to validate the new modeling strategy using the experimental data targeting agreement with relevant particle parameters including the particle velocity (measured using PIV) and particle curtain opacity. Ultimately, a successfully validated model could be utilized to optimize the ceramic impediments of the G3P3-KSA obstructed flow receiver for features like obstruction spacing and pore size. Additionally, this project helped to strengthen an ongoing collaboration between the two G3P3 teams, helped to inform G3P3-KSA FPR design decisions, and provided a launching point for developing a modeling capability suitable for evaluating future commercial scale FPRs.

The remainder of this report is summarized as follows. First, a description of the modeling strategy is provided highlighting the relevant design decisions in the new capability. Solution verification activities are also documented to provide confidence in the implementation. Next, a model sensitivity study is described, and the results are analyzed to assess the relevance of different model inputs on the QoI. Then, the experimental validation campaign is described, and the results are summarized. Next, a model validation study that leverages the experimental data is presented evaluated against the above referenced QoI. A comparable commercial capability is also evaluated against the experimental data. Finally, the results of this study are summarized.

2. MODEL IMPLEMENTATION AND CODE VERIFICATION

2.1. Model Development Strategy

The Sandia-developed Sierra code suite [9] was selected to implement the identified array of physics necessary to accurately model next-generation particle receivers[1] including multistage features. Sierra was selected in this project primarily for the following reasons:

1. Recent history of particle receiver models developed using Sierra (indicative of the implementation many key physical models needed for particle receivers)
2. In-house development of Sierra at Sandia to enable rapid implementation of new models/physics
3. Sufficient computational resources available unencumbered by commercial licenses

Prior to implementing the present features, the limitations within Sierra that hindered modeling of the thermal performance of particle receivers with multistage features included the inability to accurately model transitory dense particle flows within the receiver. Particle-to-particle interactions (e.g. collisions) were largely ignored in most particle receiver models under the assumption that particle volume fractions were in the dilute regime (i.e. < 10%) [2]. This was mostly true for FPRs which also helped to minimize the computational expense. However, with multistage features in FPRs, this assumption no longer held, and dense particle flow interactions were considered. Previous modeling workarounds utilized reduced order models (ROMs) calibrated to experiments to simplify the physics [10], but this approach did not scale well[2] as particle receiver technology looked to commercialize.

Fuego, a submodule within Sierra, was leveraged to model the low-Mach number fluid dynamics for this problem. It enabled introducing Lagrangian particles and coupled with additional codes/submodules to incorporate radiation transport using discrete-ordinates (DO) models. These capabilities provided many of the critical physics required to predict the thermal performance of FPRs in the dilute particle regime, but as discussed, additional physics were needed for dense particle flows in two keys areas: particle-to-particle collisions and particle drag models in dense particle flows. Sierra/Fuego was enhanced in this project by:

1. coupling an established molecular dynamics code, LAMPPS, and
2. utilizing existing fast lubrication dynamics (FLD) models to more accurately model drag in dense flow regimes.

The Large-scale Atomic/Molecular Massively Parallel Simulator (LAMMPS) [3] is an open-source, molecular dynamics code actively developed at Sandia. It features a wide array of particle potentials, is highly parallelizable, and is an extremely mature code with a large user base. Coupling with Sierra provided immediate access to a wide range of verified particle-to-particle interaction strategies that were well suited for particle receivers. Additionally, integration of more sophisticated drag models was made easier within LAMMPS with the existing FLD models already available within the code. Finally, given that LAMMPS is an open-source code, development in this project was expected to be impactful for other CSP teams with similar particle-based modeling needs who would leverage the capability.

[1] While the particle receiver designs being explored in this report are variations of falling particle receiver concepts, these specific receivers are also referenced in the literature more generally as particle heating receivers (PHRs).
[2] Did not scale well in the sense that the ROM must be informed through experimentation and large-scale experiments were difficult and costly to execute.

As described above, previous modeling strategies for FPRs typically utilized isolated particle drag models whereby nearby particles have no direct impact on the particle's trajectory. This assumption worked well in the dilute particle phase (particle volume factions ≤ 10%) but tended to break down in denser particle flow regimes leading to over/underestimation of the drag forces experienced by a particle or particle parcel (one particle effectively representing > 1 particles). Under certain conditions, this approach was also observed to lead to numerical instabilities. Alternative, more sophisticated drag models exist that account for each particle's proximity to neighboring particles (beyond just volume fractions). One such model is the pairwise interaction extended point-particle (PIEP) model [11] which is informed with DNS simulations to more accurately capture complex particle arrangements. However, implementation of the PIEP model was not pursued in lieu of the already implemented pairwise FLD model available in LAMMPS. These models coupled well with existing granular models and captured much of the physics created by the interstitial fluid in collisions.

In summary, the chart in Figure 3 summarizes the previous model strategy and the changes implemented as part of this project using Sierra. LAMMPS was successfully integrated with Sierra/Fuego and replaced existing discrete particle models within Fuego (that didn't include particle-to-particle collisions). Integration of LAMMPS within Sierra was achieved through the use of a dynamic library. This concept enabled LAMMPS functionality to exist separately from the Sierra code base which was simply executed at the launch of Sierra. An advantage of this approach was that the LAMMPS features were more portable and agnostic to the code with which it is being coupled. A demonstration problem of three falling particles with initial colliding trajectories illustrated the new particle-to-particle interactions using LAMMPS in Figure 4.

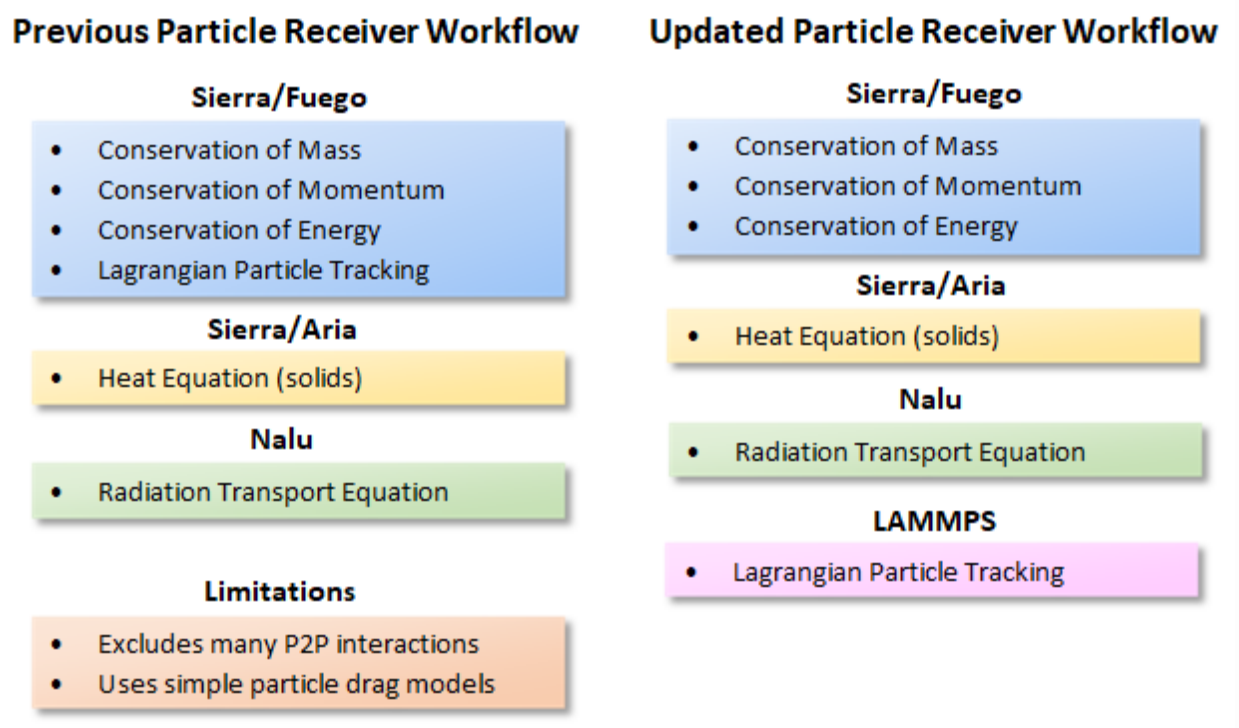

Figure 3. Previous (left) and new (right) particle receiver modeling strategy using Sierra

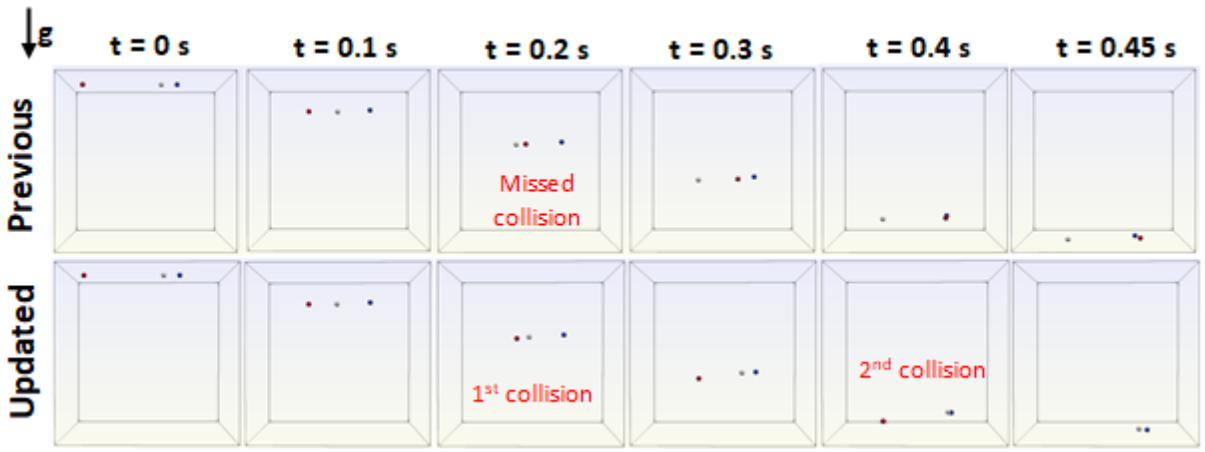

Figure 4. Three falling colliding particles without particle-to-particle collisions (top; previous model) and with particle-to-particle collisions (bottom; updated model)

2.2. M.1.1.2: Conservation of Momentum Verification Tests

In addition to various toy problems used to verify appropriate coupling between Sierra and LAMMPS, two more rigorous verification tests were defined as milestones in this project: the "drafting, kissing, tumbling" (DKT) verification test and a "conservation of momentum" (CoM) verification test. This section discusses the execution of the CoM test ensemble, summarized in Table 1, looking at a number of CoM-style problems to ensure momentum is properly handled in particle collisions. With each test, analytical solutions of the total momentum were available. Conservation of momentum was expected to be conserved within negligibly small values; therefore, the acceptance criteria being used in these tests required that the error in the momentum must be $< 1\times10^{-12}$.

Table 1. CoM Verification Test Summaries

Test Description	Error	Result
Head-on collision – Hard repulsion (CoR = 1)	$<1\times10^{-16}$	Passed
Head-on collision – Energy dissipation (CoR < 1)	$<1\times10^{-16}$	Passed
Glancing collision – Energy dissipation (CoR < 1)	$<1\times10^{-16}$	Passed
Multiple collisions – Energy dissipation (CoR < 1)	$<1\times10^{-12}$	Passed

It should be emphasized that each test also varied solution control parameters including the fluid time step and the number of particle sub-cycles (i.e. number of particle time steps for each fluid solve) in order to select reasonable bounds necessary to accurately simulate the solution. These parameters were carefully selected such that numerical artifacts were not introduced into the results while balancing the computational expense for large problems. Additionally, the physical particle parameters were selected to match relevant values for CSP applications (e.g. particle diameter of 350 μm). Note that any heat generated from particle-to-particle collisions was ignored in this model (i.e. not passed to the surrounding fluid) under the assumption that the generated heat was negligible for particle-based receivers.

2.3. M.1.1.1: DKT Verification Problem

The other verification test posed for this coupling included an evaluation of the Sierra-LAMMPS model using the "drafting, kissing, and tumbling" (DKT) problem [11]. This problem features two vertically stacked particles starting at rest being pulled by gravity within a fluid where the 'lagging' particle catches up to the 'leading' particle due to the reduced drag created by being in its wake. As the particles approach one another, a complex rolling mechanism occurs whereby the lagging particle overtakes the leading particle in the descent. The decision to move forward with the pairwise particle lubrication model (FLD) (superimposed with the standard drag law (SDL) over a sphere) to handle the more sophisticated drag interactions in dense phase flows in lieu of the more advanced pairwise interaction extended point-particle (PIEP) model was thought to have minimal impact on the accuracy of the solution. However, some limitations in the FLD+SDL model are apparent when exercised for this problem.

A key aspect of the DKT problem is the ability to model the reduced drag created for the lagging particle. However, as illustrated in [11], if only using the SDL, there is no mechanism to communicate the reduced drag to the lagging particle. The FLD model only superimposes a 'squeezing' mechanism to retard the velocity of two particles if their velocities are already different (i.e. they are already approaching one another) and in close enough proximity. Since they will fall at the same rate under the SDL model, the drag of the lagging particle is not captured. Implementing the PIEP model in future versions of this model framework would improve the response for this type of problem.

Despite this limitation, the DKT problem was still used in a modified form to qualitatively illustrate other key physics being captured by the SDL+FLD model. First, the lagging particle was given an initial velocity to ensure the applied lubrication forces would be exercised as the particles approached in proximity. Second, the leading particle was given a slight horizonal offset to ensure asymmetry in the collision. This verification test then looked for qualitative particle behaviors with increasing complexity of the lubrication forces and granular physics being applied. The qualitative solutions of the modified DKT problem are depicted in Figure 5.

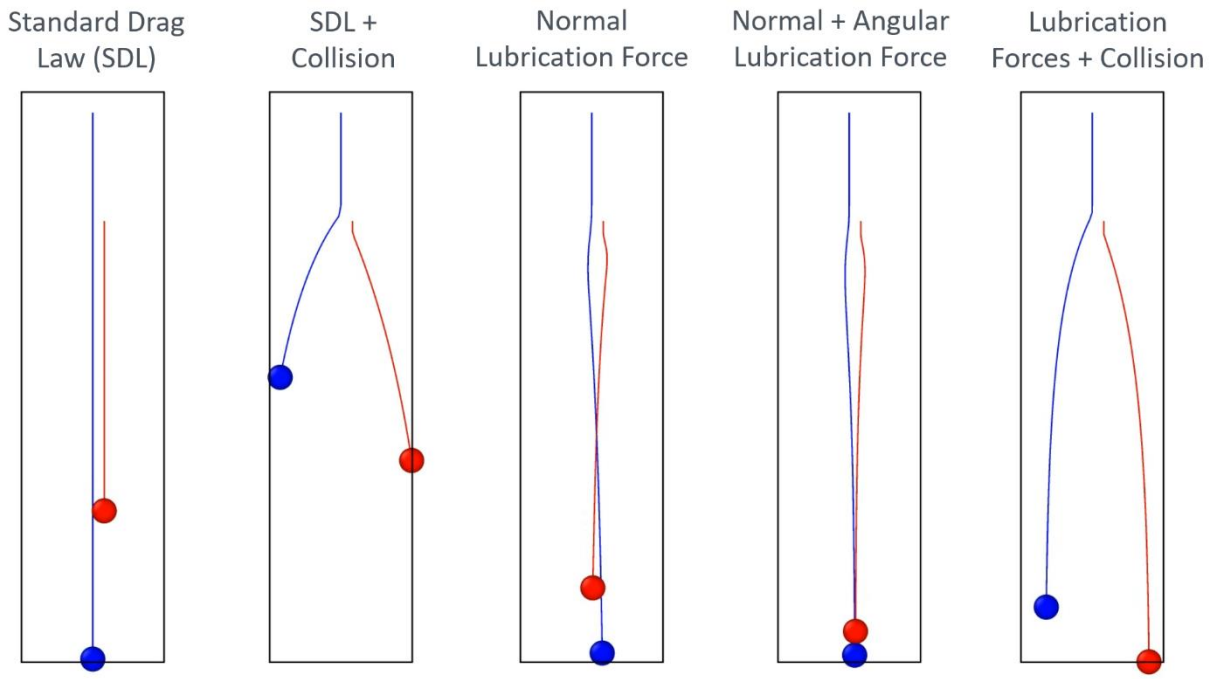

Figure 5. Particle trajectories in the modified DKT problem demonstrating the qualitative behavior of the different levels of physics

As shown in the figure, the first simulation (left) was the original Sierra capability using only the SDL without any particle-to-particle interactions. Next, granular particle-to-particle collisions were included akin to the demonstration problem in Figure 4. Then, the *normal* lubrication forces were included. Next, the normal and angular lubrication forces were included (angular in that they factor in the relative rotational speed of the particles). Finally, particle collisions were included with the full suite of lubrication forces.

With only the SDL and without collisions, the particles did not show any interaction and fell at rates commensurate with the SDL and their initial velocities. With the inclusion of normal lubrication forces, the particles experienced a "roll" as observed in the original DKT problem where the particles were pushed laterally from one another ('squeezing' the interstitial fluid). With angular lubrication forces, the lagging particle (blue) pulled the leading particle (red) in its trajectory as it passed. Finally, the full suite of physics showed lower lateral velocities after collision with the inclusion of lubrication forces (demonstrating decreased velocities from the interstitial fluid flowing back in between the particles after collision). Based on these observed qualitative behaviors, we assert that the FLD model was properly implemented in the model framework despite the limitations it provided in capturing the true physics. However, we asserted that despite these limitations it would be sufficient for this CSP application space.

3. MODEL SENSITIVITY STUDY

A model sensitivity study was executed using this new model framework to discern the effect of model inputs on the relevant QoI for this application space. The QoI defined for this study included: the particle velocity (both mean and standard deviation) after the particle obstruction (wire mesh or perforated plate) at different distances beyond the obstruction, and the particle curtain opacity at different 'windows' beyond the obstruction. For the particle velocity, individual particle velocities were averaged across the domain in 1 mm vertical windows. For the particle curtain opacity, the values were evaluated in 20 mm vertical windows. Both values were computed from 1 to 90 mm from the top surface of the obstruction for a total of 80 velocity values (mean and standard deviation) and 4 curtain opacity values. This is summarized Table 1. For this study, the selection of the distances beyond the obstruction were defined based on expectations of the capabilities for the eventual model validation experiments.

Table 1. Sensitivity Study Responses

Response	Increments	Total Responses
Particle Velocity (Mean) [m/s]	1 mm	89
Particle Velocity (Standard Deviation) [m/s]	1 mm	89
Curtain Opacity [-]	20 mm	4

The meshed computational domain for the model sensitivity study is depicted in Figure 6. The computational domain for the air continuum was 60 mm x 60 mm x 180 mm. A total of 51,840 hexahedral elements were utilized. A perforated plate (PP) spanning the length and width of the domain was selected for this study using a staggered hole arrangement (PPS). The holes were 10 mm in diameter and the center-to-center distance was 15 mm. The PP was constructed using static particles with 1 mm diameter. A key advantage of this technique was that the continuum mesh did not need to conform to the particle obstruction. This was critical design decision that likely helps the scalability of this modeling strategy to full particle receivers. The geometric parameters of the PP were not varied in this sensitivity study, but the importance of this effect could be evaluated in future studies. Instead, this study focused specifically on the granular properties of the falling

particles.

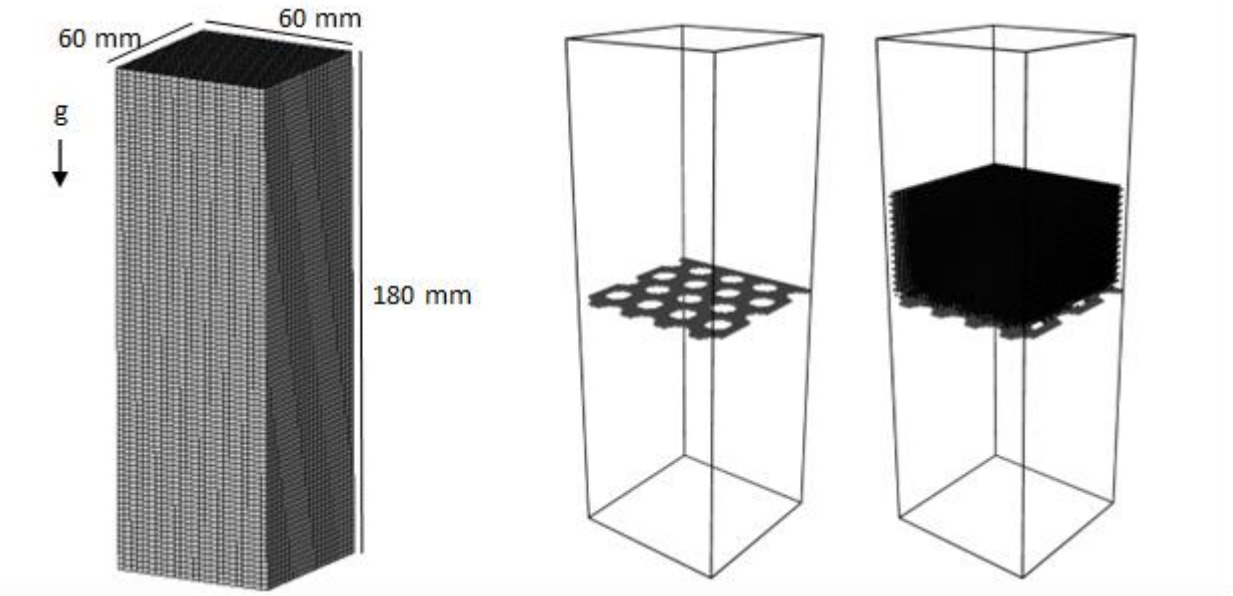

Figure 6. Meshed computational domain for the model sensitivity study (left) and a depiction of a perforated plate and particle initialization in the domain (right)

An array of moving CARBO HSP particles was initialized in the domain above the perforated plate as shown in Figure 6. A total of ~42,000 particles were initialized in a body-centered arrangement. The location of the particles in the first layer of the body-centered arrangement is randomized but was consistent for each sample in the sensitivity study. The particles were given a small initial downward velocity and allowed to approach a steady-state solution within 2 seconds of simulation time. Periodic boundary conditions were used such that particles that fall through the bottom of the domain were transported to the top of the domain. At the end of the simulation (2 s), the responses defined in Table 1 are computed.

Depictions of how each QoI in Table 1 is calculated are shown in Figure 7. Figure 7a highlights the 1 mm window below the perforated plate over which the mean and standard deviation of the particle velocity is computed. For the curtain opacity, the instantaneous particle positions and their pixelated spherical silhouettes at the end of the simulation are projected onto a pixelated backwall. Then, the fraction of backwall pixels obstructed by the particles is computed at the end of the simulation to arrive at the curtain opacity. A visualization of this method being applied is depicted in Figure 7b.

As described in more detail later in this report, experimental methods to calculate the curtain opacity utilized still images of the particle curtain at a point in time against a high contrast background. The number of background pixels in the image covered by particles divided by the total number of pixels in the sample region is used to determine the curtain opacity. To be consistent with the experiments, curtain opacity is computed in the same manner computationally based on the particle locations at the end of the transient simulation after having reached steady state. For the sensitivity study, each spherical particle is projected onto a pixelated surface of the x-plane and the number of pixels covered by the particles divided by the total number of pixels used determines the opacity. A sample visualization of this method is depicted in Figure 7 where purple depicts particles and yellow depicted the background.

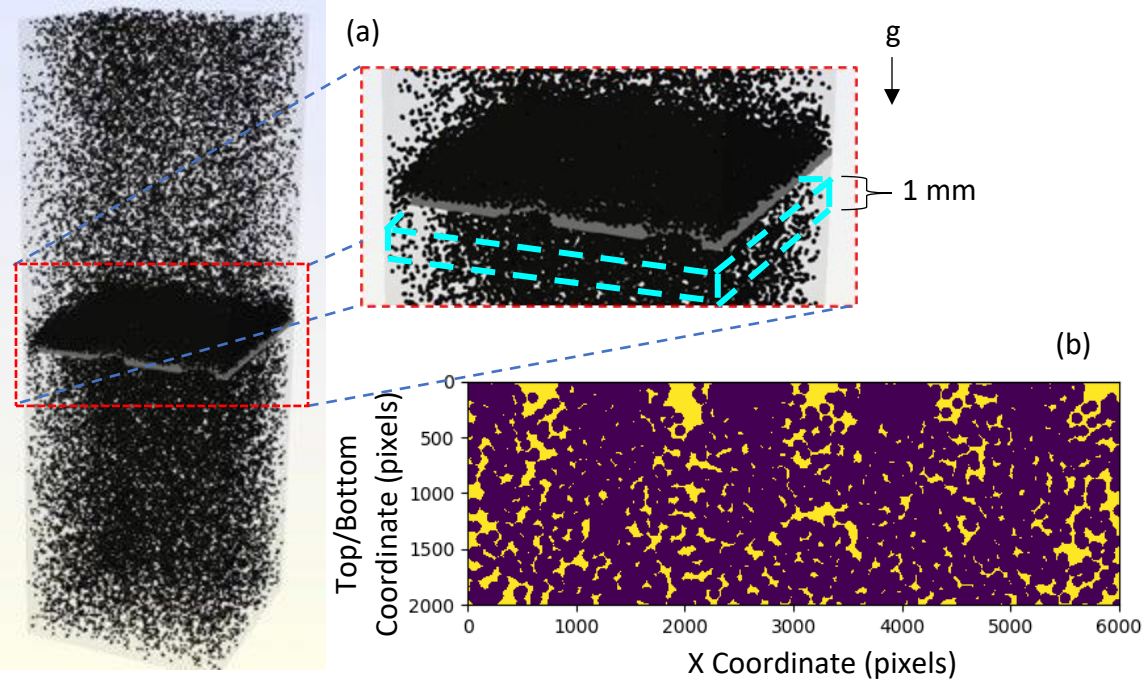

Figure 7. A 1 mm window below the obstruction over which the particle velocity is evaluated (a), and the projected particle positions perpendicular to gravity to visualize the calculation of the curtain opacity (b)

A granular flow model was implemented in LAMMPS using lessons learned from existing numerical and experimental studies on CARBO particles in dense discrete phase flows [12]. However, while this study and the model both used a Hertz based contact model, there were some differences in the granular formulation used here versus the methods described in Yarrington's thesis. More details about the full equation set are provided in Section 5.1 as to not be repetitive here; however, this study focused on granular model parameters used in those equations.

An incremental Latin hypercube sampling (LHS) method is used to vary a total of 18 variables in the study. Each variable, defined in Table 2 allowed to vary for each sample within the prescribed ranges with a uniform distribution. An *incremental* LHS study is performed to ensure that convergence is observed in the number of samples used in the study to assess the importance of each input in Table 2. 128 samples were needed to observe convergence in the results (shown below). Several snapshots from a sample in the sensitivity study are shown in Figure 8 at 0.025, 0.035, 0.07875, and 0.5 s into the simulation. Likewise, the particle velocity magnitude and curtain opacity at increasing distance from the perforate plate are plotted in Figure 9. As shown in the figure, the mean particle magnitude after the obstruction follows the theoretical kinematic equation without drag suggesting that the presence of the air is not significant at short distances. This effect has been observed previously [13]. Curtain opacity after the obstruction decreases rapidly from a peak value of ~0.98 shortly after the obstruction to ~0.92 between 60 to 80 mm after the obstruction.

Table 2. Model inputs varied in the sensitivity study. Initial value is listed in specified units and the min./max. values are fractional increments of the initial value.

Variable	Initial	Min.	Max.
Elastic Modulus E_{eff} (particles) [GPa]	113	0.9	1.1
Elastic Modulus E_{eff} (particle/plate) [GPa]	110	0.9	1.1

Normal Damping Coefficient η_{n0} (particles) [-]	1×10^{3}	0.2	5
Normal Damping Coefficient η_{n0} (particles/plate) [-]	1×10^{3}	0.2	5
Poisson Ratio ν (particles) [-]	0.28	0.96	1.04
Poisson Ratio ν (particles/plate) [-]	0.3	0.93	1.07
Tangential Damping Scaling x_η (particles) [-]	1.0	0.75	1.25
Tangential Damping Scaling x_η (particles/plate) [-]	1.0	0.75	1.25
Tangential Friction Coefficient μ_t (particles) [-]	0.53	0.75	1.25
Tangential Friction Coefficient μ_t (particles/plate) [-]	0.5	0.75	1.25
Rolling Stiffness Coefficient k_{roll} (particles) [-]	200	0.5	1.5
Rolling Stiffness Coefficient k_{roll} (particles/plate) [-]	200	0.5	1.5
Rolling Damping Coefficient γ_{roll} (particles) [-]	100	0.5	1.5
Rolling Damping Coefficient γ_{roll} (particles/plate) [-]	100	0.5	1.5
Rolling Friction Coefficient μ_{roll} (particles) [-]	0.37	0.75	1.25
Rolling Friction Coefficient μ_{roll} (particles/plate) [-]	0.41	0.75	1.25
Time Step [s]	5×10^{-7}	0.5	1.0
Air Viscosity μ [Pa-s]	184.6×10^{-7}	0.9	4.0

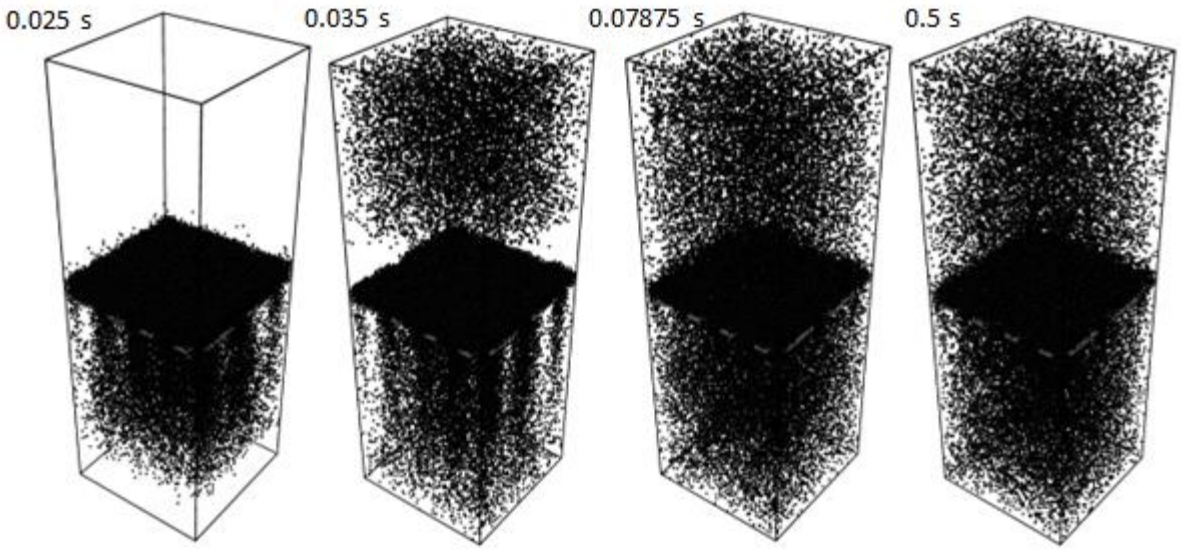

Figure 8. Snapshots from a sample in the study at 0.025, 0.035, 0.07875, and 0.5 s

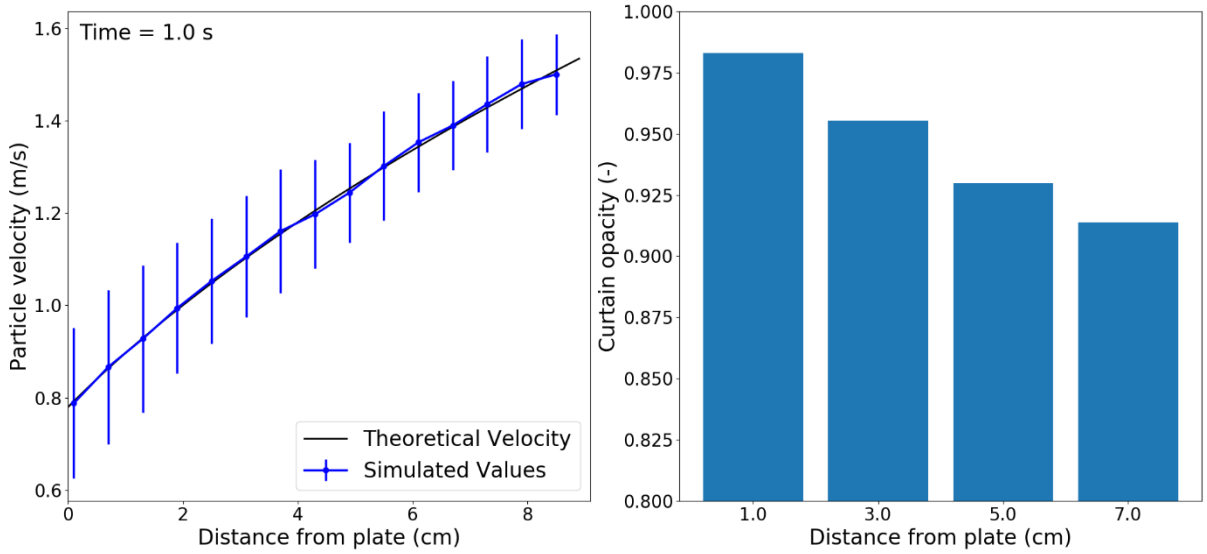

Figure 9. Simulated particle velocity compared with theoretical values (left) and the curtain opacity after the perforated plate (right)

Pearson correlation coefficients are computed from the study to quantify the relationship between the relevant QoI (Table 1) and varied model inputs (Table 2). A Pearson correlation coefficient is a measure of the strength and direction of the relationship between the QoI and the model input normalized to values between -1 and 1. A subset of the results are plotted in Figure 10 with an increasing number of samples used in the study to show convergence. As shown, each plot shows reasonable convergence with an increasing number of samples up to 128. A relatively large number of samples were required as the relationship between model inputs and QoI was found to be very weak. Ultimately, none of the model inputs showed a strong relationship (usually defined by correlation coefficients < -0.4 or > 0.4) suggesting that critical QoI are not significantly dependent on the DEM model parameters. For the particle velocity, the most relevant values included friction coefficients, and for the curtain opacity, values related to the rolling model proved to be the most relevant. It should be emphasized, that while the particle velocity magnitude and curtain opacity are weakly related to the granular model, particle trajectories are expected to be more sensitive and are the subject of future work.

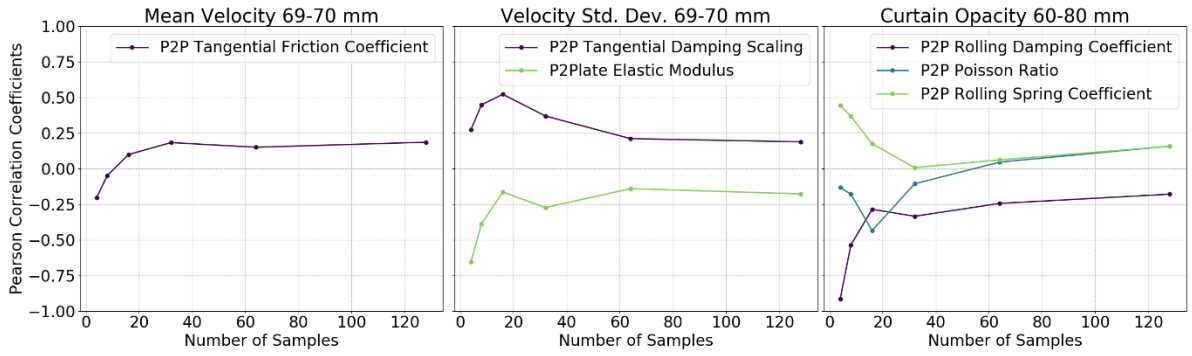

Figure 10. Pearson correlation coefficients for the mean particle velocity (left), standard deviation of the particle velocity (center), and the curtain opacity (right) after the perforated plate.

4. MODEL VALIDATION EXPERIMENTS

To provide more confidence that the new model framework was well suited for particle-based CSP, a validation campaign was executed using an obstructed flow particle receiver concept for the candidate application space. Specifically, the obstructed flow particle heating receiver (OF-PHR) design being leveraged at KSU was adopted. An experiment setup was designed and assembled leveraging existing experimental facilities to measure relevant particle QoIs including the particle velocity and particle curtain opacity that affect particle receiver thermal performance. Models of these experiments were then constructed to evaluate the model.

As described below in more detail, these experiments of an obstructed-flow particle heating receiver (OF-PHR) used only a single obstruction to simplify the number of relevant variables for better quality validation data. However, validation of the complex physics for even a single stage OF-PHR was assumed to be sufficient to a full-scale OF-PHR and for other obstructed flow receiver designs like the multistage FPR used at Sandia.

4.1. Test Setup

The test setup is depicted in Figure 11 and Figure 12. It was composed of two main components: a particle-handling unit and a particle heating receiver (PHR). The particle-handling unit was responsible for delivering particles to the PHR and then collecting the particles that left the PHR. The PHR, located just below the particle feeder, consists of (1) a lightly painted white acrylic board as its base and (2) an obstruction made of stainless-steel perforated plate or wire mesh that is attached to the board. CARBOBEAD HSP particles were used in the experiment with a nominal diameter of 300 μm.

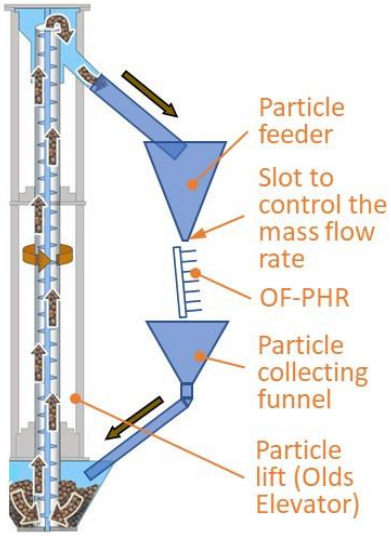

Figure 11. Schematic diagram of the test setup at KSU.

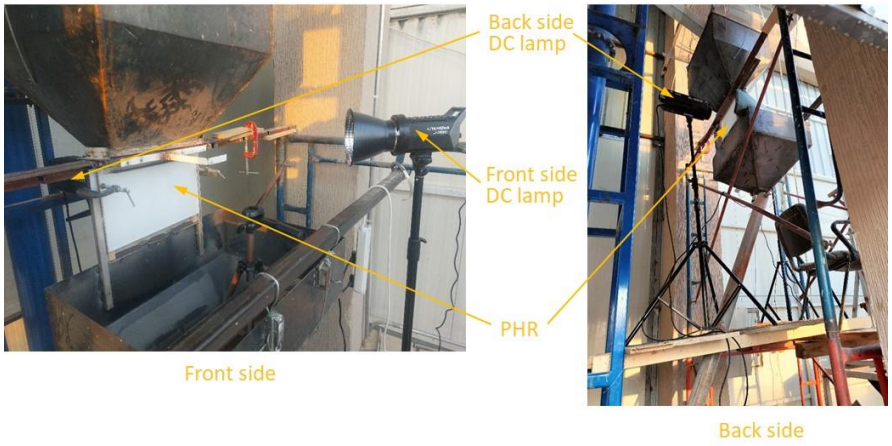

Figure 12. Test setup along with the DC lamps at the front and behind the PHR. These lamps are for particle velocity and curtain opacity measurements.

The acrylic board was lightly painted white to be semi-transparent (translucent). This was done to ensure that a lighting source behind the board would be sufficiently diffused to enable adequate particle curtain opacity measurements, which is explained in more detail below. The tilt angle of the whole PHR was adjustable to allow for tests at different angles with respect to gravity (up to 7° was used in this experimental campaign). The board of the PHR was 200 mm and 300 mm in height and length, respectively. It was grooved to facilitate insertion of various kinds of obstructions to be tested as shown Figure 13a where an obstruction has been installed on the groove. Two types of obstruction were tested in this validation campaign: a wire mesh (WM) and a perforated plate (PP) (Figure 13b); both were made of stainless steel. Additionally, the hole pattern of the PP was oriented in two directions with respect to the back wall creating two variations of the PP: staggered (PPS) and parallel (PPP) (c.f. Figure 13b). Each PP variation was created merely by changing the orientation of the plate when cutting and installing it on the board.

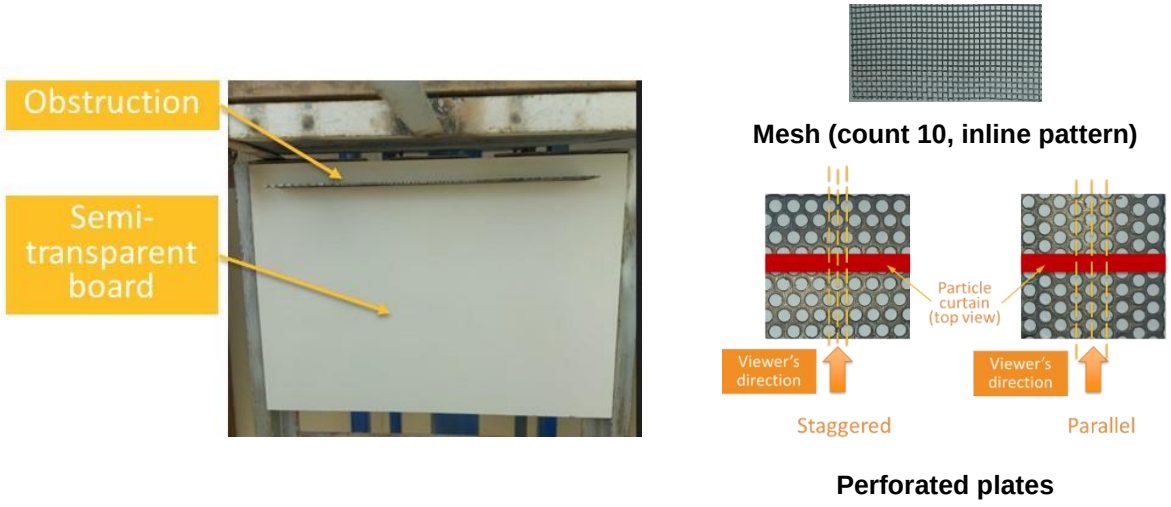

Figure 13. (a) A photo of the PHR test section and (b) the different obstructions used in the test campaign

To vary the particle mass flow rate, the feeder above the PHR test section was equipped with a compartment to house an interchangeable plate. The plate had a rectangular slot with the same length as that of the PHR. Figure 14 shows a schematic of the slotted plate that was inserted in the feeder with a 4.5 mm slot size. It was attached to a handgrip for easier insertion and removal of the plate. By changing the slot size of the plate, the particle mass flow rate could be varied for a given experiment.

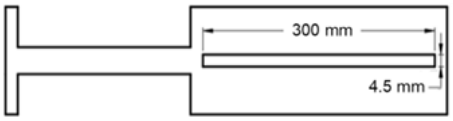

Figure 14. An example of the slotted plate (4.5 mm slot size); different slot sizes will give different particle mass flow rates

4.2. Velocity Measurements

As described above, the particle velocity below an obstruction was identified as an important variable affecting the performance a particle-based receiver. Therefore, it was a critical QoI to be measured in the validation campaign. For the velocity measurements, a Chronos 1.4 high-speed camera was utilized. It was capable of recording at a maximum rate of 1069 frame per second (FPS) at a resolution of 1280 x 1024. Two DC lamps were placed at the front and back of the PHR to give better quality of recorded videos (Figure 12). While recording the particle flow, a measuring scale was placed on the particle curtain front plane for a short period of time (Figure 15). This is done to be able to convert distance in the recorded videos/images from pixel to a length unit. Several images were extracted from the video and converted to an 8-bit grayscale image type to be ready for PIV analysis, which was carried out using PIVlab, a particle image velocimetry (PIV) tool in MATLAB.

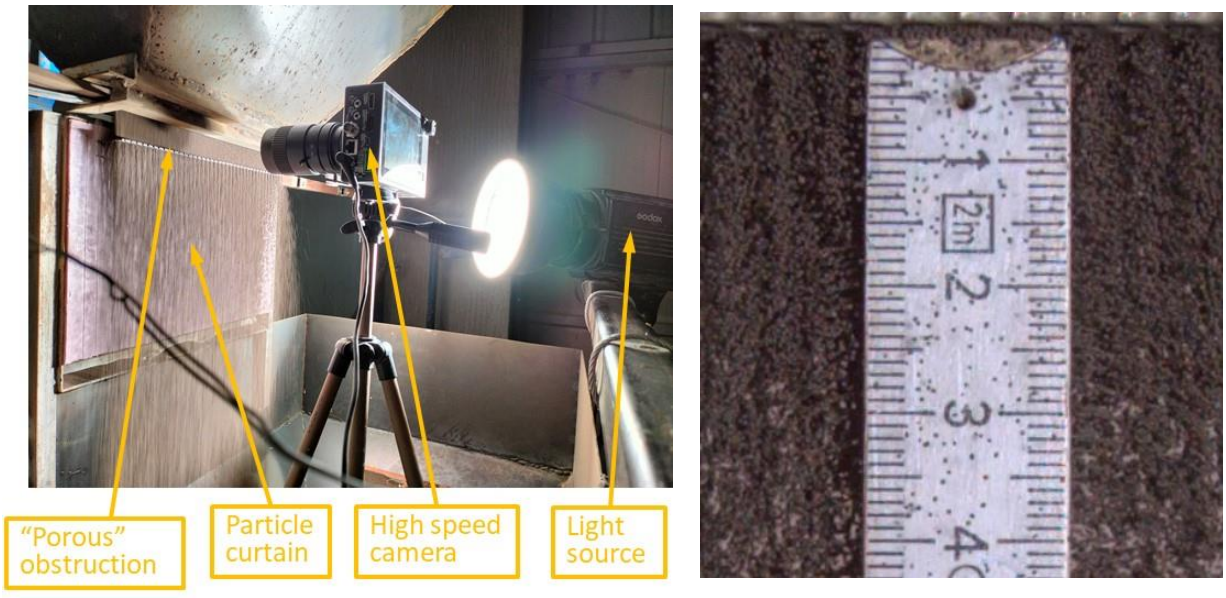

Figure 15. One of the particle velocity measurement tests (left) and measuring scale at the front plane of the particle curtain (right).

4.3. Particle Opacity Measurements

Additionally, the particle curtain opacity was measured in the experiments using a geometrical-based curtain opacity measurement ("line of sight"). To perform this measurement, changes to the test setup were necessary to get reliable and repeatable results. Initially, tests were done using boards made of opaque materials (calcium silicate, Styrofoam, and wood) as the base of the PHR with a forward-facing DC lamp (directionally similar to the high-speed camera; c.f. Figure 15). While this setup provided suitable conditions for velocity measurements, it did not yield quality curtain opacity measurements. A significant reason for this was that the illumination provided by the DC lamp in front of the PHR created particle shadows on the back wall in gaps that would otherwise be identified as regions where particles did not exist. Therefore, this resulted in misleading dark regions in the recorded videos/images that were difficult to distinguish with the back wall material.

To overcome this issue, a transparent acrylic board was used as the PHR back wall in conjunction with a DC lamp that was directed perpendicularly to the particle curtain from behind; the camera was still located in the same position. However, this still did not work well since the light from the back wall was too bright overwhelming the camera as shown Figure 16.

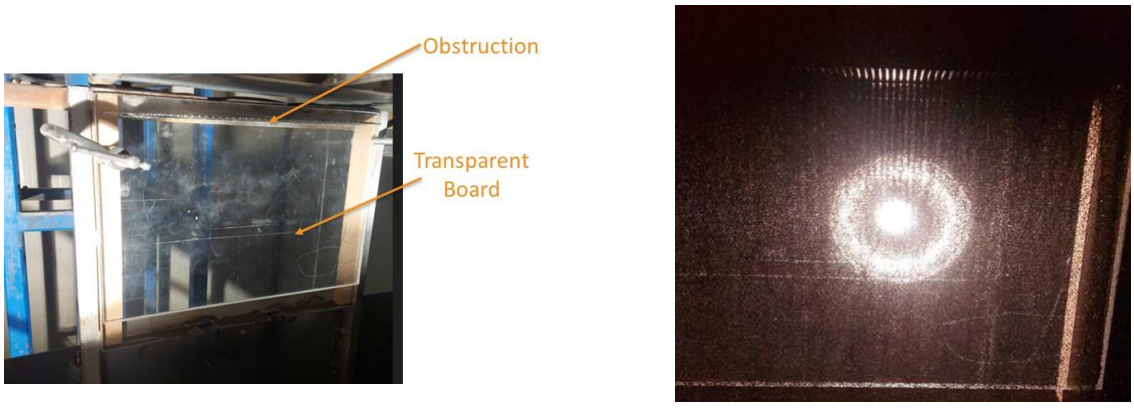

Figure 16. PHR with acrylic board base (left) and light from the back (right).

To finally resolve this issue, the acrylic board was lightly painted white (c.f. Figure 17) such that it was now translucent with good contrast with the natural color of the particles used in this experiment (black). By doing so, light was diffusely transmitted through the board, resulting in sufficient illumination of the back wall. During the particle-curtain opacity tests, only the lamp behind the PHR back wall was turned on (the front lamp, used for particle velocity illumination, was turned off).

Figure 17. The DC lamp behind the PHR (left) and the semi-transparent PHR board seen from the front (right); only the back-side lamp was on during the opacity measurements.

4.4. Experimental Methods

4.4.1. Test Procedures

The following test procedure was used in the experiments:

1. Place the appropriate obstruction and slotted plate for the experimental conditions to be obtained
2. Prepare the camera and lamps in their respective positions
3. Set the appropriate camera settings:
    a. low exposure time (high shutter speed) so that the particles' image is "frozen" in space; hence, sharp particle boundary
    b. analog gain (ISO) of the camera was set to ISO 320 to decreases digital noise; thereby, grainy images were avoided
4. Start the particle flow loop and allow the experiment to reach steady-state
5. Upon reaching steady particle flow, the recording was triggered for:
    a. the velocity measurements (both lamps switched on)
    b. the curtain opacity measurements (only the rear lamp switched on)

4.4.2. Geometric Test Parameters

The following geometric parameters were used for the experimental campaign, as shown in Figure 18. The distance from the tip (exit outer surface) of the particle feeder to the top surface of the obstruction (A) was either 30 or 60 mm. This was referred to as the falling distance/height and influenced the particle velocity impacting the obstruction. The depth of obstruction defined as the distance from the PHR back wall to the tip of the obstruction (B) was fixed at 30 mm in these experiments. The distance from the PHR back wall to the curtain centerline (C) was also fixed at 15 mm in this campaign.

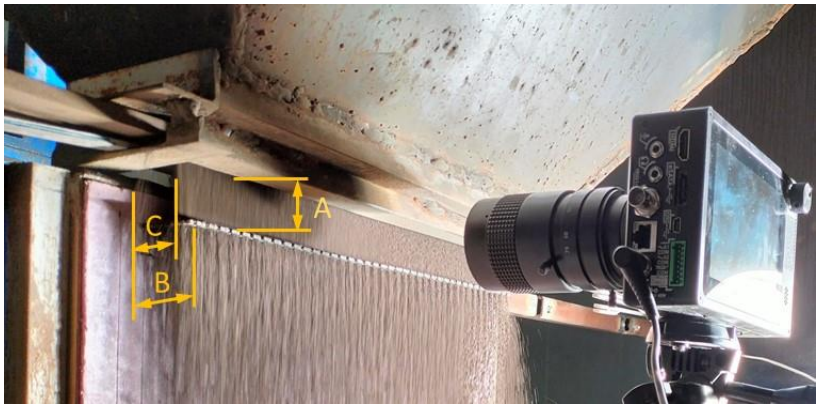

Figure 18. Geometric parameters used for the tests.

4.4.3. Curtain Opacity Thresholding

Curtain opacity measurements in this experimental campaign were evaluated using the image processing software, ImageJ. An image from the high-speed videos was uploaded to the software, and it was then converted to an 8-bit image. As described above, the definition used for curtain opacity here was the fraction of PHR back wall area that was covered by the particles in steady-state; To achieve this, thresholding was needed to divide the pixels into two regions: black and white, where dark pixels represented the backwall covered with particles and the white pixels represented the back wall uncovered by particles. Since there were pixels that were ambiguous for this classification (caused by pixels being partially covered by particles or imperfect lighting), a standardized thresholding method was required to handle these unclear values.

Two ways of thresholding were applied and compared: (1) the default method available in ImageJ and (2) a self-calculated value based on analysis of the pixel-values histogram. The former approach, as stated in the ImageJ manual, was using a variation of the IsoData algorithm. The latter approach, started by using the pixel values histogram. Then, threshold values were calculated by linear interpolation between two predefined cutoff values (above or below these cutoffs would represent pixel values for fully uncovered or covered pixels, respectively). These cut-off values were subjectively determined by identifying regions of sharp gradients in the histograms on log-scale. However, this method was ultimately found to create poor precision in the computed opacity values between equivalent experiments (likely due to the subjectivity of the selected cut-off values). Therefore, the default ImageJ thresholding method was used throughout the experimental campaign which was found to provide more consistency in the opacity measurements.

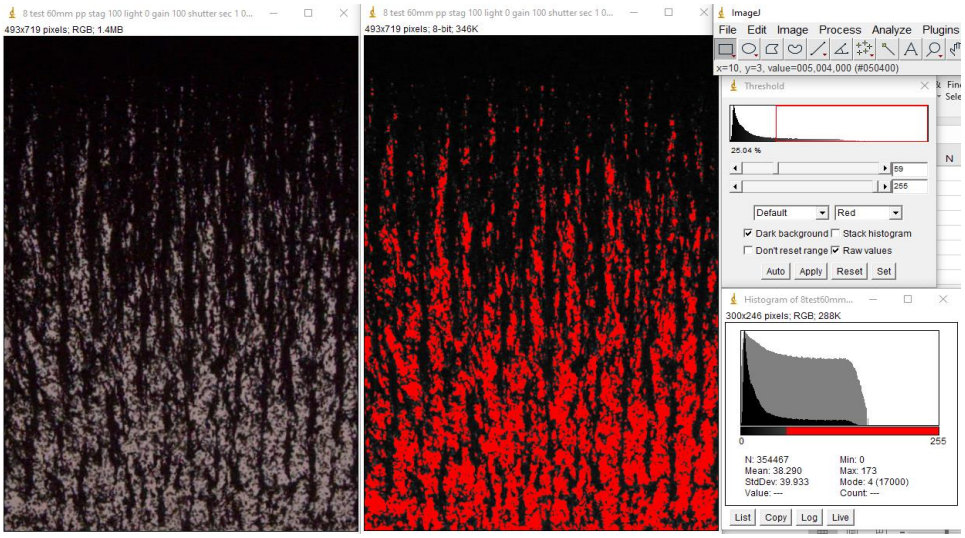

(a)

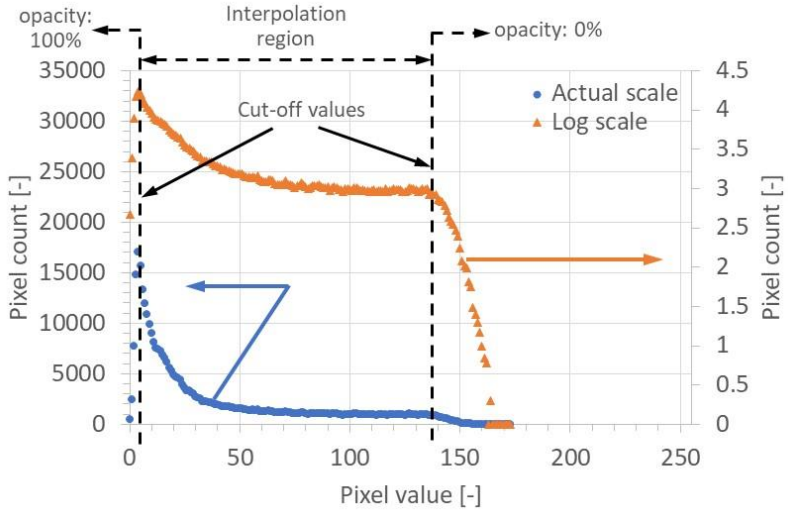

(b)

Figure 19. A sample post-processed image using the default thresholding method within ImageJ GUI (a) and a histogram of the 8-bit pixel values of the image showing the interpolation approach (b)

4.4.4. Curtain Opacity Calibration and Uncertainty

As explained above, the PHR back wall was made of a transparent board that was painted white to diffuse the rear illumination resulting better quality videos/images for curtain opacity measurements. Midway through the experimental campaign, a scratch was noticed on the painted board, and it was decided to create a new board. However, the new board received additional coatings of paint (compared to the first board) which resulted in darker images (Figure 20). As a result, it was suspected that the thresholding approach described above might yield different results depending on the intensity of the illumination. An effort was then undertaken to ensure that the curtain opacity measurements were not dependent on the lighting. Additionally, the uncertainty in the curtain opacity measurements was calculated.

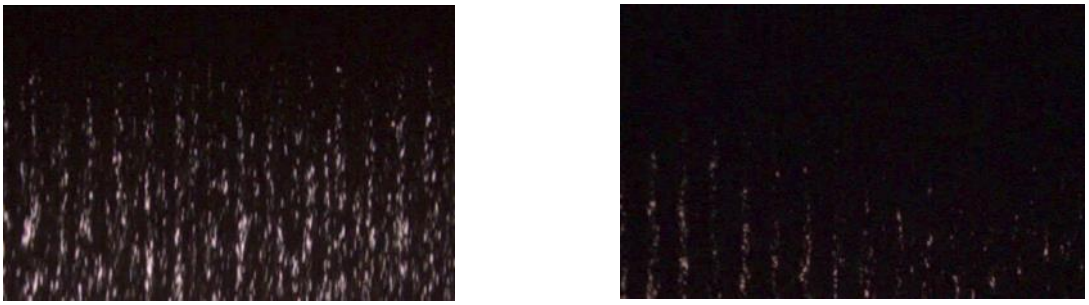

Figure 20. Images resulted from the old board (left) and the new (right).

To ensure the consistency and accuracy of the software in analyzing images obtained from different level of board translucency and back light intensity, a test setup was constructed evaluating the consistency of the measurements against a known value. For the known value, two types of obstructions with known dimensions were used as a truth: (1) a perforated plate with circular hole of 2.84 mm diameter, 4.29 mm pitch, and 60° between adjacent holes; and (2) a wire mesh of mesh-count 10 with 0.55 mm wire diameter (mesh-count 10 means ten openings per inch in both x and y directions). The obstructions were attached to the boards along with an adjustable-intensity light-source positioned behind it as shown in Figure 21. Three translucent boards were prepared by applying different number of paint layers: (1) one layer, (2) two layers, and (3) three layers of paint. The light was directed perpendicular to the board and set to emit 20%, 60%, and 100% of its maximum intensity.

A high-speed camera was used to capture videos of the test sections with various combination of board and light intensity. Images were extracted from the videos and, using the image processing software (ImageJ), the opacity was determined. Note that, as mentioned in the above, the definition of opacity in this work was the fraction of pixels deemed to be obstructed. The calculated opacities from ImageJ were compared to a "true" opacity obtained from the knowledge of geometry of the obstructions (mesh and perforated plate). Geometric tolerances of the obstructions were assumed to be negligible. Consequently, this process can be regarded as calibration, which provides a measure of the bias uncertainty.

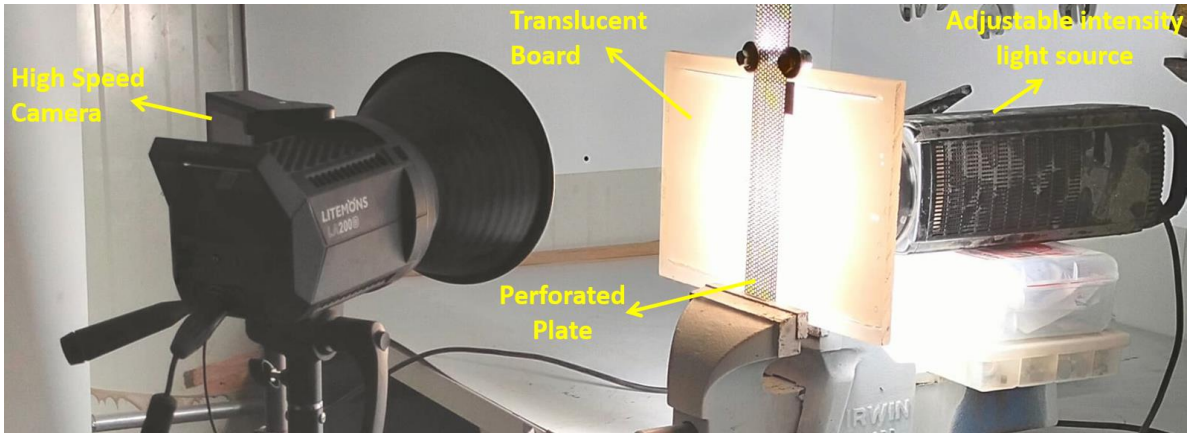

Figure 21. Opacity calibration setup, specifically using perforated plate; the same setup was used when using the mesh as the obstruction.

Results show that the translucency of the board and the light intensity did not affect the opacity calculated by ImageJ using the default thresholding method as shown in Table 3. This table presents the test results using both mesh and perforated plate (PP) where their opacities were calculated to be

38.62% and 60.26%, respectively (geometrically). The difference between measured average and true value was taken as the bias uncertainty. As shown in the table, the largest difference was found using the PP as the obstruction, i.e., 6.7 %-points; therefore, it was taken as the bias uncertainty for all measurements used in this study.

Table 3. Opacity values obtained from the recorded images with various combination of translucent boards and light intensities using auto threshold method.

	Mesh (True opacity: 38.62%)			PP (True opacity: 60.26%)		
	20% light	**60% light**	**100% light**	**20% light**	**60% light**	**100% light**
PL 1	40.47	40.39	40.50	53.18	53.48	53.40
PLs 2	40.23	40.21	40.45	53.35	53.16	53.24
PLs 3	40.66	40.72	40.80	54.79	54.05	53.81

Figure 22 shows an example of photograph image of the mesh before and after processing using ImageJ during the calibration test. This image was taken at 60% backlight intensity with a board having three layers of paint.

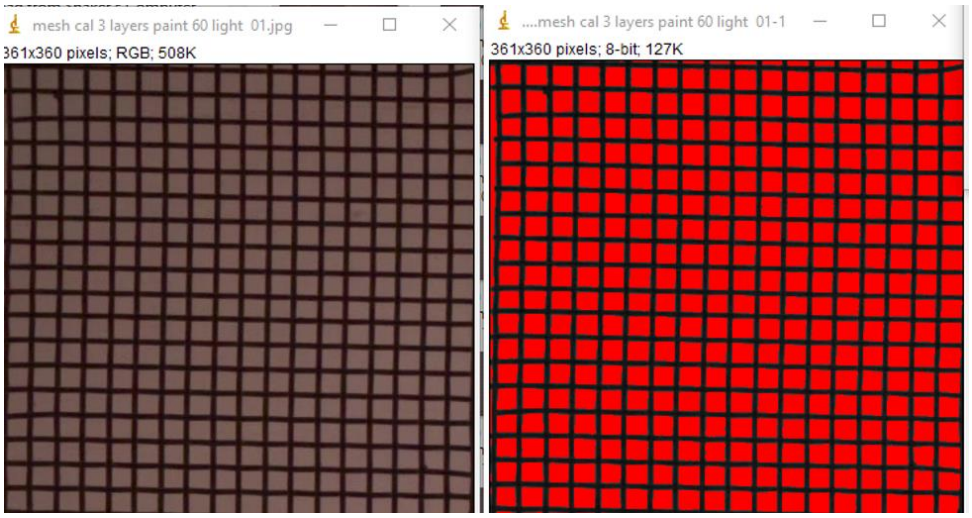

Figure 22. An image taken at 60% light intensity with a board having three layers of paint: before (left) and after ImageJ processing where the red pixels indicate unobstructed pixels (right)

Opacity measurements of a particle curtain using the same operating conditions with varying light intensity were also conducted to further verify the consistency of the measurements as seen in Table 3. To reduce the number of tests, only one board was tested with three different light intensities since it was found from the previous tests (Table 3 above) that the effect of the number of paint layers on the opacity calculation is the same as that of changing the light intensity, and the results are summarized in Table 4. The board with three layers of paint was used; the tests utilized perforated plate as the obstruction with particle mass flow rate of 1.91 kg/s/m. Results confirmed the consistency of the measurements using particles.

Table 4. Effect of the light intensity on the particle curtain opacity

light intensity	**20%**	**60%**	**100%**
PLs 3	86.50%	85.61%	85.07%

Finally, the random/precision uncertainty of the curtain opacity estimated from seven different images taken at different time frames under the same conditions. This test used 100% light intensity, a particle mass flow rate of 1.91 kg/s/m, and a PP obstruction with staggered arrangement. Measurements were taken for the first 5 cm below the PP. The results are presented in Table 5, and they show that all the images provided similar opacity values with a standard deviation of ±0.3%.

Table 5: Opacity measurements result for seven different images taken at various times

Image number	1	2	3	4	5	6	7	Avg	STDEV	U_A_vp
Opacity [%]	84.0	84.1	84.6	84.4	84.5	84.2	83.7	84.2	0.3	0.3

Based on the above tests, the uncertainty of the experiment was estimated by computing the root sum square (RSS) of the bias and precision uncertainties, which were 6.7 %-points and 0.3 %-points, respectively. The total uncertainty in the curtain opacity measurement was therefore estimated to be 6.7 %-points.

4.4.5. Particle Volume Fraction

It was important to also estimate the volume fraction of the particle curtain hitting the obstruction to quantify the range of experimental conditions for which the experimental setup applies. Using the images of the particle curtain above the obstruction, the particle volume fraction was computed for different mass flow rates and fall heights. As shown in Figure 23 and Figure 24, the particle volume fraction was found to range from a minimum of 10% to a maximum of 17% for the range of experimental conditions. Increasing to even higher volume fractions just before impact with the obstruction was deemed to be impractical for this experimental setup.

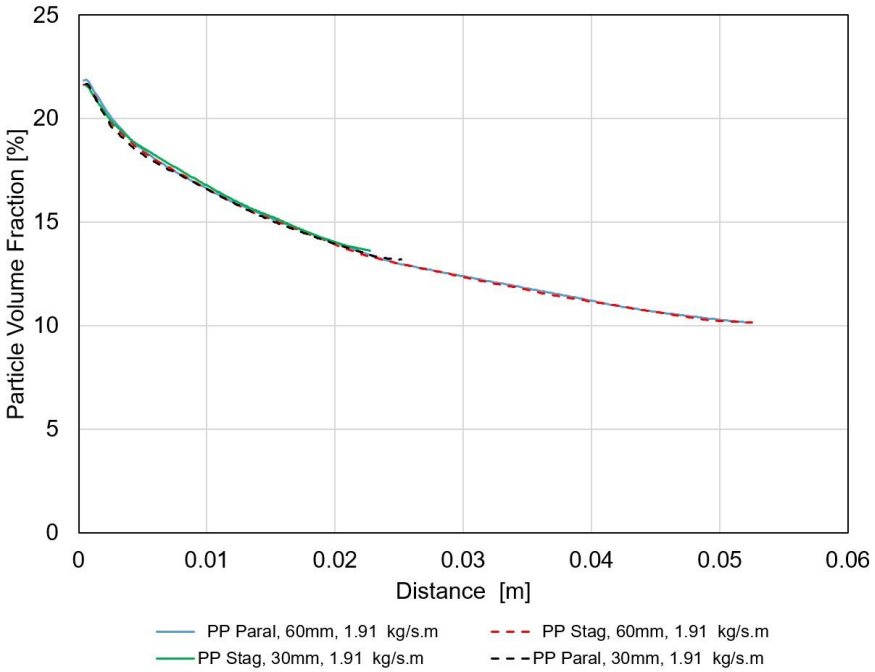

Figure 23. Particle volume fraction along the vertical distance for different fall height and type of obstruction, but constant mass flow rate.

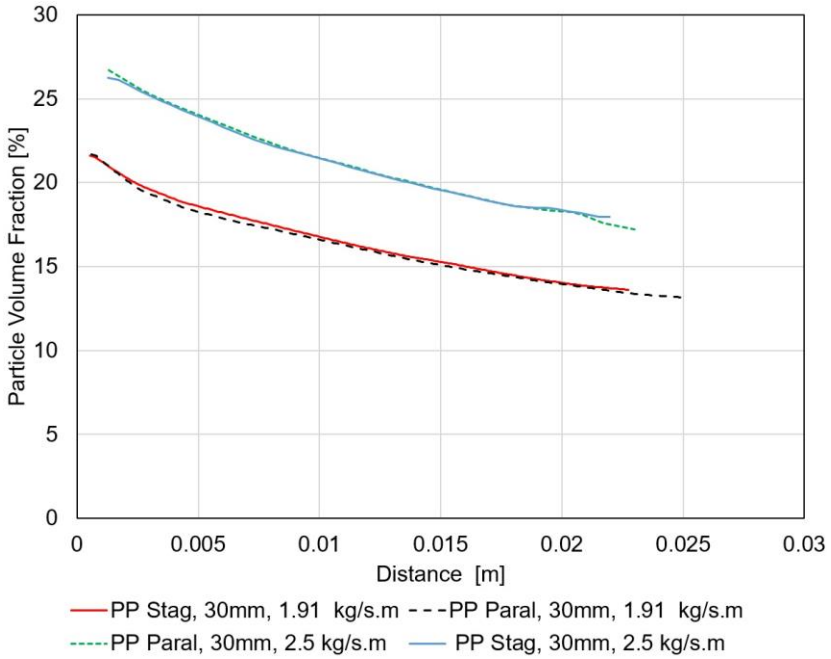

Figure 24. Particle volume fraction along the vertical distance for different mass flow rate and type of obstruction, but constant fall height.

4.5. Results and Discussion

4.5.1. Particle Flow Behavior

Figure 25a shows an image of the particle flow within the validation experiment. The image showcases a beneficial impact of the obstructions on the falling particle curtain. The utilization of straight-shaped porous obstructions in the design allows for a thicker and wider curtain. This advantageous design characteristic leads to the formation of a particle bed at the top of the porous obstruction (Figure 25b and c), facilitating the absorption of particle kinetic energy; thus, arresting particle velocity and increasing the particle curtain opacity.

The perforated plates (PP) tested can be oriented in two arrangements on the PHR: parallel (PPP; or paral.) and staggered (PPS; or stag.), depending on how they are cut and installed. Figure 25b and c provide a side-by-side comparison of the particle packed-bed formed on the perforated plate for both arrangements. These images were captured at a particle flow rate of 1.91 kg/s/m and a fall height of 30 mm. The average opening (hole) diameter of the perforated plate was 2.84 mm with 4.29 mm pitch and 60° between adjacent holes; this size of obstructions was carefully chosen to distribute the particles across the plate's area, thereby increasing curtain thickness.

The phenomenon of particle crowding causes particle accumulation on the PP which results in the creation of a relatively thin particle layer/pile (referred to here as the particle packed bed). The images revealed (c.f. Figure 25) that the PPP obstruction yielded a thinner and more dispersed particle packed bed, while the PPS obstruction created a thicker and less dispersed one. This was determined to be a function of the cross-sectional area of the openings created by the obstruction available to the particle curtain impact location.

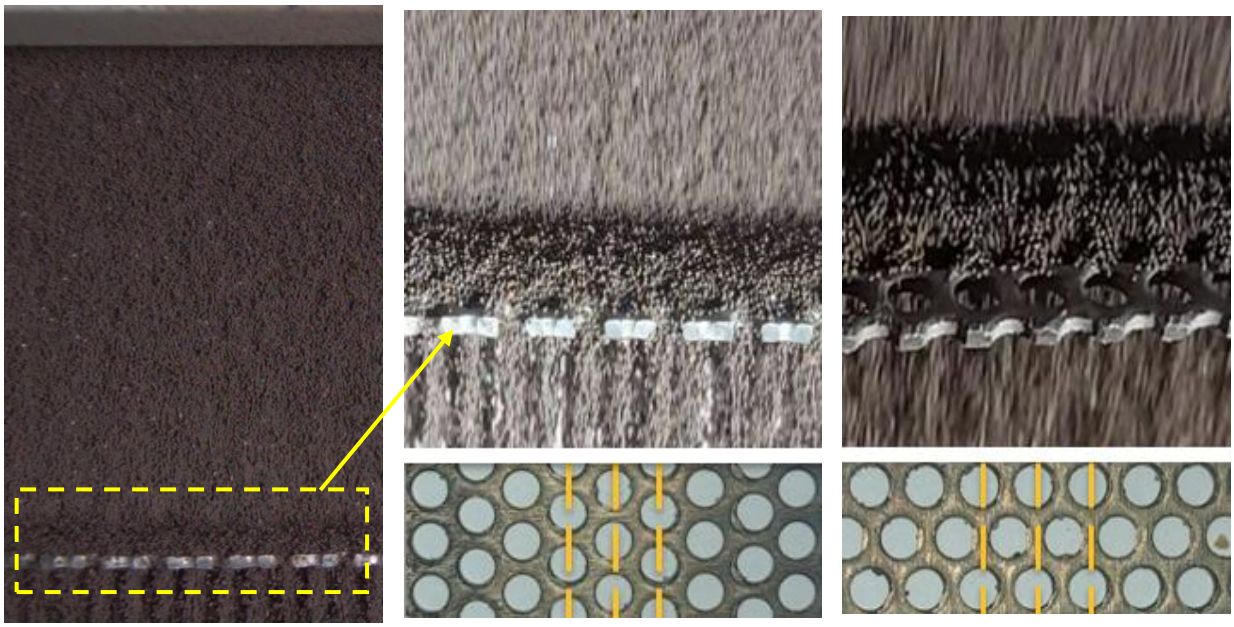

Figure 25. (a) Particle flow pattern above the perforated plate at a mass flow rate of 1.91 kg/s/m; (b) particle bed formation in the case of parallel arrangements; (c) particle bed formation in the case of staggered arrangements.

Practically, the formed packed bed can give several advantages to a PHR's performance: (1) adding additional protection to the back wall from being irradiated and eventually overheated, (2) absorbing kinetic energy of the falling particles (as opposed to the obstruction itself), (3) enhancing ray trapping by increasing the particle curtain thickness which results from the particle dispersion on the perforated plate, and (4) reducing the opportunity of obstruction overheating since most of the obstruction body will be covered and "cooled" by the particle curtain.

4.5.2. Particle Velocity

4.5.2.1. Above the Obstruction

The initial falling particle velocity before the obstruction was measured for two particle flow rates of 1.91 kg/s/m and 2.5 kg/s/m and two fall heights of 30 mm and 60 mm (the falling height). Figure 26 plots the velocity profile of particles above obstructions, comparing results for mesh, PPP, and PPS for a 30 mm falling height. As expected, the particle velocities across all configurations showed similar trends from the release point (particle feeder outlet) up to a distance of 0.022 m. Beyond this point, particles in the PPS, followed by those in the PPP, began to decelerate, which was attributed to the particle bed formation, as shown in Figure 25b and c. The maximum velocity recorded for the PPP was 0.87 m/s at 0.025 m, compared to 0.84 m/s at 0.023 m for the PPS. The mesh configuration exhibited the highest maximum velocity of 0.89 m/s at 0.026 m. This increased velocity in the mesh case is probably due to the obstruction thickness 1 mm less than that of the PP, effectively increasing the fall height. Similar to the PPP case, the particles on the mesh formed a flatter particle bed, which contributed to additional falling distance (a distance through which the particles travel), thereby increasing the maximum velocity. It is important to emphasize that the region where particle velocity starts to decrease does not represent the true particle bed height but the effect of particle collisions and their upward rebound on the falling particles.

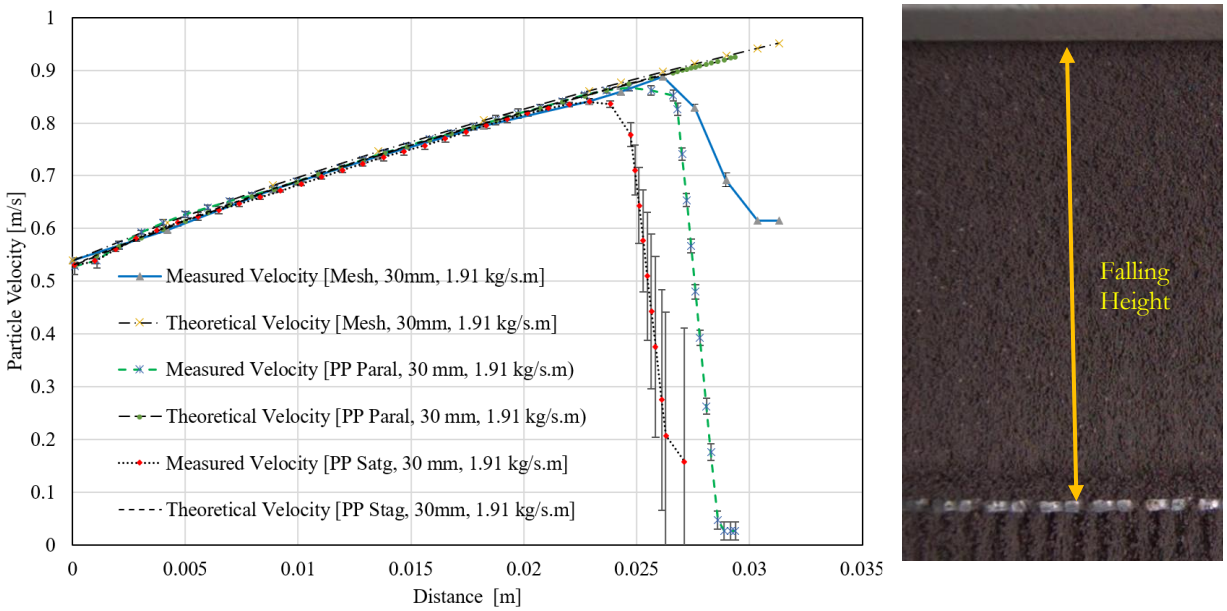

Figure 26. Particle velocity profile above the obstruction of various types (mesh, PPP, and PPS) for falling height, flow rate, and PHR tilt angle of 30 mm, 1.91 kg/s/m, and 0°, respectively.

A similar trend in the particle velocity profile was observed above the obstruction at a flow rate of 2.5 kg/s/m with a 30 mm falling height as shown in Figure 27. The measured particle velocities across all configurations remained consistent from the release point (particle feeder outlet) up to a falling distance of 0.021 m. Beyond this point, particles in the PPS configuration began to decelerate. The results indicated a higher maximum velocity in the PPP and mesh configurations also due to the formation of a smaller particle packed bed. The maximum velocity recorded was 0.86 m/s for both the PPP and mesh at 0.022 m, compared to 0.83 m/s for the PPS at 0.021m. It should be noted that increasing the mass flow rate to 2.5 kg/s/m led to particle flooding (particle overflowing) in the three cases, as the obstructions' limited opening area restricted particle passage as shown in Figure 27 right.

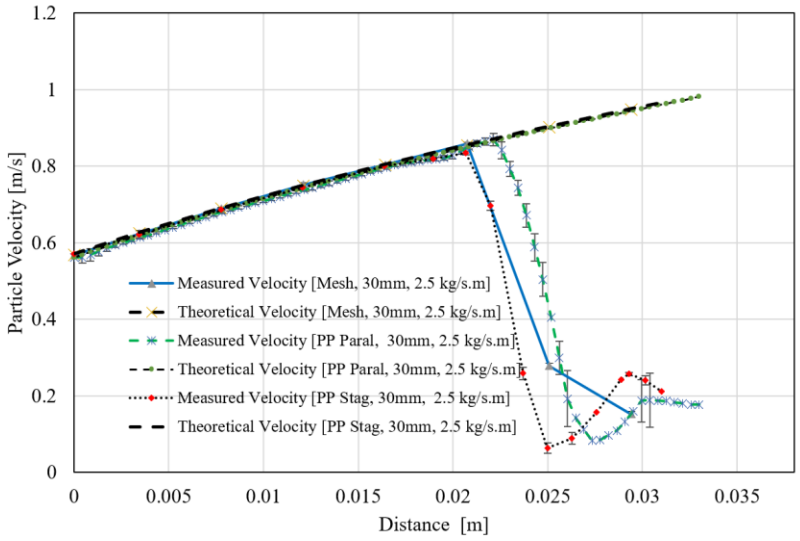

Figure 27. Particle velocity profile above the obstruction of various types (mesh, PPP, and PPS) for falling height, flow rate, and PHR tilt angle of 30 mm, 2.5 kg/s/m, and 0°, respectively.

Figure 28 and Figure 29 depict the velocity profile for the particles above the three porous obstructions for the 60 mm falling height at 1.91 kg/s/m and 2.5 kg/s/m, respectively. Different from the 30 mm falling height case, the results demonstrated nearly identical velocity profiles across all obstruction types from the release point up to the velocity drop region. This is likely due to higher kinetic energy of the falling particles prior to the impact with the obstruction, causing the particles to spread to a certain extent equally regardless the obstruction types. At a mass flow rate of 1.91 kg/s/m, the peak velocities recorded were around 1.13 m/s for all obstructions, which happened at around 0.053 m below the release point. When the mass flow rate increased to 2.5 kg/s/m, the maximum velocities reached around 1.17 m/s for all obstructions and occurred at approximately the same distance below the release point as that of the 1.91 kg/s/m.

Similar to the previous results (the case of 30 mm falling height), Figure 28 and Figure 29 underscore the influence of the particle bed height formed above the obstructions, which is reflected in the sharp drop in velocity beyond 0.05 m, albeit gradual at the beginning of the drop. The increased uncertainty near the packed bed region was primarily attributed to the dynamic behavior of the particles, as they tended to exhibit random bouncing in this area. Notably, the error bars in both figures grew significantly as the distance approached 0.06 m, signifying greater experimental variability during the deceleration phase. This variability was likely caused by complex particle interactions, turbulence, or other dynamics.

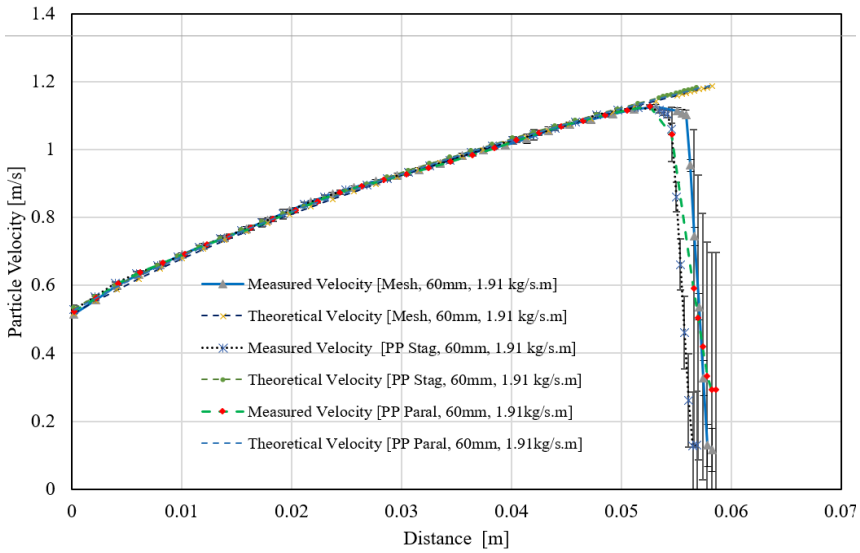

Figure 28. Particle velocity profile above the obstruction of various types (mesh, PPP, and PPS) for falling height, flow rate, and PHR tilt angle of 60 mm, 1.91 kg/s/m, and 0°, respectively

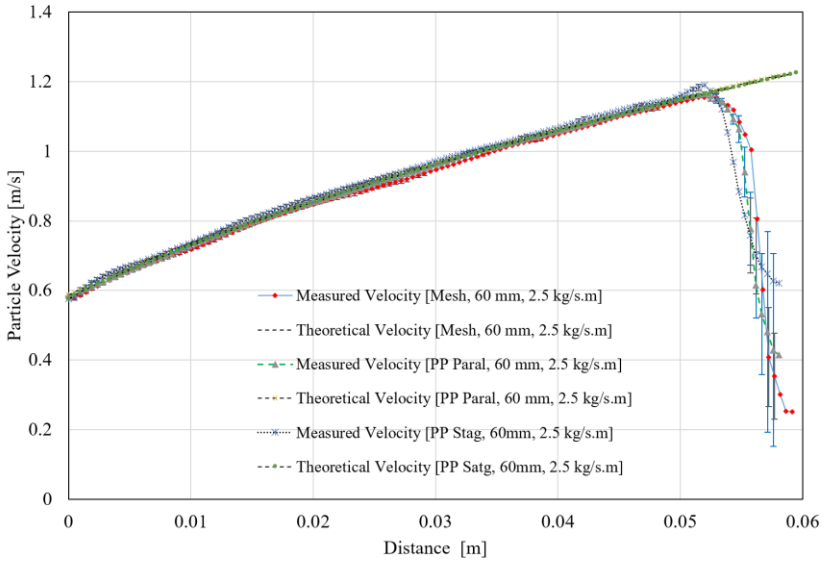

Figure 29. Particle velocity profile above the obstruction of various types (mesh, PPP, and PPS) for falling height, flow rate, and PHR tilt angle of 60 mm, 2.5 kg/s/m, and 0°, respectively.

The effect of the PHR tilt angle on particle velocity was also investigated experimentally. Specifically, particle velocity at a 7° PHR tilt angle was measured for the three types of porous obstructions: mesh, PPP, and PPS. These measurements were conducted at two distinct mass flow rates, 1.82 kg/s/m and 2.5 kg/s/m, with a constant falling distance of 30 mm. Note that the measurements were taken at a flow rate of 1.82 kg/s/m instead of 1.91 kg/s/m. The reduction in mass flow rate can be attributed to the unintentional distortion of the slot shape that occurred during re-installation into the hopper. After completing the measurements at a 0° angle, it was found that the slot plate had become stuck due to particles entering its rail, requiring significant force to slide it back into place, causing the distortion. Unlike the case observed at 1.91 kg/s/m, at this mass

flow rate, the particles did not reach the tip in any of the obstruction configurations, indicating a similar bed formation (Figure 30). This effect can be attributed to two factors: (1) the 7° tilt angle redirected particles striking the obstruction back toward the rear, increasing the height of the particle bed near the board/base and thereby reducing the particle dispersion area, and (2) the reduction in mass flow rate (from 1.91 to 1.82 kg/s/m) required fewer openings in the porous obstructions to effectively accommodate the flowing particles.

(a) (b) (c)

Figure 30. Particle packed bed on the three porous obstructions: (a) Mesh, (b) PPP, (c) PPS

The particle velocity profiles at 1.82 kg/s/m and 2.5 kg/s/m were presented in Figure 31 and Figure 32. The particle velocity profiles exhibited similar trends across all configurations, i.e., the particles accelerated and, at some point, decelerated steeply. It can be seen in Figure 31 that at a flow rate of 1.82 kg/s/m, the maximum velocities observed for all obstruction configurations (mesh, PPP, and PPS) ranged between 0.85-0.9 m/s; all occurred at a falling distance (particle travel distance from the particle feeder outlet) of approximately 0.023-0.024 m, implying that all have similar pack bed heights.

At a higher mass flow rate of 2.5 kg/s/m, the packed bed effect was observed earlier at 0.014 m for PPS and 0.016 m for PPP configurations. This can be attributed to the formation of a taller packed bed, resulting from the accumulation of particles on a smaller surface area, tend to accumulate at the base, due to the increased mass flow rate and tilting of the PHR. At this flow rate, the maximum velocities recorded were around 0.78 and 0.79 m/s for PPP and PPS, respectively. As for the mesh configuration, it reached a maximum velocity of 0.84 m/s at a fall distance of 0.020 m, which indicated that it has the shortest packed bed height, followed by PPP and PPS.

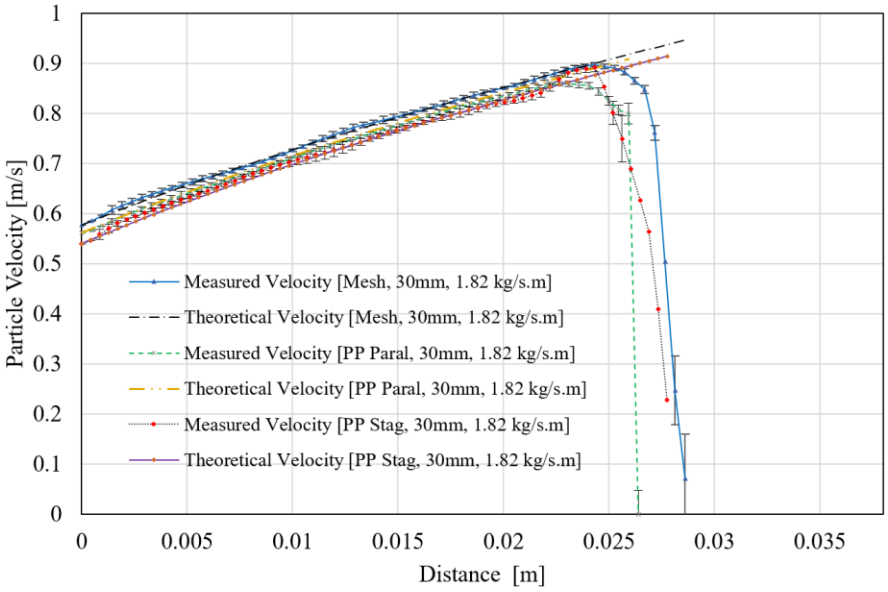

Figure 31. Particle velocity profile above the obstruction of various types (mesh, PPP, and PPS) for falling height, flow rate, and PHR tilt angle of 30 mm, 1.82 kg/s/m, and 7°, respectively

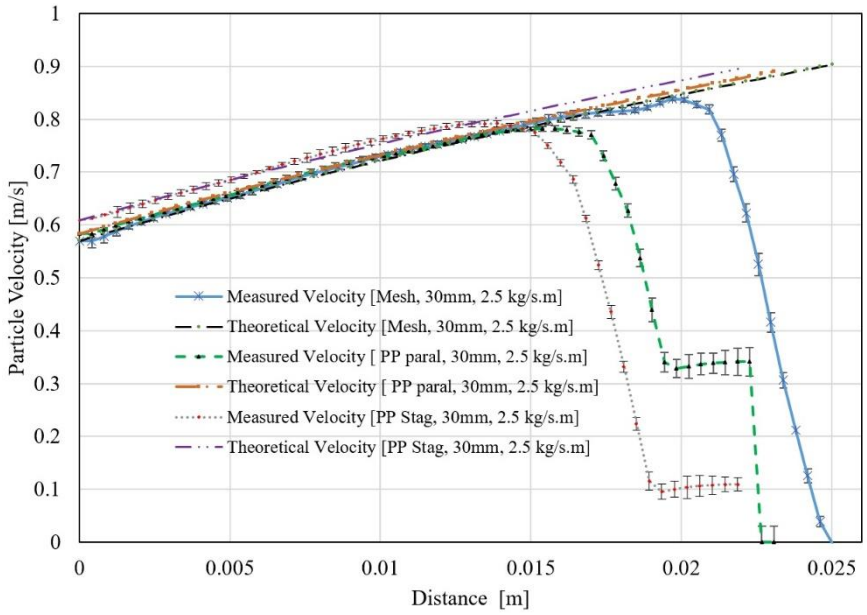

Figure 32. Particle velocity profile above the obstruction of various types (mesh, PPP, and PPS) for falling height, flow rate, and PHR tilt angle of 30 mm, 2.5 kg/s/m, and 7°, respectively

4.5.2.2. Below the Obstruction

Figure 33 presents the velocity profiles of particles *after (below)* the obstruction over a 30 mm falling height at a mass flow rate and PHR tilt angle of 1.91 kg/s/m and 0°. The profiles compared three configurations: Mesh, PPP and PPS. Both the measured and theoretical velocities were presented to have an insight into the behavior of particles in different configurations. The results showed that for all configurations, a similar trend of increasing velocity from the starting point up to about 0.08 m was exhibited. This consistent acceleration phase indicated that the particle velocity was nearly identical across all configurations. The overall trend for Mesh, PPP and PPS was very similar,

indicating that despite minor differences, the particle velocity profiles were not heavily influenced by the obstruction type under the tested conditions. For PPP and PPS, the close alignment suggested that different plate arrangement (parallel vs. staggered) did not significantly impact the velocity profile at mass flow rate of 1.91 kg/s/m. Moreover, Figure 33 also showed that the measured and theoretical velocities for all cases were closely aligned up to 0.03 m below the obstructions, and they started to differ from the theory afterwards, indicating a more significant air-particle interaction effect such as drag and air flow driven by the falling particles. Another important point was that all obstructions were able to decrease the particles velocity significantly from around 0.8-0.9 m/s before the obstructions to around 0.1-0.2 m/s after. It indicated that the obstructions performed well in increasing the residence time on the PHR; however, to further assess their performance, a PHR with multi-row obstructions must be tested, which is left as future work.

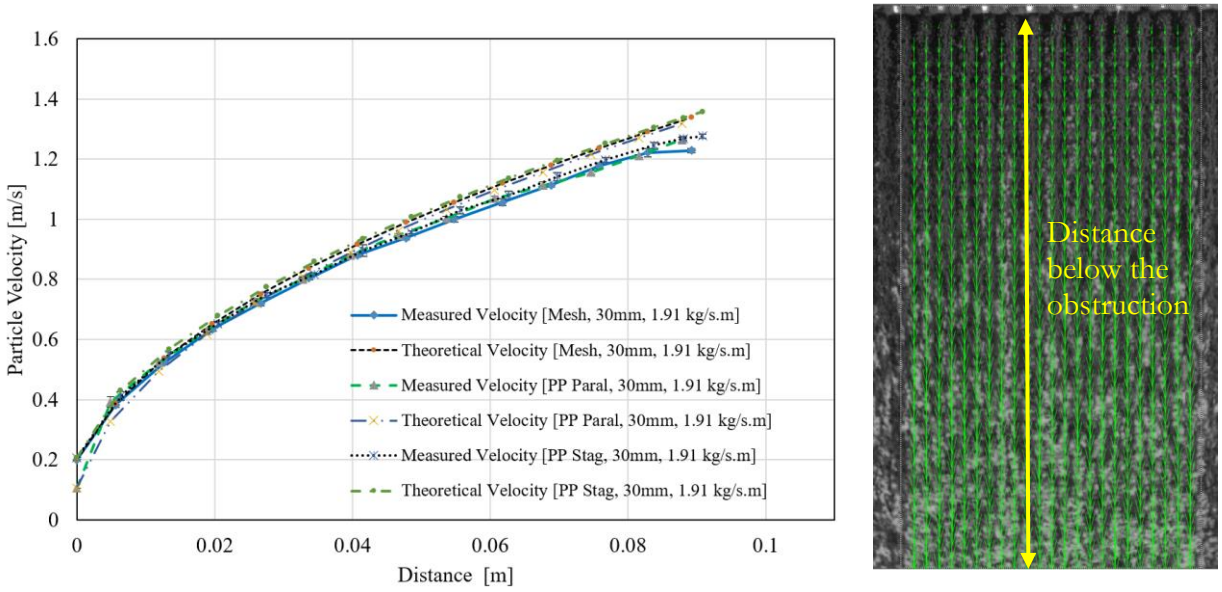

Figure 33. Particle velocity profile below the obstruction of various types (mesh, PPP, and PPS) for falling height (release point above the obstruction), flow rate, and PHR tilt angle of 30 mm, 1.91 kg/s/m, and 0°, respectively.

Figure 34 presents a comparative analysis of the particle velocity as a function of distance below the obstruction for different configurations of obstruction, where the falling height above the obstruction is fixed at 60 mm and the particle mass flow rate is set to 1.91 kg/s/m. The plot illustrates both measured and theoretical particle velocities for three configurations: mesh, PPP, and PPS. The theoretical curve was determined from the kinematic equation for falling objects assuming no drag.

The results showed that, similar to the case of 30 mm falling height, all configurations were able to impede the falling particles movement well, reducing its speed from approximately 1.1 m/s to around 0.23 m/s. The theoretical predictions for each configuration aligned closely with the measured data up to falling distance of about 0.03 m, showcasing that the kinematic models were able to capture the initial particle behavior. After that, all obstruction configurations exhibited a noticeable reduction in acceleration, less than that predicted by the theory. As mentioned before, this was, most likely, due to the effect of air that is getting more significant as the particles travel downstream, creating drag that decreased the particle acceleration.

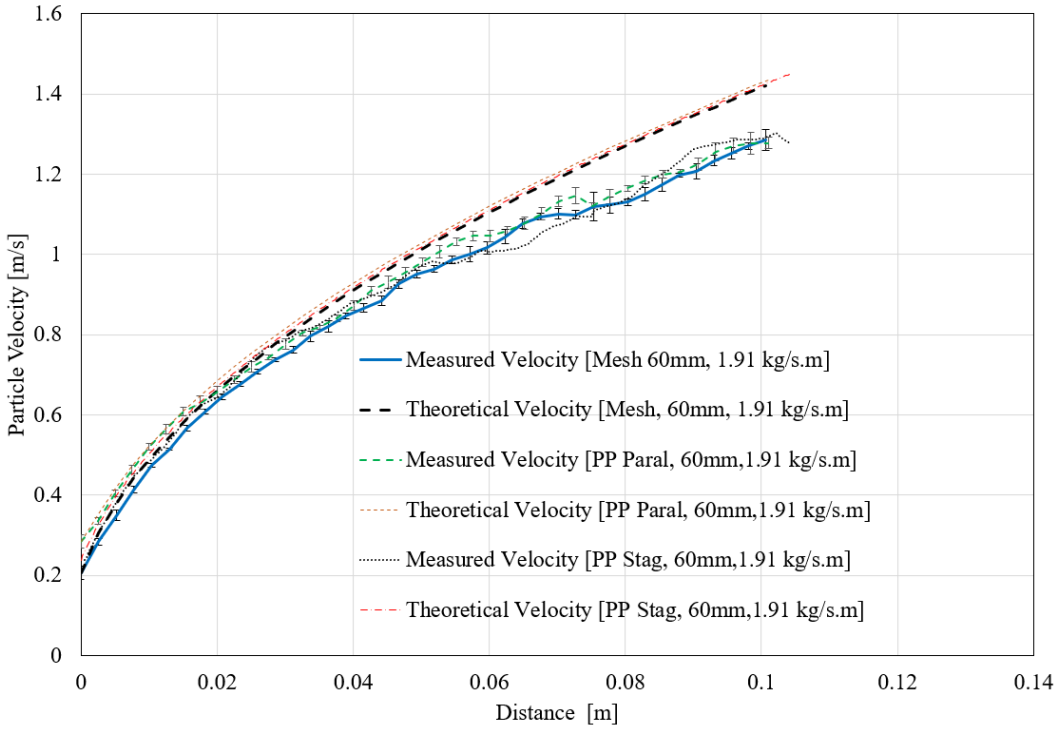

Figure 34. Particle velocity profile below the obstruction of various types (mesh, PPP, and PPS) for falling height (release point above the obstruction), flow rate, and PHR tilt angle of 60 mm, 1.91 kg/s/m, and 0°, respectively.

Figure 35 illustrates the velocity profiles of particles for a 30 mm falling height at a mass flow rate of 1.82 kg/s/m and PHR tilt angle of 7° for all configurations. From this figure, it was seen that the velocity profiles below the obstruction were similar for all obstruction types. They showed a good agreement with the theoretical velocity up to 0.03 m and then deviated afterwards, suggesting the theoretical models accurately capture the early stages of particle descent, but become less accurate as factors like drag, falling-particles-driven air flow, and turbulence came into play.

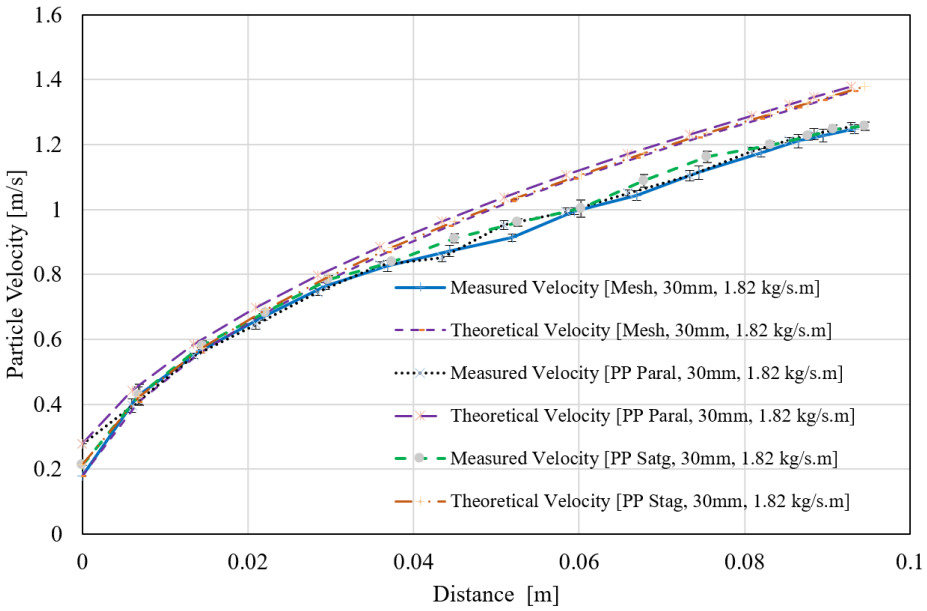

Figure 35. Particle velocity profile below the obstruction of various types (mesh, PPP, and PPS) for falling height (release point above the obstruction), flow rate, and PHR tilt angle of 30 mm, 1.82 kg/s/m, and 7°, respectively.

A summary of the experiment results is presented in Table 6 and Table 7 for 0° tilt angle before and after the obstruction, respectively. Table 8 and Table 9 provide results for 7° tilt angle before and after the obstruction, respectively.

Table 6. Summary of experimental particle velocity results above the obstruction at 0° tilt angle

#	Obstruction Geometry	Particle Mass Flow Rate [kg/s/m]	Fall Height	Particle Velocity (20 mm)	Particle Velocity (40 mm)	Max Particle Velocity
1	PPP	1.91	30	0.820±0.008	----	0.868±0.007
2			60	0.816±0.007	1.022±0.006	1.127±0.003
3		2.5	30	0.819±0.006	----	0.869±0.022
4			60	0.839± 0.002	1.040±0.004	1.164±0.013
5	PPS	1.91	30	0.815±0.005	----	0.836±0.006
6			60	0.822±0.010	1.025±0.010	1.124±0.005
7		2.5	30	0.816±0.004	----	0.835±0.011
8			60	0.851±0.005	1.053±0.004	1.189±0.017
9	Mesh	1.91	30	0.805±0.004	----	0.889±0.006

10			60	0.823±0.005	1.018±0.010	1.126±0.007
11		2.5	30	0.820±0.004	----	0.863±0.022
12			60	0.848±0.003	1.049±0.005	1.155±1.181

Table 7. Summary of experimental particle velocity results below the obstruction at 0° tilt angle

#	Obstruction Geometry	Particle Mass Flow Rate [kg/s/m]	Fall Height [mm]	Falling Distance Below the Obstruction			
				20 mm	40 mm	60 mm	80 mm
1	PPP	1.91	30	0.603±0.008	0.853±0.005	1.040±0.006	1.181±0.010
2			60	0.653±0.014	0.867±0.010	1.046±0.014	1.16±0.009
3		2.5	30	0.656±0.008	0.890±0.011	1.085±0.007	1.225±0.011
4			60	0.641±0.008	0.882±0.006	1.039±0.018	1.197±0.013
5	PPS	1.91	30	0.608±0.009	0.864±0.009	1.054±0.008	1.212±0.008
6			60	0.643±0.013	0.878±0.020	1.008±0.020	1.134±0.012
7		2.5	30	0.671±0.008	0.873±0.004	1.054±0.008	1.215±0.009
8			60	0.669±0.009	0.885±0.011	1.054±0.012	1.197±0.014
9	Mesh	1.91	30	0.608±0.009	0.852±0.005	1.023±0.006	1.193±0.012
10			60	0.630±0.007	0.853±0.008	1.017±0.015	1.128±0.010
11		2.5	30	0.686±0.010	0.903±0.022	1.083±0.016	1.247±0.011
12			60	0.632±0.003	0.861±0.006	1.017±0.011	1.186±0.007

Table 8. Summary of experimental particle velocity results above the obstruction at 7° PHR tilt and 30 mm fall height

#	Obstruction Geometry	Particle Mass Flow Rate	Particle Velocity (20 mm) (m/s)	Max Particle Velocity
1	PPP	1.82	0.815±0.004	0.860±0.007
2	PPP	2.5	0.499±0.018	0.783±0.008
3	PPS	1.82	0.810±0.006	0.892±0.022
4	PPS	2.5	0.273±0.015	0.792±0.005
5	Mesh	1.82	0.830±0.003	0.897±0.006

6	Mesh	2.5	0.828±0.004	0.839±0.004

Table 9. Summary of experimental particle velocity results below the obstruction at 7° tilt angle and 30 mm fall height

#	Obstruction Geometry	Particle Mass Flow Rate [kg/s/m]	Falling Distance Below the Obstruction			
			20 mm	40 mm	60 mm	80 mm
1	PPP	1.82	0.592±0.007	0.836±0.015	0.985±0.010	1.142±0.010
2	PPP	2.5	0.656±0.013	0.873±0.008	1.035±0.011	1.166±0.024
3	PPS	1.82	0.632±0.010	0.850±0.010	0.982±0.020	1.173±0.010
4	PPS	2.5	0.669±0.017	0.891±0.020	1.038±0.011	1.137±0.036
5	Mesh	1.82	0.624±0.012	0.841±0.014	0.990±0.014	1.151±0.011
6	Mesh	2.5	0.662±0.005	0.873±0.011	1.071±0.011	1.172±0.021

4.5.3. Curtain Opacity

Figure 36 represents a sample of particle curtain opacity measurements conducted at 20 mm intervals, covering a total distance of 80 mm below the obstruction, specifically for a mass flow rate of 1.91 kg/s/m. The measurements in Figure 36 utilized a PPP obstruction. Each section also provides a computed curtain opacity. The particle curtain opacity was depicted by the black regions, which represent the particle-dense areas, and the red regions indicated unobstructed pixels.

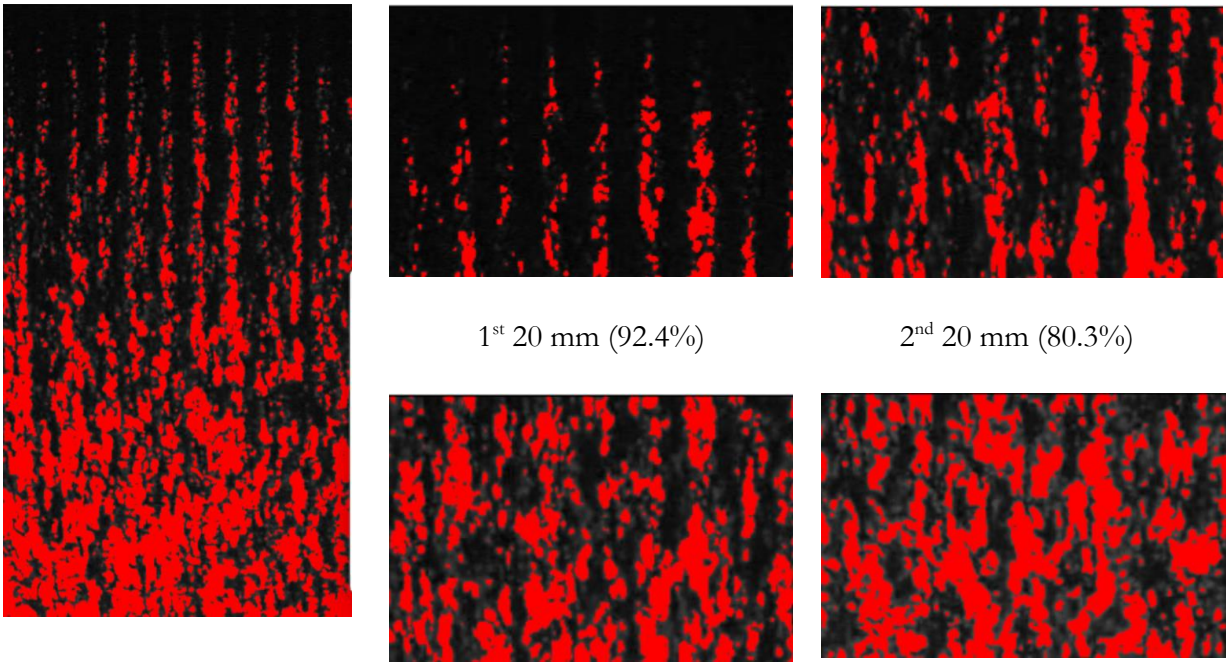

Figure 36. Processed photographic image for curtain opacity below the obstruction at every 20-mm interval for PPP arrangement at mass flow rate of 1.91 kg/s/m and 0° tilt angle.

The overall particle curtain opacity across the entire 80 mm window is 78.2%. This suggests that approximately 78% of the light is physically blocked by the particles. The image of the whole window showed an increasing curtain opacity as the particles fell. This was in line with expectations. As particles continued to fall, they continued to increase in velocity and particles dispersed from one another vertically thus decreasing the opacity. The opacity in the first 20 mm section had the highest opacity at 92.4%. This indicated that this portion of the particle curtain was very densely packed. The second 20 mm section exhibited a lower opacity of 80.3%. The opacity in the third 20 mm section dropped to 68.9%, reflecting a significant decrease in particle density compared to the first two sections. The lowest opacity, 58.3%, was observed in the fourth 20 mm section. An interesting observation was also seen in the images that showed very tightly packed columnar flow of the particle streams below the obstruction. As will be discussed in the model validation section below, this proved to be a significant factor affecting the ability to accurately predict the particle curtain opacity with the code's framework developed here.

Figure 37 presents the particle curtain opacity for different sets of parameters for the PPS obstruction. The parameters included two different falling heights of 30 mm and 60 mm above the obstruction and two mass flow rates, 1.91 and 2.5 kg/s/m, all at a 0° tilt angle. The particle curtain opacity was assessed for every 20 mm segment below the obstruction: 0–20 mm, 20–40 mm, 40–60 mm, and 60–80 mm. Generally, the results showed that, the particle curtain opacity decreased consistently with increasing fall distance (farther below the obstruction).

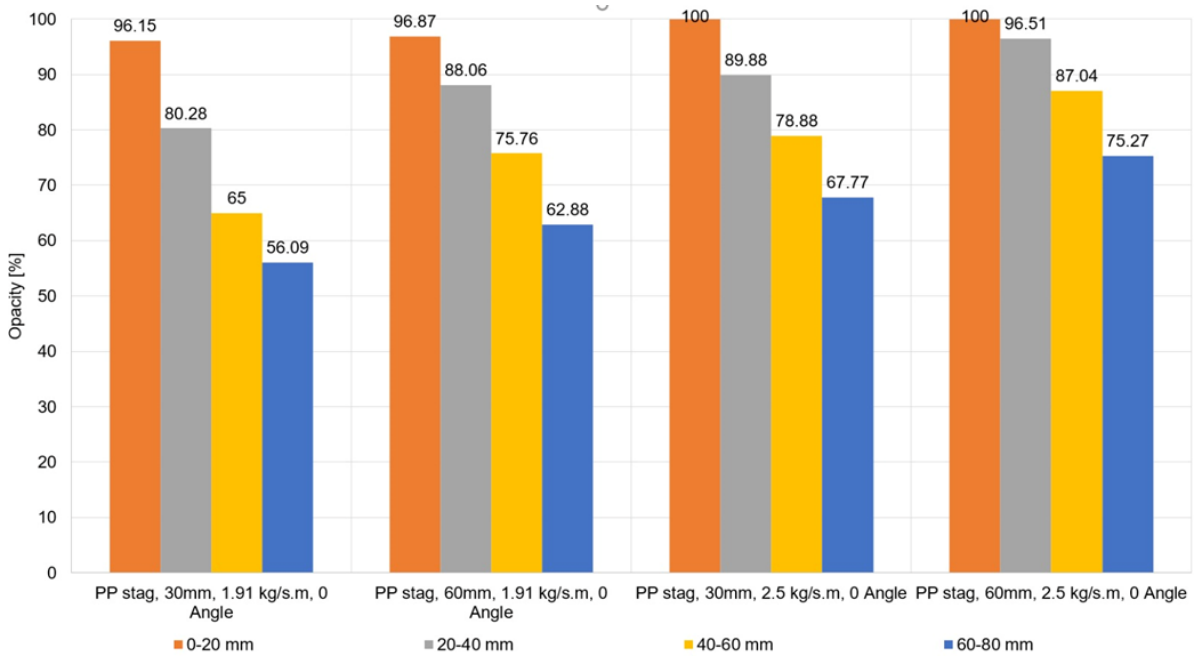

Figure 37. Effect of mass flow rate and falling height on the particle curtain opacity of perforated plate of Staggered arrangements.

Figure 37 also shows that the falling height significantly affected the opacity of the particle curtain. The 60 mm falling height configurations consistently show higher opacity across all 20 mm-segments compared to the 30 mm configurations. This indicated that not all particle velocity information was lost as the particles impacted the obstruction. Increased particle velocity on impact likely created more particle dispersion on the obstruction thereby increasing the curtain opacity.

The mass flow rate had a profound effect on the opacity of the particle curtain. As expected, 2.5 kg/s/m configurations exhibited consistently higher opacity across all falling distances compared to the 1.91 kg/s/m configurations. The higher mass flow rate resulted in a denser as well as thicker curtain, as more particles were packed into the same volume of space. The 2.5 kg/s/m configurations maintained near-total opacity in the 0–20 mm range (~100%), and the opacity declined more slowly compared to the lower flow rate. This indicated that higher mass flow rates helped maintain particle density for longer distances, resulting in a thicker curtain. Also, it should be noted that, at this flow rate, the particles spread to the front such that the particle curtain covered the leading edge of the obstruction, i.e., some particles overflowed the leading edge. Table 10 summarizes all of the opacity measurement results for 0° tilt angle and particle curtain below the obstruction.

Table 10. Summary of opacity [%] results below the obstruction at 0° tilt angle

#	Obstruction Geometry	Mass Flow Rate [kg/s/m]	Fall Height [mm]	0-20 mm	20-40 mm	40-60 mm	60-80 mm	Overall (80 mm)
1	PPP	1.91	30	92.38	80.29	68.91	58.29	71.24
2			60	96.22	85.78	72.48	62.72	78.03
3		2.5	30	94.16	82.19	76.74	67.77	79.34

4			60	96.19	89.61	84.28	76.9	87.33
5	PPS	1.91	30	96.15	80.28	65	56.09	69.95
6			60	96.87	88.06	75.76	62.88	80.09
7		2.5	30	100 (not detected)	89.88	78.88	67.77	82.63
8			60	100 (not detected)	96.51	87.04	75.27	89.31
9	Mesh	1.91	30	95.42	81.42	65.94	58.18	69.95
10			60	98.23	88.41	76.37	62.88	80.04
11		2.5	30	100 (not detected)	87.96	77.12	65.44	79.37
12			60	100 (not detected)	95.8	87.3	75.28	89.12

Not detected* indicates that the ImageJ thresholding provided an inaccurate value. In these cases, the actual opacity values were very high, but the software erroneously reported unreasonably low values.

Table 11 summarizes the particle curtain opacity for different configurations of the PPP, PPS, and mesh obstructions at two mass flow rates (1.82 kg/s/m and 2.5 kg/s/m) with a 7° tilt angle. The particle opacity was analyzed for different segments below the obstruction (0–20 mm, 20–40 mm, 40–60 mm, and 60–80 mm), and the overall opacity was provided for the full 80 mm window. It was found that the trend of the curtain opacity was the same as that for the 0° tilt angle, but with higher opacity values.

Table 11. Summary of opacity [%] results below the obstruction at 7° tilt angle and 30mm falling height

#	Obstruction Geometry	Mass Flow Rate [kg/s/m]	0-20 mm	20-40 mm	40-60 mm	60-80 mm	Overall 80mm
1	PPP	1.82	91.88	81.1	78.12	70.13	79.99
2		2.5	100 (not detected)	89.32	85	79.67	87.08
3	PPS	1.82	100 (not detected)	88.12	79.97	71.5	83.54
4		2.5	100 (not detected)	100 (not detected)	89.58	82.87	91.01
5	Mesh	1.82	100 (not detected)	90.59	80.39	72.29	84.32
6		2.5	100 (not detected)	100 (not detected)	89.39	84.15	92.18

Not detected* indicates that the ImageJ thresholding provided an inaccurate value. In these cases, the actual opacity values were very high, but the software erroneously reported unreasonably low values.

5. MODEL VALIDATION

Using the experimental data collected in the above described experiment, a model validation study was also executed to evaluate the new CFD/DEM modeling capability developed in this work. The following sections: describe the equation set used to model the experiments, describe the details of the modeling domain/mesh to accurately capture the QoI, and present parity plots of the QoI that capture the quality of the comparison. As will be described, the validation focuses on a subset of the experimental cases (with a tilt angle of only 0°) due to time constraints. It should be emphasized that while this validation focuses on the obstructed flow receiver in this project, the complex physics of this receiver type should provide confidence that other receiver variations (e.g. StAIR/multistage trough based FPRs) or other particle technologies can also be evaluated using this capability.

5.1. CFD/DEM Model Description

A description of the CFD/DEM model used in the validation (and previous model sensitivity study in Section 3) is provided here for reference. This model used a Eulerian/Lagrangian framework to capture critical physics within next-generation FPRs. Discrete particles were coupled to a continuum model of the air through source terms in the momentum and energy conservation equations. For brevity, only a subset of the relevant equations for the complete FPR model are included here as they would be too extensive and outside of the scope of this paper. Readers are directed to [14] for a more thorough description of the complete equation set and their corresponding assumptions (specifically if heat and radiation transport were also desired). This section focuses solely on the momentum coupling between the particles and the fluid as it was the most pertinent to addressing the key omissions/simplifications used for particle-to-particle interactions and particle drag.

The Reynolds-averaged Navier Stokes (RANS) equations were used to model the air in and around the receiver. The momentum transport equations were as follows:

$$\frac{\partial \rho u_i}{\partial t} + \frac{\partial \rho u_i u_j}{\partial x_j} = -\frac{\partial p}{\partial x_i} + \frac{\partial}{\partial x_j}\left(\mu\left(\frac{\partial u_i}{\partial x_j} + \frac{\partial u_j}{\partial x_i} - \frac{2}{3}\delta_{ij}\frac{\partial u_I}{\partial x_I} \right)\right) + \rho g_i + F_i + \frac{\partial}{\partial x_j}\left(-\rho\overline{u_i' u_j'}\right) \qquad (1)$$

where ρ was the air density, u_i was the time-averaged air velocity vector, μ was the air dynamic viscosity, p was the pressure, g_i was gravity vector, F_i were external body forces, and $-\rho\overline{u_i' u_j'}$ were the Reynolds stresses. A two-equation turbulence model (e.g. k–ε model) was used to close the equations.

The external body forces F_i were computed from the cumulative particle drag and buoyancy forces within a fluid element of the continuum. Historically, particle drag has been computed assuming flow over isolated particle spheres based on the relative velocity between the particle and the fluid. While this worked well in dilute particle flows, it ignored the effect of lubrication forces between particles created by the presence of an interstitial fluid which became more relevant as the particle volume fraction increased. In this approach, we superimposed lubrication forces with the typical drag effects as shown below. However, while these forces affected the trajectory of the particles, the resulting forces on the fluid domain were equal and opposite and therefore were not included in F_i (assuming a relatively large fluid discretization).

Particle motion for a particle of diameter d_p was determined by:

$$\frac{\partial u_{p,i}}{\partial t} = \frac{3\rho C_D \left|u - u_p\right|}{4\rho_p d_p}\left(u_i - u_{p,i}\right) + \left(\frac{\rho_p - \rho}{\rho}\right) g_i + \sum_M \frac{F_{p,mn}}{m_{p,n}} \qquad (2)$$

where $u_{p,i}$ was the particle velocity vector, ρ_p was the particle density, $|u - u_p|$ was the magnitude of the particle/fluid velocity difference, $F_{p,mn}$ were pairwise particle interaction forces between particle n and m (up to M particles) discussed below, $m_{p,n}$ was the particle mass of particle n, and C_D was the coefficient of drag computed by:

$$C_D = \begin{cases} 24\left(1 + Re_p\right)^{2/3} / Re_p & \text{for } Re_p < 1000 \\ 0.424 & \text{for } Re_p > 1000 \end{cases} \quad \text{where} \quad Re_p = \frac{\rho d_p \left|u - u_p\right|}{\mu} \tag{3}$$

As discussed above, lubrication forces were superimposed on the particle trajectory with Eq. (3) to account for the presence of the interstitial fluid in dense particle flows. They were implemented as pairwise interaction forces using a dissipative force W in pair-wise interactions of particles "1" and "2" as follows:

$$W = -a_{sq}\left|\left(u_{p,1} - u_{p,2}\right) \bullet nn\right|^2 - a_{sh}\left|\left(\omega_{p,1} - \omega_{p,2}\right) \bullet \left(I - nn\right) - 2\Omega_N\right|^2 - a_{pu}\left|\left(\omega_{p,1} - \omega_{p,2}\right) \bullet \left(I - nn\right)\right|^2 \tag{4}$$
$$\text{where} \quad \Omega_N = n \times \left(u_{p,1} - u_{p,2}\right) / r$$

where the terms preceded by a_{sq}, a_{sh}, and a_{pu} represented effects of "squeeze", "shear", and "pump" with the interstitial fluid defined for rigid spheres as they interact in [8]. "Twisting" effects were assumed small and thus excluded. Note that ω_p was the particle angular velocity and r was the distance between the two interacting particles.

Particle-to-particle interactions were also superimposed on the particle motion using a Hertzian granular model where the normal forces on a particle pair F_n were defined by:

$$F_n = \frac{4}{3} E_{eff} R_{eff}^{1/2} \delta_{12}^{3/2} n + F_{n,damp} \quad \text{where}$$
$$\mathrm{E}_{eff} = \left(\frac{1 - \nu_1^2}{E_1} + \frac{1 - \nu_2^2}{E_2}\right)^{-1}, \ \mathrm{R}_{eff} = \frac{R_1 R_2}{R_1 + R_2}, \ \delta_{12} = R_1 + R_2 + \left\|r_{12}\right\|, \ n = \frac{r_{12}}{\left\|r_{12}\right\|} \tag{5}$$

where E_n was the Young's modulus, R was the particle radius, ν was the Poisson ratio, δ was the particle overlap, r was the particle vector separating the two particles, and $F_{n,damp}$ was the normal damping term. As will be shown later, values in Eq. (5) were tuned depending on which particles were interacting (e.g. particle-to-particle, particle-to-obstruction). The damping term was based on a "viscoelastic" model [15] defined by:

$$F_{n,damp} = -\eta_{n0} a m_{eff} u_{n,rel} \quad \text{where} \quad a = \sqrt{R\delta_{12}}, \ m_{eff} = \frac{m_1 m_2}{m_1 + m_2}, \ u_{n,rel} = \left(u_1 - u_2\right) \cdot nn \tag{6}$$

where η_{n0} was the normal damping coefficient, u was the particle velocity, and m was the particle mass. Tangential interaction forces in a particle pair F_t were defined using a Mindlin [16] model:

$$F_t = -\min\left(\mu_t F_{n0}, \left\|F_{te} + F_{t,damp}\right\|\right)\mathrm{t} \quad \text{where}$$
$$F_{n0} = \left\|F_n\right\|, \ F_{t,damp} = -\eta_t u_{t,rel}, \ dF_{te} = -k_t a u_{t,rel} dt \tag{7}$$

where k_t and μ_t were the tangential stiffness and tangential friction coefficient, respectively. The tangential damping coefficient η_t was simply scaled by a constant x_η from η_{n0}, and F_{te} represented an increment of the elastic tangential force. This Mindlin model calculated the accumulated elastic tangential force over the contact history to ensure it did not exceed a critical value. This removed the

dependence of the particle overlap on the tangential force, and if it exceeded this threshold, the tangential force was simply rescaled such that $F_{te} = -\mu_t F_{n0} t + F_{t,damp}$. Additionally, an increment of the elastic tangential force F_{te} was also re-scaled as the contact unloaded as: $F_{te} = F_{te,t_{n-1}}(a/a_{t_{n-1}})$.

Finally, a rolling pseudo-force F_{roll} was applied using a spring-dashpot-slider model [17] as follows:

$$F_{roll} = \min\left(\mu_{roll} F_{n0}, \left\|F_{roll,0}\right\|\right) \mathrm{k} \quad \text{where}$$
$$F_{roll,0} = k_{roll}\xi_{roll} - \gamma_{roll} u_{roll},\ u_{roll} = -R(\Omega_1 - \Omega_2)\times n,\ k = u_{roll}/\|u_{roll}\|,\ \xi_{roll} = \int u_{roll} dt \tag{8}$$

where k_{roll}, γ_{roll}, and μ_{roll} were the rolling stiffness, the rolling damping coefficient, and rolling friction coefficient, respectively. Much like the tangential force model, this model set an appropriate critical value for the pseudo-force which F_{roll} did not exceed. Then, a torque $\tau = R_{eff} n \times F_{roll}$, was applied to the two particles.

At each fluid timestep, Fuego (CFD) solved the momentum conservation equations (Eq. (1)) and passed local fluid properties to LAMMPS (DEM) for each particle to calculate the particle's new trajectory as defined above (Eqs. (2)–(8)). LAMMPS updated particle positions and velocities and returned those values to Fuego where the source terms could be computed for the next timestep. This method leveraged a weak coupling strategy necessitating a small fluid time step. Note that particle positions and velocities often required significantly smaller time steps to properly resolve and LAMMPS executed hundreds or thousands of timesteps for each fluid timestep.

5.2. CFD/DEM Model Setup

Several scripts were written to automate the setup and meshing of the experimental domain for this project. As described in Section 4, there were 5 independent variables that were varied in each experiment including: obstruction type, fall height, particle mass flow rate (or slot width), tilt angle, and plate length. As the entire experiment was not necessary to simulate for model validation under the assumption that edge effects were negligible, periodic boundary conditions were used on a 15 mm wide slice of the experimental setup. The computational domain extended up to a maximum 200 mm below the obstruction. Images of some of final computational domains are depicted in Figure 38.

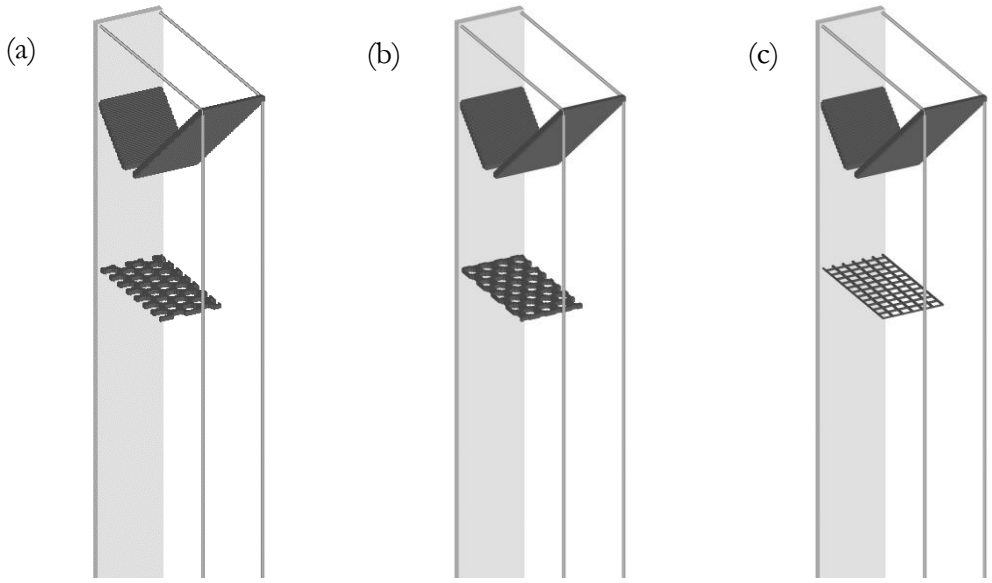

Figure 38. Model validation domain for the perforated plate (parallel; PPP) (a), perforated plate (staggered; PPS) (b), and wire mesh (c) for 30 mm fall heights

The obstruction (either PPP, PPS, or a mesh), the hopper, and the back wall were all created using static particles to simplify the creation of these complex geometric features. In addition to simplifying the meshing requirements on the continuum domain, this also allowed for tuning of the particle/surface interactions using granular models to achieve the right behavior as observed in the experiments. The particles for the hopper and the obstruction both imparted drag on the continuum while the particles for the back wall did not as the back wall was represented in the fluid domain as a simple no-slip boundary condition. However, the particles that comprised the back wall still served as a physical barrier for the DEM model.

Several 100,000, 350 μm diameter CARBOBEAD particles were initialized *below* the obstruction. At the start of each simulation, the particles fell via gravity and were relocated to the top of the domain using a periodic BC (only affecting the particles; not the fluid). After reaching the top of the domain, the particles collected in a hopper with an outlet "slot" profile closely matching that used in the experiments. The hopper accumulated a bed of particles and reset their initial velocity and mass flow rate through the slot to that of the experimental initial condition. The simulation was then allowed to reach steady state (usually requiring at least 1 second of simulation time; more below) at which point the particle velocity and curtain opacity below the obstruction was calculated to validate with experimental measurements. This model set-up was used due to present limitations of the newly developed coupling in which all particles to be used in the simulation must be initialized at $t = 0$.

CARBOBEAD particles are often used as the particle medium in particle-based CSP, and existing numerical and experimental studies using CARBO particles [12] were leveraged here to inform the constants necessary for the granular model above where available. As the elastic modulus was very high necessitating very small time steps for the DEM solves, the decision was made to relax the elastic modulus for computational expediency. The damping coefficient was modified for this relaxed elastic modulus to approximate particle-to-particle and particle-to-surface coefficient of restitutions where available in the literature [12]. The authors' best judgement was used here to make these modifications, and the final values leveraged in the study are reported in Table 12.

Table 12. DEM model inputs used for the CARBO particles, the obstruction, the hopper, and the back wall.

Variable	Value
Elastic Modulus E_{eff} (particles) [MPa]	157
Elastic Modulus E_{eff} (particle/surf.) [MPa]	129
Normal Damping Coefficient η_{n0} (particles) [-]	1×10^{10}
Normal Damping Coefficient η_{n0} (particles/obs.) [-]	1.1×10^{10}
Normal Damping Coefficient η_{n0} (particles/wall) [-]	3.8×10^{9}
Poisson Ratio ν (particles) [-]	0.28
Poisson Ratio ν (particles/surf.) [-]	0.3
Tangential Damping Scaling x_η [-]	1.0
Tangential Friction Coefficient μ_t (particles) [-]	0.53
Tangential Friction Coefficient μ_t (particles/surf.) [-]	0.5
Rolling Stiffness Coefficient k_{roll} (particles) [-]	200
Rolling Stiffness Coefficient k_{roll} (particles/surf.) [-]	200
Rolling Damping Coefficient γ_{roll} (particles) [-]	100
Rolling Damping Coefficient γ_{roll} (particles/surf.) [-]	100
Rolling Friction Coefficient μ_{roll} (particles) [-]	0.37
Rolling Friction Coefficient μ_{roll} (particles/surf.) [-]	0.41

5.3. Validation Results

As described above, time constraints and resources limited the total number of experimental cases that could be evaluated with the model to 12. These cases were limited to those presented in Table 6, Table 7, and Table 10. Cases using a tilt angle of 7° were collected late in the project and not evaluated here. A visualization of a simulation (Case 1) at steady state (t = 2 s) is provided in Figure 39. For this case, the inlet particle mass flow rate and the inlet particle velocity are plotted in Figure 40. To smooth out instantaneous variations in these values when they were post-processed, a moving average was also computed. Note that these plots confirmed that steady state was achieved by at least 1 second of simulation time.

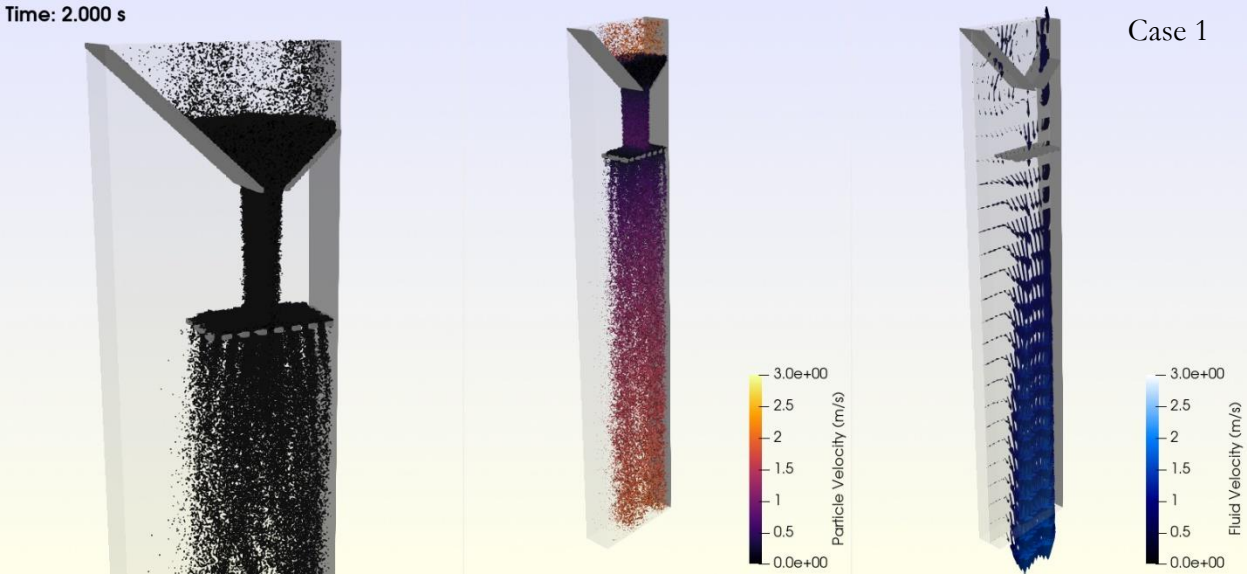

Figure 39. Visualization of a simulation (Case 1) at steady state for a 30 mm fall height, 1.91 kg/s/m, perforated plate (parallel), 0° tilt (left); colored by particle velocity (middle), and with fluid velocity vectors along the midline (right)

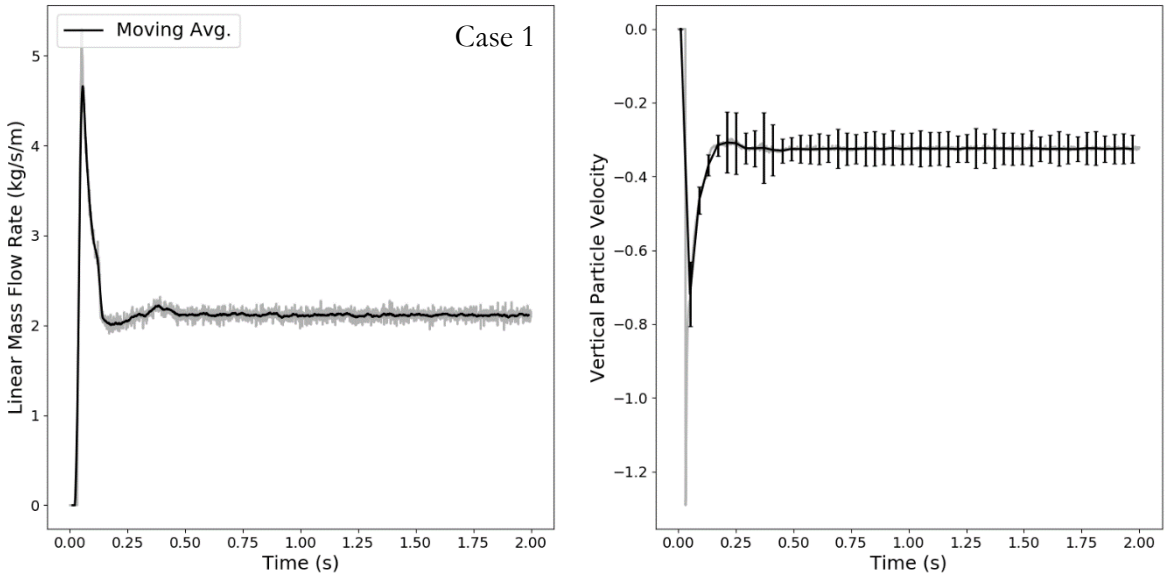

Figure 40. Linear particle mass flow rate in kg/s/m (left) for Case 1 and inlet particle velocity in m/s (right) at the exit of the hopper

As can be seen in the above plots, the particle/hopper granular parameters and its pre-defined slot width (c.f. Figure 39) governed the particle mass flow rate and particle velocity that ultimately impacted the particle plate. These values were tuned to approach experimental values, but still showed slight deviations as observed in the experimental data shown in Table 6. It was deemed that while further adjustments to these values could be made, they were sufficient to properly validate/evaluate the model. The particle velocity and the particle curtain opacity below the obstruction for Cases 1 and 9 is depicted in Figure 41. Here, particle velocities were averaged in 1 mm windows below the obstruction and the particle curtain opacity was evaluated in 20 mm windows. As observed experimentally, the particle velocity deviated slightly below the theoretical

falling velocity (with no drag). This is a different behavior than observed for unconstrained falling particle curtains (with no surrounding walls nearby) [13] suggesting that the effects of particle drag on the falling particle curtain were indeed being captured. For reference, the "theoretical velocity" described in the figures refers to the kinematic equations for falling objects.

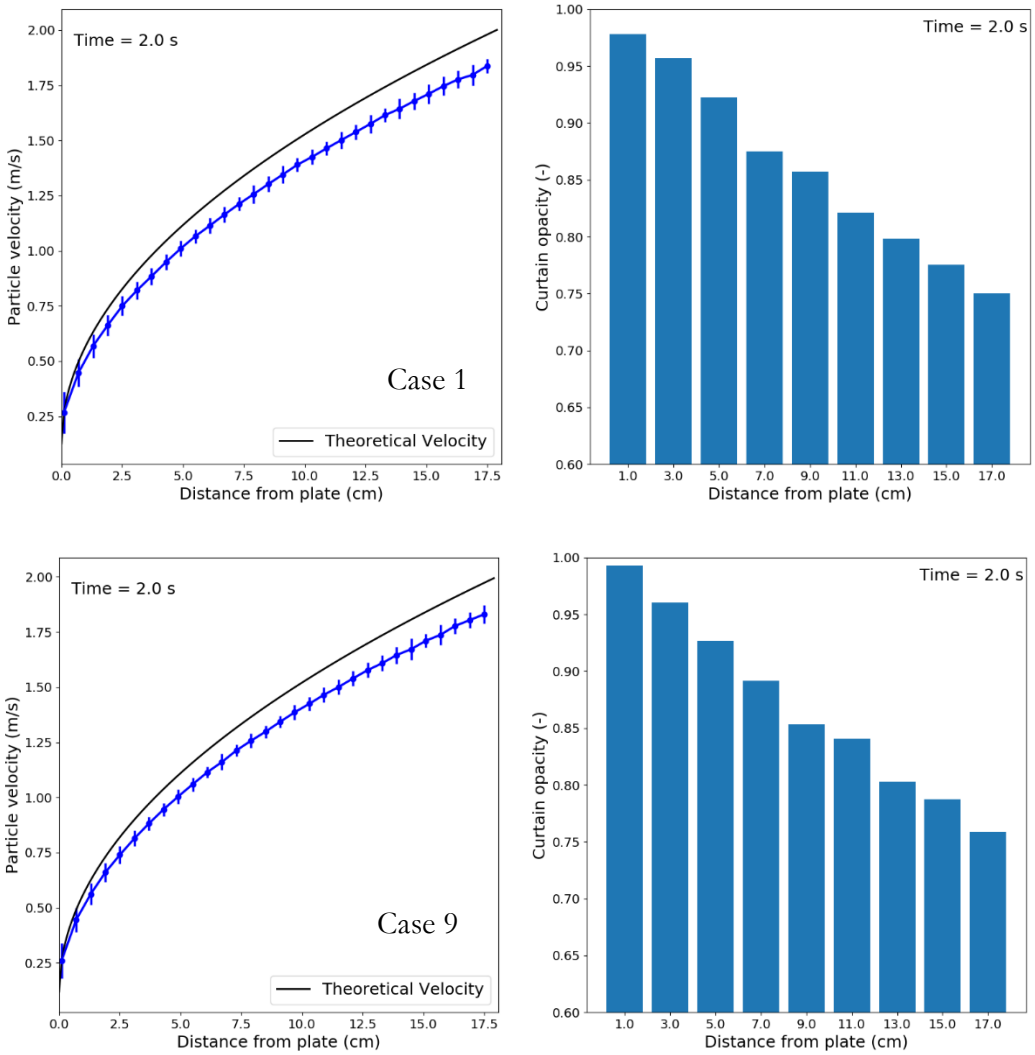

Figure 41. Particle curtain velocity in m/s (left) and curtain opacity in 20 mm windows below the obstruction (right) for the PPP (top; Case 1) and PPS (bottom; Case 9) at 1.91 kg/s/m and 30 mm fall height with 0° tilt

Parity plots of the particle velocity at 20, 40, 60 and 80 mm below the obstruction for each of the 12 cases is presented below in Figure 42. If the model captured all aspects of the experiment perfectly, then all points on the particle plot would follow the line $y = x$ as depicted by the solid black line in the figures. Any scatter in the data can be attributed to experimental or model uncertainty or model form error. In the experiment, the precision uncertainty was assessed to be relatively small from repeated measurements of the same experiment, but the bias uncertainty was more difficult to quantify and thus not included (e.g. since the particles could only be observed from the front of the curtain, particles in front likely biased the particle velocity measurements). In Figure 42, only the model uncertainty was plotted for clarity which was estimated from ±1 standard deviation of the particle velocity in that 1 mm vertical window.

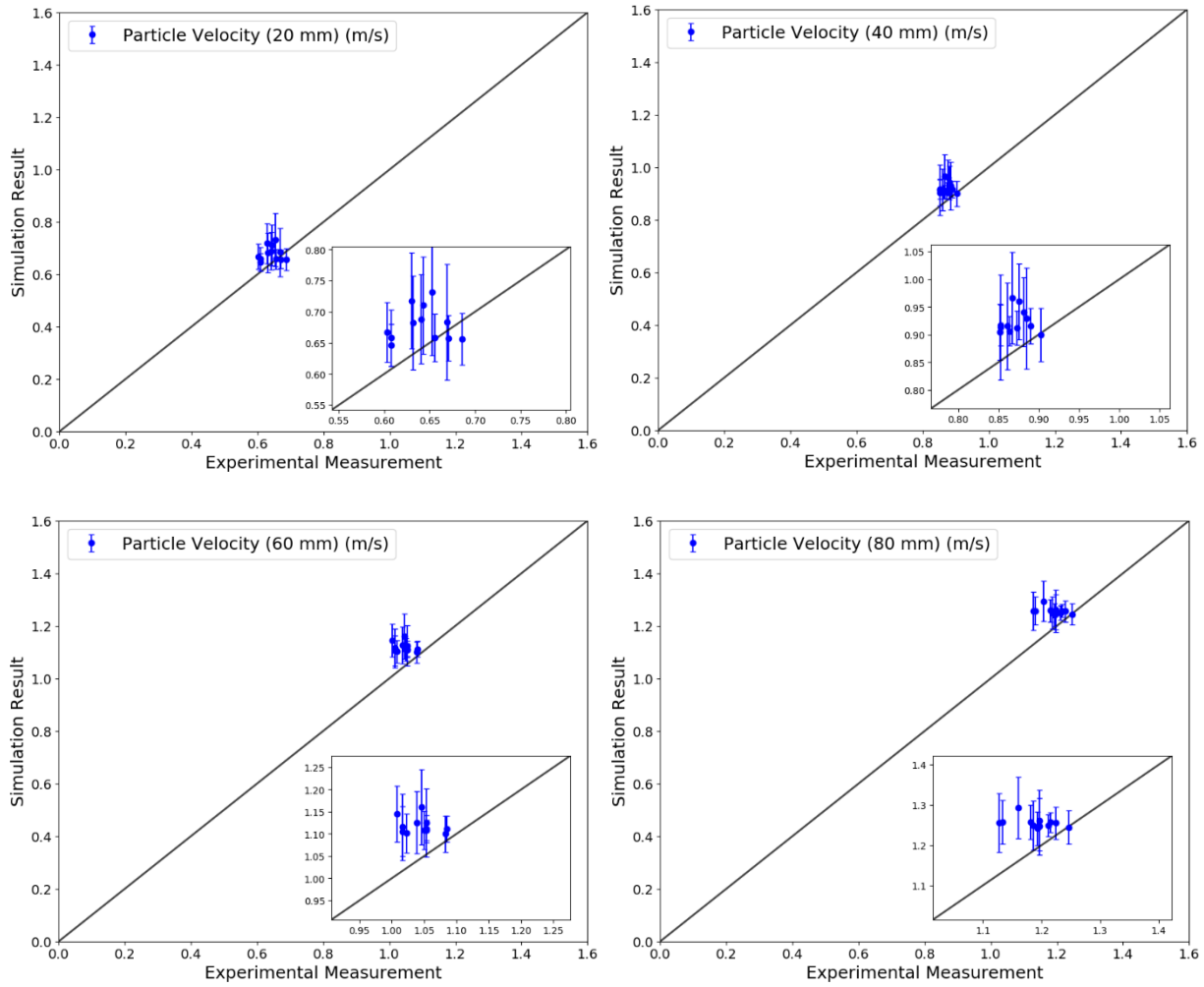

Figure 42. Parity plots comparing the particle velocities after the obstruction at 20, 40, 60, and 80 mm (from left to right, top to bottom)

As shown in the above figures, all experimental cases exhibited a high degree of clustering as would be expected since the solution was primarily driven by gravity as opposed to influence from the obstruction. Unfortunately, the model uncertainty was found to be too high to assess any subtle variations in the particle velocity measured in the experiment for a given height. As a result, it only made sense to evaluate the overall velocity for all four locations with a linear fit on the parity plot as shown in Figure 43. This figure showed that the model provides good overall agreement with the experiment with a slope of 1.044 and a coefficient of determination $R^2 = 0.97$.

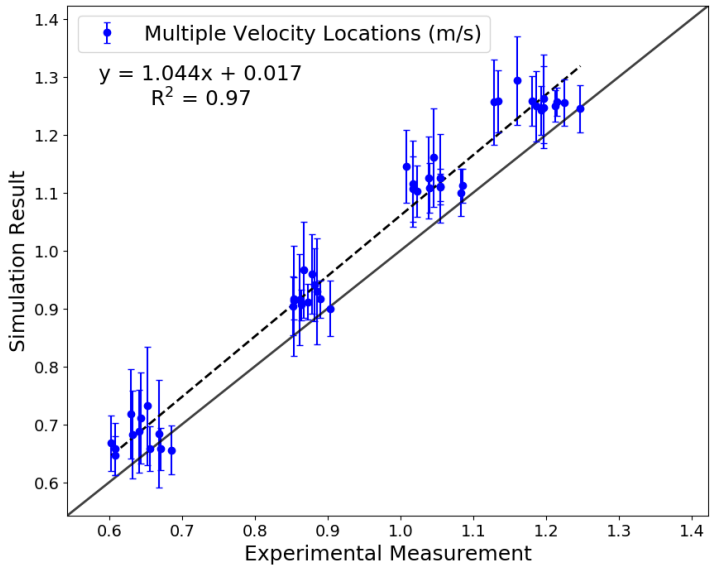

Figure 43. Parity plot of the particle velocities at 20, 40, 60, and 80 mm below the obstruction for each of the 12 experiments

Overall, the results showed good agreement with more deviations observed in the particle velocity as the particles fell beyond 60 mm (i.e. the experiments tended to show slightly higher velocities at longer fall distances). To assess if the particle velocity measurements may have favored particles at the front of the curtain in the PIV analysis, the particle velocity was determined using only the front half of the particle curtain below the obstruction as depicted by the red particles in Figure 44. A parity plots of the particle velocity was again created for 80 mm as shown in the figure. Overall, the results showed that the source of the deviation was not likely attributed to bias from the front particles in the curtain; however, the variability in the particle velocity was found to be lower.

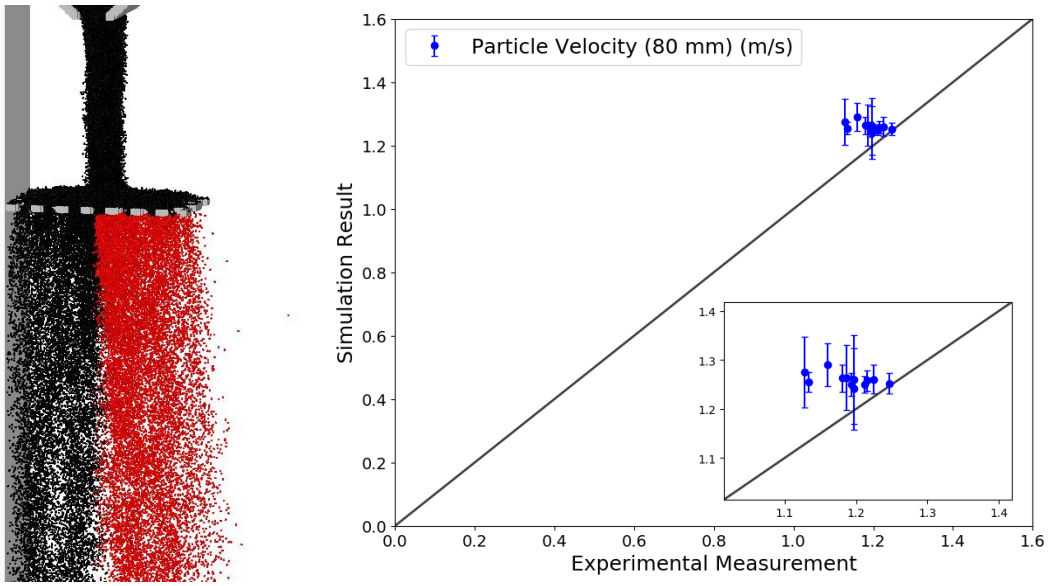

Figure 44. Rendering of a PPP case highlighting the selection of only the forward half of particles for the velocity analysis (in red; left) and a parity plot of the particle velocity at 80 mm below the obstruction (right)

Parity plots of the particle curtain opacity in 20 mm windows below the obstruction at 0-20, 20-40, 40-60 and 60-80 mm for each of the 12 cases is presented below in Figure 45. Model uncertainty was estimated from standard deviation of three calculations of the curtain opacity after the simulations had reached steady state. While the particle velocity compared well with the experiments, the curtain opacity showed significant differences that became more pronounced as the particles continued falling further from the obstructions. In general, the curtain opacity predicted by the model was significantly higher than the experimental measurements. Uncertainty in the experiment nor the simulation explained the differences.

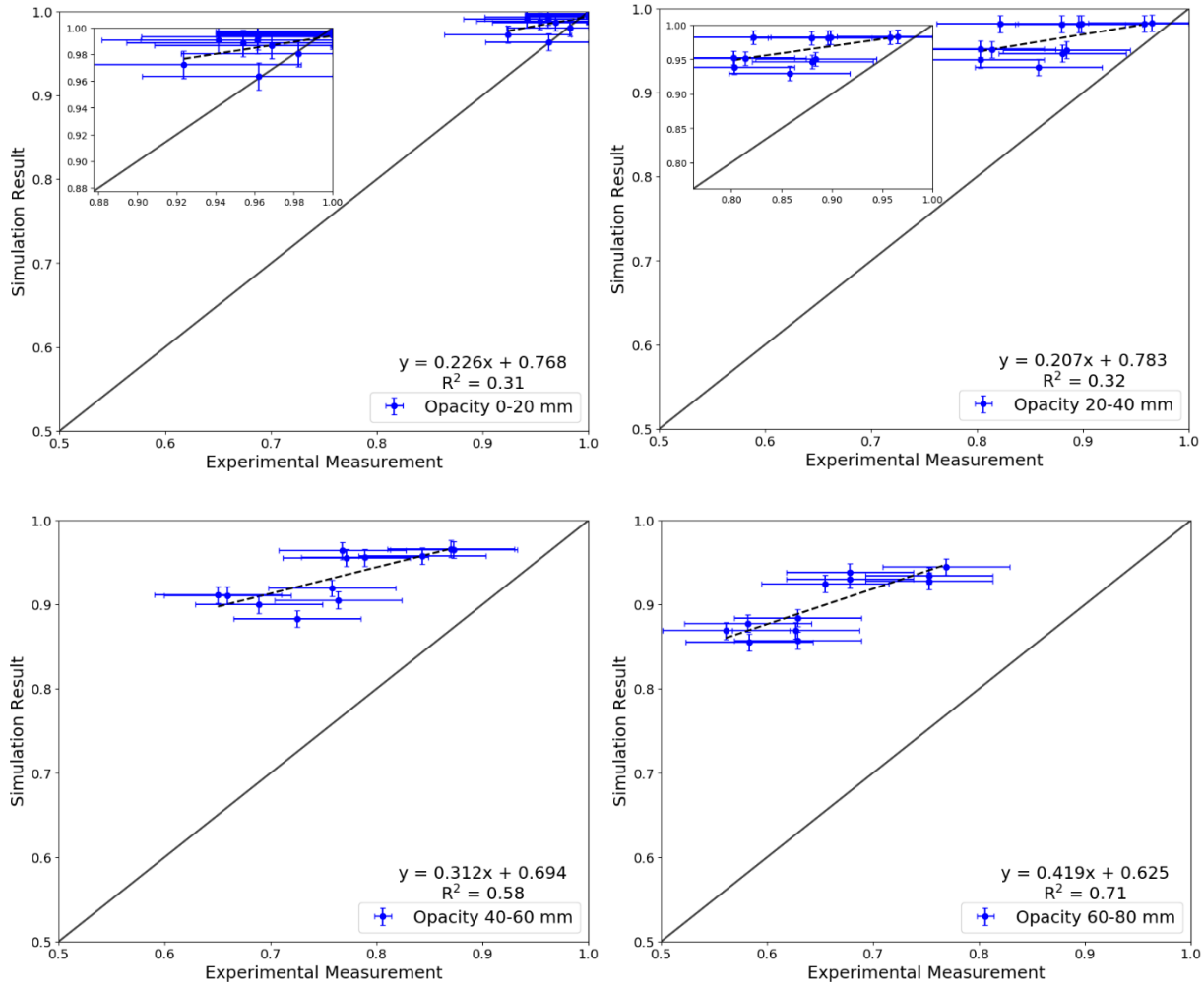

Figure 45. Parity plots comparing the curtain opacity below the obstruction in windows of 0-20, 20-40, 40-60, and 60-80 mm (from left to right, top to bottom)

Ultimately, the differences between the model and experiment were explained by visually comparing the curtain downstream of the obstruction. In Figure 46a, an image from the high-speed video is extracted showing the instantaneous locations of the particles. Likewise, in Figure 46b-d, the instantaneous particle locations are rendered for the PPP and PPS cases (where Figure 46c also visualized the PPS case from the side view). Of note in Figure 46a was that the particles downstream of the obstruction were found to be highly columnar showing a significant effect from the shape of the PP obstruction and low dispersion laterally. Conversely, in Figure 46b, the model showed high uniformity in the particles downstream of the obstruction when viewed from the front; however, as

shown in Figure 46c, the model showed much more columnar flow with significantly less dispersion when viewed from the side. Finally, in Figure 46d, the PPP obstruction also showed similar behavior to the PPS obstruction with the exception of immediately below the obstruction since the holes were aligned when viewed from the front (c.f. Figure 13b).

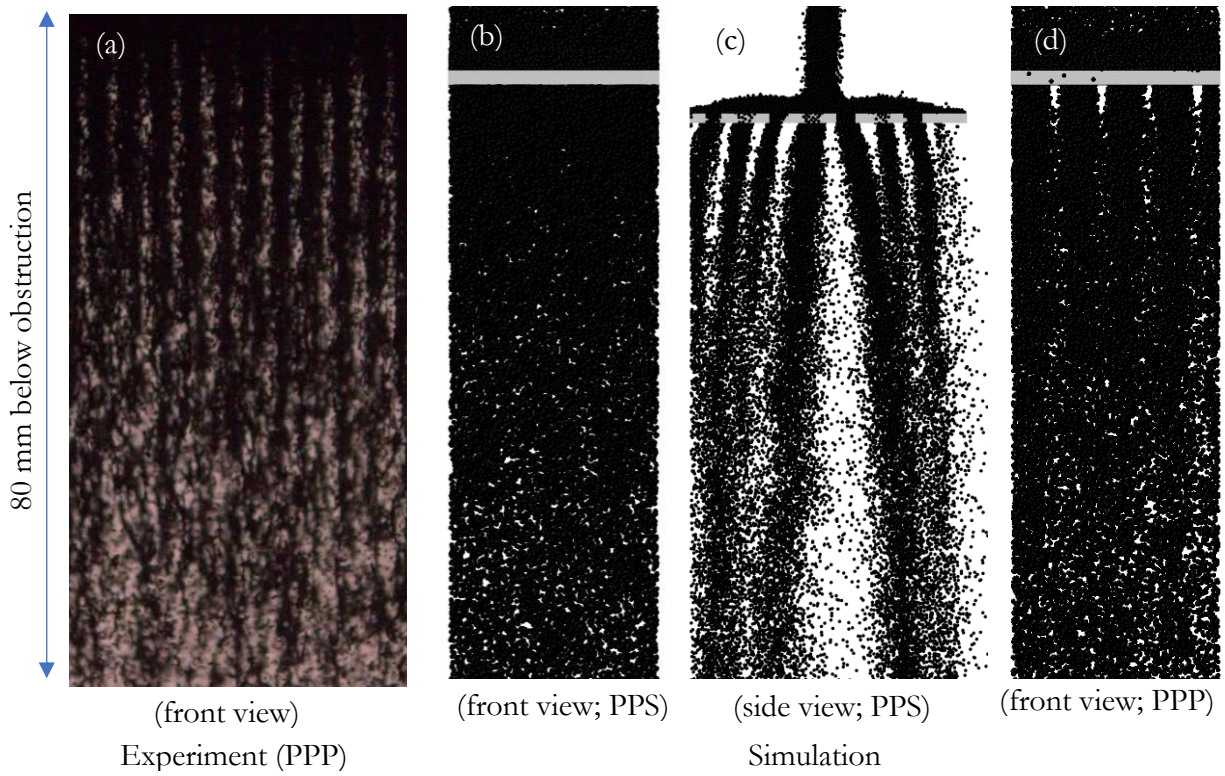

Figure 46. Visual comparison of the particle curtain downstream of the PP obstructions: front view of the PPP experiment (a), front view of the PPS simulation (b), side view of the PPS simulation (c), and front view of the PPP simulation (d)

In short, while some particle clustering was observed from the side, the model did not capture the clustering of the particles when viewed from the front for either PP obstruction. This clustering behavior was concluded to explain the significantly lower opacities observed in the experiment when compared to the simulations. At the time of this report, a satisfactory explanation of the cause of this discrepancy has not been found, but several hypotheses were put forward including: inaccurate turbulent dispersion models for particles, electro-static effects in the experiment, and subtle geometric effects not captured in the model of the obstruction geometry (e.g. the PP was built using particles in the model with an inaccurate radius of curvature for each hole). Resolution of this phenomenon was left as future work.

5.4. Commercial Modeling Capabilities

An effort was also undertaken to evaluate comparable commercial modeling capabilities for this application space using an appropriate set of physics. Two modeling strategies were evaluated within the ANSYS® modeling suite as described below: a two fluid model within Fluent® and a DEM-based model within Rocky®.

5.4.1. Two Fluid Model (ANSYS Fluent)

A "two fluid" model (TFM), also referred to as a Eulerian/granular flow model that was readily available within ANSYS Fluent, was the first modeling strategy evaluated. Prior to simulating particle flow through a PP, a simulation was first performed on a simple geometry to ensure that the model can reasonably capture relevant flow behavior. The first case selected simulated flowing particles released from a rectangular infinite funnel to a platform below it (i.e. a 2D simulation). The mesh along with the specified boundary conditions (BCs) are shown in Figure 47. Simulations were conducted using pressure-based solver settings with gravity.

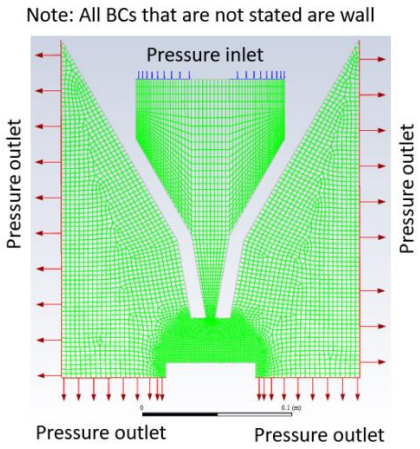

Figure 47. An image of the mesh with assigned boundary conditions for the TFM evaluation

The key physical parameter to be evaluated with this preliminary simulation was the qualitative shape of the resulting particle pile on the platform below the funnel. Several relevant numerical parameters were varied to ascertain their effect on the shape of the pile in this model framework: (1) coefficient of restitution (CoR) between particles (granular phase), (2) friction packing limit (FPL) of the particles, and (3) the wall boundary condition between the particles and the wall (through the specularity coefficient (SC)). It was found that CoR and FPL had the biggest impact on the shape of the particle pile. First, a lower CoR resulted in particle pile with a more clearly defined shape. As shown in Figure 48, from the three values that were explored (0.9, 0.5, and 0.3), 0.9 yielded unphysical bouncing that did not correspond with physical observations. Thus, only a very small pile was formed. Very little qualitative difference was observed when comparing the smaller CoR values.

Decreasing the FPL caused the pile to be taller/slimmer, which may be attributed to the increase of friction between particles (Figure 49). The FPL was defined as the particle volume fraction at which shear friction between particles was activated in the model; thus, a lower FPL means that this friction force occurred earlier in the formation of pile.

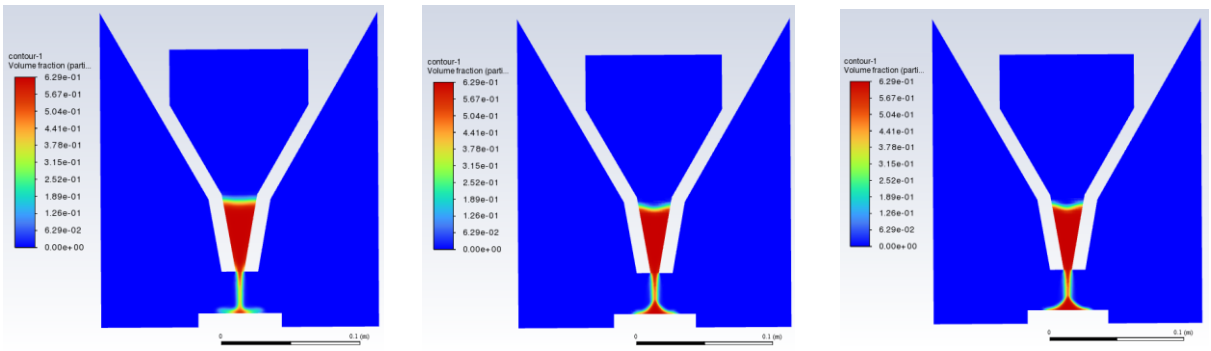

CoR: 0.9 CoR: 0.5 CoR: 0.3

Figure 48. Particle volume fraction contour plots for various CoR values; all are taken at flow time of around 0.1 s with FPL and SC of 0.61 and 0.25, respectively

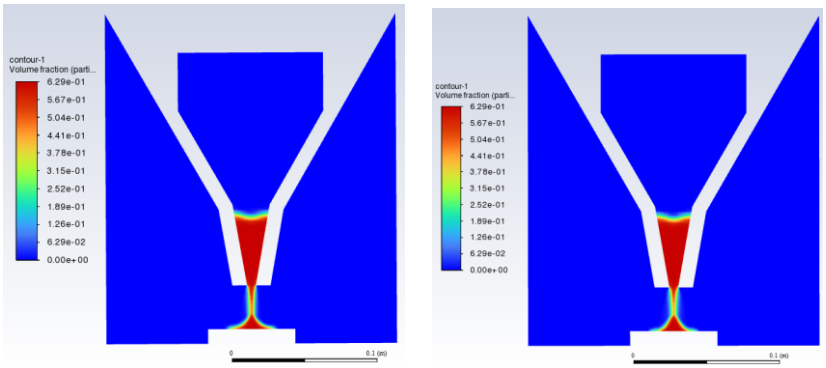

FPL: 0.61 (default) FPL: 0.4

Figure 49. Comparison of particle pile obtained from two different FPL values at flow time of around 0.1 s; CoR and SC used are 0.5 and 0.75, respectively

For the SC, two values were explored for the platform surface: 0.25 and 0.75. However, the results from both values were similar. The SC was a normalized value from 0 to 1 where 0 represents perfectly specular particle collisions and 1 represents perfectly diffuse particle collisions. Some literature reported using a SC of 1 was representative of a no-slip wall boundary condition [18]. Despite these encouraging results, one observation with this modeling strategy was that the particle pile as defined by the particle volume fraction continued to flow after the funnel above the platform emptied (i.e. ultimately, the particle pile became nearly flat).

After identifying appropriate parameters that yielded a realistic particle pile for flowing particles (CoR: 0.5; FPL: 0.4; and SC: 1), a simulation of particles flow through a PP was conducted. The results showed the potential of using Eulerian Granular model for such a flow (c.f. Figure 50); however, the calculation diverged repeatably which required decreasing relevant under-relaxation factors until the simulation could proceed. It was speculated that this was caused by the small size of cells near the obstruction to capture the curvature of the PP holes; therefore, a smaller time-step-size might be needed for a more stable calculation. This would significantly increase the computation expense, and it was deemed that the benefits of a TFM were outweighed by simply using a DEM-based model also available in ANSYS.

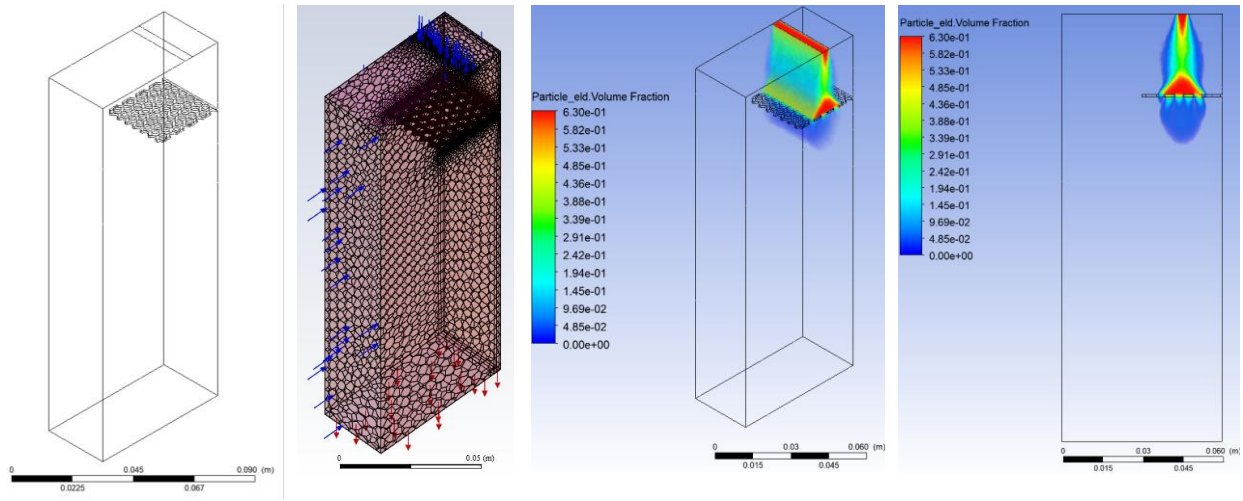

Figure 50. Simulation of particles flowing through a PP; from left to right: geometry, mesh, and contour plot of the particle volume fraction at 0.009960 s

5.4.2. DEM Model (ANSYS Rocky)

A DEM-based approach was also explored using ANSYS Rocky, a commercial DEM software that was recently integrated within ANSYS. It was formerly known as Rocky DEM, a subsidiary of Engineering Simulation and Scientific Software (ESSS). Rocky also included coupling with the CFD software, Fluent, to provide a more complete CFD/DEM capability. However, for the simulations performed here, the fluid effects were excluded due to limited computational resources. Including the effect of fluid coupling was left as future work.

5.4.2.1. Modeling the Static Angle of Repose (SAOR)

Like the TFM model evaluation above, the DEM-based model was evaluated first on a simple problem to ensure appropriate values have been selected. The static angle of repose (SAOR) from experiments (hollow cylinder method) were used as a metric of comparison [19]. To limit the scope of the study, only three parameters were initially assessed: (1) the coefficient of rolling resistance ($CoRR$), (2) the particle-particle coefficient of restitution (CoR_{pp}), and (3) the particle-particle dynamic friction coefficient ($\mu_{d,pp}$). Other parameters were kept constant (e.g. particle-particle static friction coefficient ($\mu_{s,pp}$), particle-boundary static and dynamic friction coefficients ($\mu_{s,pb}$ and $\mu_{s,pb}$), etc.).

In this work, SAOR was defined by the arctan of the ratio of the particle pile height to the radius of the base. Spherical CARBOBEAD particles with an average diameter of 300 μm were used. Loose density of the particles, ρ_p, was measured and utilized in the simulation, which value was 1796±2.3 kg/m^3. The modulus of elasticity used for the particles (E_p) and boundaries (E_b) were 0.1 and 1 GPa, respectively. These were lower than real values but selected based on computational expense. Chen et al. [20] has found that scaling E_p down as low as $0.001E_p$ did not affect the solution. Similar conclusions were also drawn by Yan et al. [21]; in their work, E_p was varied from 0.02-200 GPa. All properties explored for these simulations are summarized in Table 13. Adhesive forces were assumed to be insignificant because the particles were dry and sufficiently large.

Table 13. Parameters used in ANSYS Rocky simulations

Parameters	Values
Coeff. of rolling resistance, $CoRR$	0.1, 0.2, 0.3
Coeff. of restitution of particle-particle, CoR_{pp}	0.3, 0.5, 0.7
Coeff. of restitution of particle-boundary, CoR_{pb}	0.3
Static friction coeff. of particle-particle, $\mu_{s,pp}$	0.7
Static friction coeff. of particle-boundary, $\mu_{s,pb}$	0.7
Dynamic friction coeff. of particle-particle, $\mu_{d,pp}$	0.4, 0.7
Dynamic friction coeff. of particle-boundary, $\mu_{d,pb}$	0.7
Modulus of Elasticity of particle, E_p [GPa]	0.1
Modulus of Elasticity of boundary, E_b [Gpa]	1
Density of particle, ρ_p [kg/m^3]	1796
Diameter of particle, d_p [mm]	0.3
Poisson's ratio of particle, ν_p	0.3
Poisson's ratio of boundary, ν_b	0.3

A scaled down version of the experimental setup was used to reduce the computation expense (by a factor of 0.15). In this problem, a hollow cylinder was placed on a base and then filled with particles. Then, the cylinder was lifted at a given speed creating a pile on the top of the base (c.f. Figure 51). The speed of lifting of the cylinder for the simulations was determined by scaling down the mass flow rate of particle flowing out of the cylinder with appropriate scaling. The differences between the experiment and the simulation are summarized in Table 14.

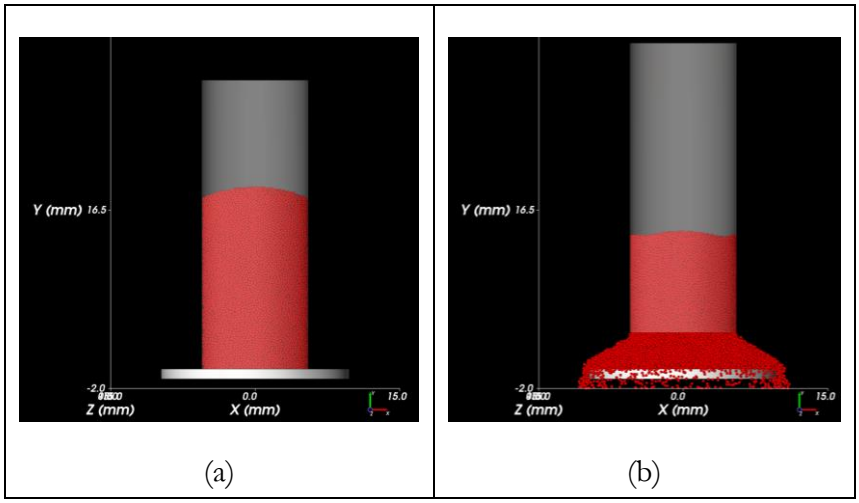

Figure 51. Hollow cylinder filled with particles in the simulation (ANSYS Rocky): before (a) and during the lifting of the cylinder (b)

Table 14. Dimensions and cylinder speed comparison between experiment and simulation.

	Cylinder inner diameter, D_{cyl} [mm]	Cylinder height, H_{cyl} [mm]	Cylinder speed, V_{cyl} [mm/s]	Base diameter, D_{base} [mm]
Experiment, exp	74.0	200.0	1.15	130.0

Simulation, sim	11.1	30.0	7.67	19.5

It was found that the CoRR had a significant effect on the resulting SAOR of the particle pile. A rolling resistance model (like that described above in the SIERRA/LAMMPS simulations: Eq. (8)) creates a moment that counters the rolling motion of a particle representative of non-sphericity or surface irregularities on two interacting particles. Two rolling resistance models were available in ANSYS Rocky: (1) Type A: constant moment and (2) Type C: linear spring rolling limit. The latter was used here. The CoRR was varied from 0.1-0.3, whereas CoR_{pp} and $\mu_{d,pp}$ were fixed at 0.3 and 0.7, respectively. The other parameters were constant as shown in Table 13. Figure 52 shows that the final SAOR increases with increasing CoRR. Photos of the particle pile from the experiment in [19] also showed that a CoRR=0.2 in the simulations provided the best agreement although some curvature in the particle pile was observed.

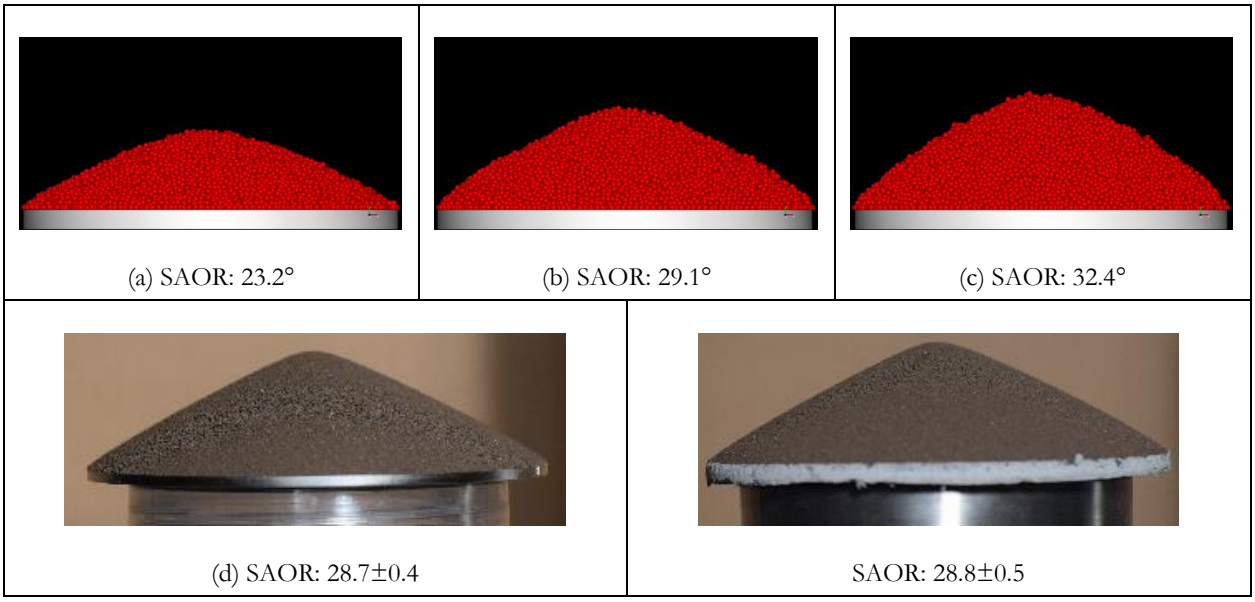

(a) SAOR: 23.2° (b) SAOR: 29.1° (c) SAOR: 32.4°

(d) SAOR: 28.7±0.4 SAOR: 28.8±0.5

Figure 52. Comparison between experiment and simulation of SAOR generated via hollow cylinder method for different CoRR: (a) 0.1, (b) 0.2, and (c) 0.3; (d) and (e) are experiment results on stainless steel (smooth) and ceramic concrete (rough) base [19].

Three different values of CoR_{pp} (0.3, 0.5, and 0.7) were also varied to see its effect on the SAOR. Values of $CoRR$ and $\mu_{d,pp}$ were fixed at 0.2 and 0.7, respectively. As shown in Figure 53, variation of the CoR_{pp} had a minimal effect on the SAOR. However, the curvature of the particle pile profile seen in Figure 52 decreased as CoR_{pp} increased.

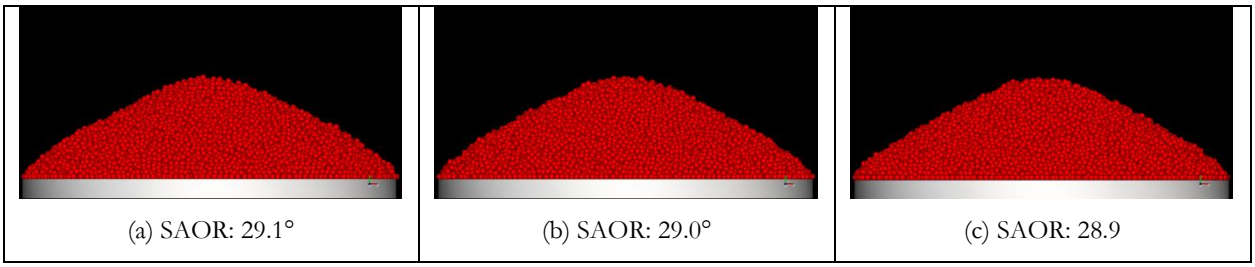

(a) SAOR: 29.1° (b) SAOR: 29.0° (c) SAOR: 28.9

Figure 53. Comparison of simulated SAOR using hollow cylinder method for different CoR_{pp}: (a) 0.3, (b) 0.5, and (c) 0.7.

It was also found that $\mu_{d,pp}$ had a minor effect on the SAOR. As shown in Figure 54, the SAOR increased by 4.7% (27.8° to 29.1°) as $\mu_{d,pp}$ increased from 0.4 to 0.7; thus, a higher friction coefficient gave a steeper angle of repose. However, it should be emphasized that there is some ambiguity in the SAOR measurements as it required visually specifying the peak of the particle pile (i.e. there is some unquantified uncertainty in the SAOR values reported here).

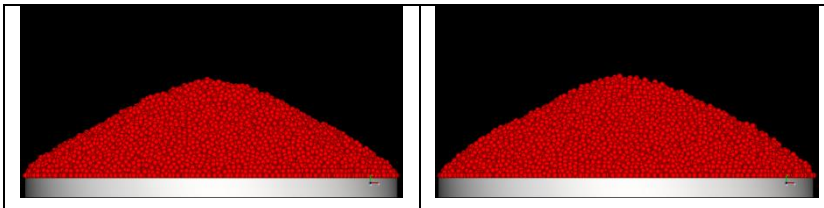

(a) SAOR: 27.8° (b) SAOR: 29.1°

Figure 54. Comparison of simulated SAOR using hollow cylinder method for different $\mu_{d,pp}$: (a) 0.4 and (b) 0.7.

5.4.2.2. Simulating Flow through a Perforated Plate

Finally, a preliminary simulation has been performed on a single perforated plate (PP) to evaluate capabilities of using it for obstructed flow receiver design. Moreover, results from the experiment described in Section 4 were used to validate the simulation. Based on the simulation results above, a $CoRR$ of 0.2 was used here. Other values used in the simulation are provided in Table 13 where CoR_{pp} and $\mu_{d,pp}$ were found to have a minimal effect on the final SAOR solution.

The geometry used in this simulation was based on the experimental setup (Figure 12 and Figure 13). The width of the simulation domain was set to 8.6 mm and periodic boundary conditions were applied to the sides (Figure 55). Unlike the simulations described in Section 5.2, the obstruction was modeled explicitly using wall boundary conditions where complex geometries could be more easily represented. Only the PPS obstruction was evaluated. The fall height and tilt angle of the experiment were 30 mm and 0°, respectively. The mass flow rate was set to 1.91 kg/s/m corresponding to Case 9 in Table 6, Table 7, and Table 10.

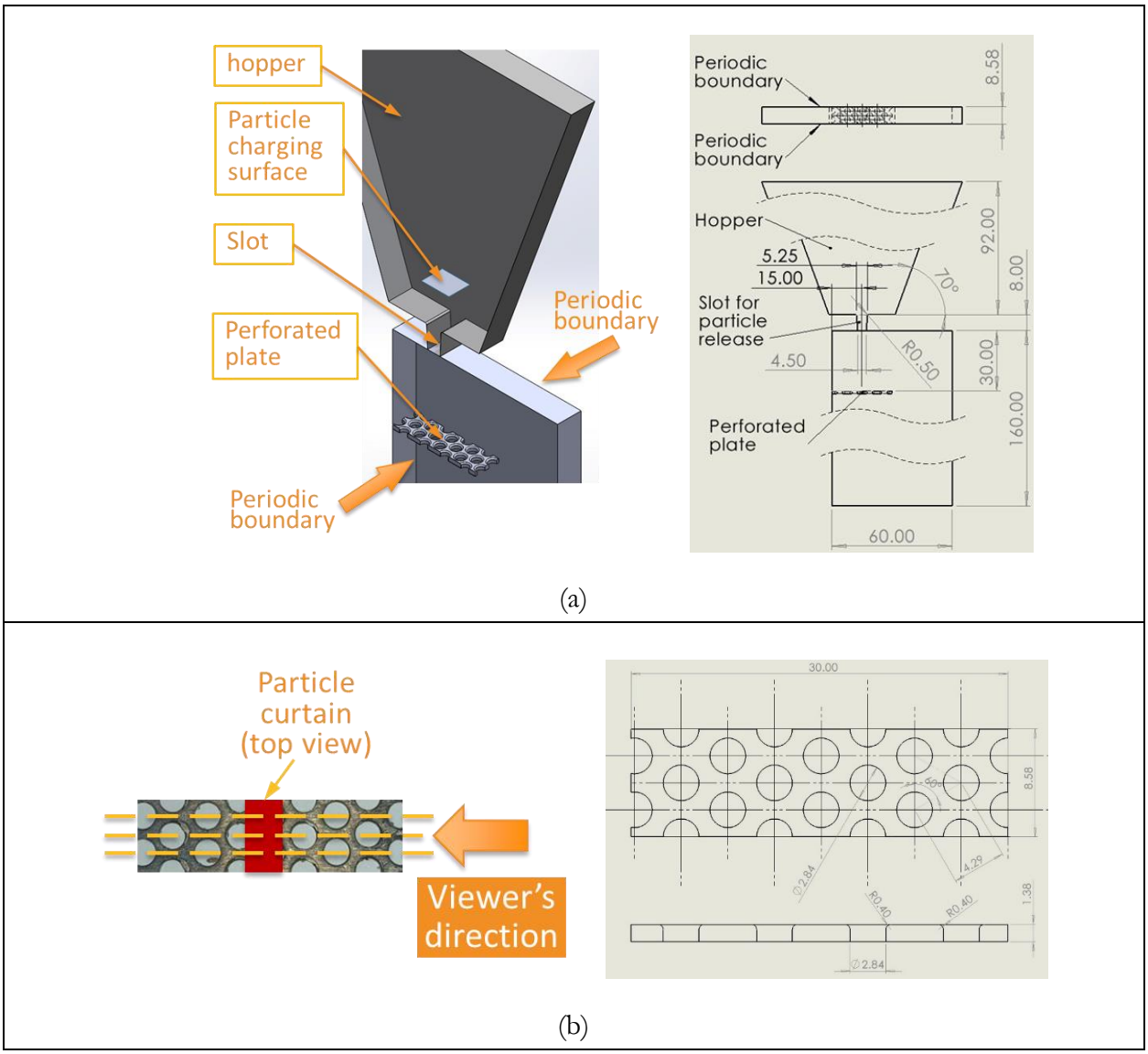

Figure 55. Geometry used for the simulation: the overall domain (a) and PPS obstruction (b)

The particles in the hopper were charged using a small surface inside the hopper referred to here as the particle charging surface. Once the hopper was sufficiently full, the bottom wall of the hopper slot was opened to release the particles. When the particle level inside the hopper reached the charging surface, additional particles were no longer added to the simulation domain. However, particles were again added as the particle inventory in the hopper fell to maintain a consistent particle flow. To match the mass flow rate with that of the experiment, the size of the upper section of the slot was adjusted, whereas the lower section followed the actual/measured. It was found that a slot width of 5.25 mm yielded the appropriate particle mass flow rate. The actual/measured slot size was 5 mm and 4.5 mm on the upper and lower sections, respectively (the slot included a taper through the thickness). The measured thickness of the slot plate was ~8 mm.

The "hysteretic linear spring" and "linear spring Coulomb limit" models were used for the normal and tangential forces, respectively. The implemented rolling resistance model was the "Type C:

Linear spring rolling limit". As done in the SAOR simulation previously, adhesive forces were assumed to be negligible.

Visually comparing the solution of the simulation when it reached steady state with the experiment of the simulation clearly showed some significant discrepancies at the leading edge of the PP. While some experiments with high flow rates (2.5 kg/s/m) observed particles overflowing the leading edge, Case 9 with a particle mass flow rate of 1.91 kg/s/m did not. However, as shown in Figure 56, particles were found to overflow the leading edge.

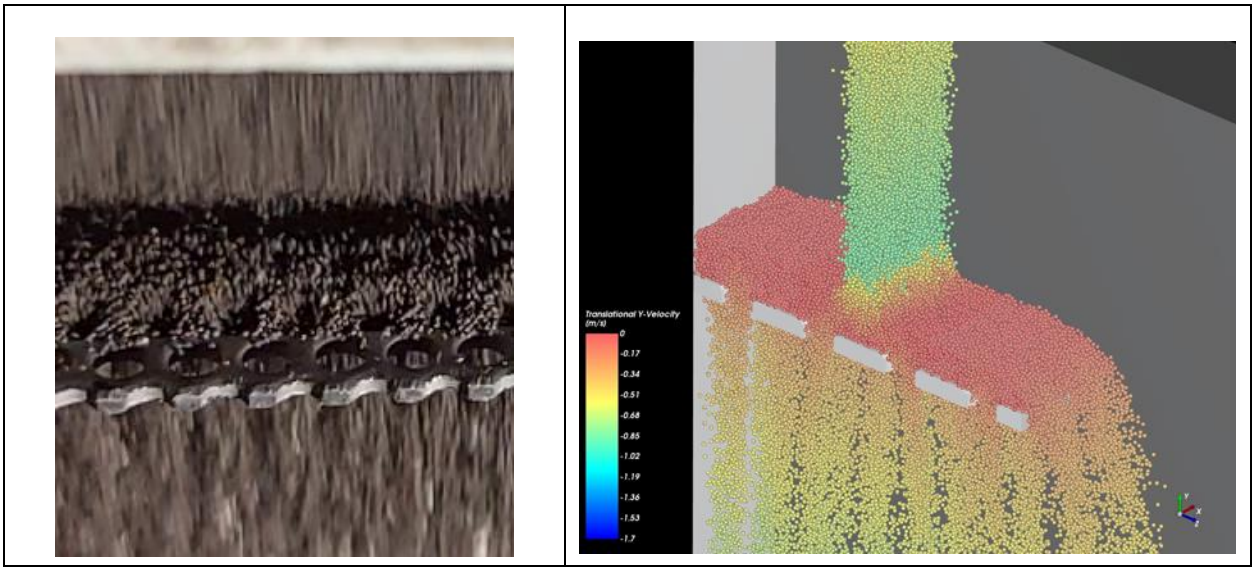

Figure 56. Visual comparison of the particle flow on Case 9 for the experiment (left) and the simulation (right)

Above the obstruction, the vertical velocity increased as the particles fell before decelerating when approaching the packed bed (particle pile) on top of the obstruction. In the simulation, the particles were found to start decelerating at 24 mm from the release point. This distance was equivalent to 6 mm above the top obstruction surface. As shown in Figure 57, this closely matched the experimental results of 22-23 mm (i.e. 7-8 mm above the obstruction). The packed bed height was predicted to be around 3.6 mm above the obstruction as shown in Figure 57c. From Figure 57b, it was found that the effect of drag was negligible as the vertical velocity closely matches that predicted by simple kinematic equations (theoretical). Since the DEM simulation was not presently coupled with a CFD simulation, this result was expected.

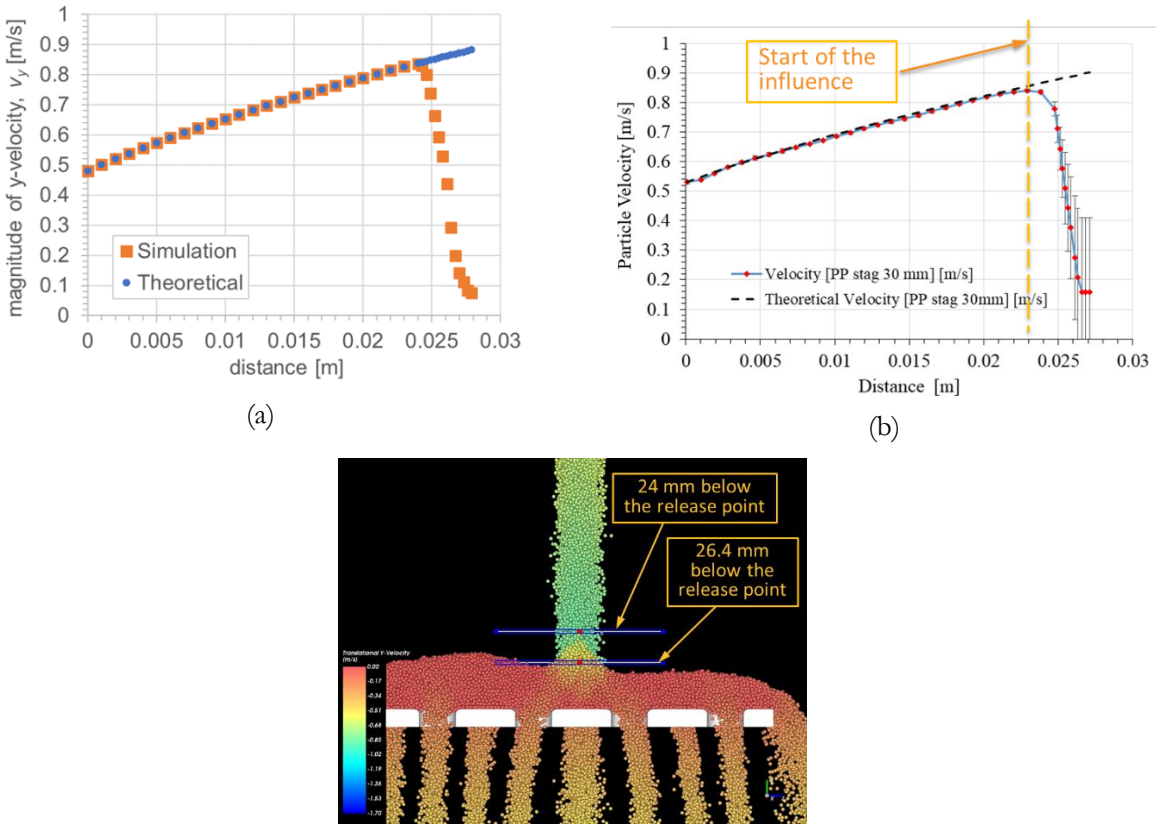

Figure 57. Plot of the particle velocity above the obstruction for the simulation (a) and the experiment (b). A magnified view of the simulation result near the packed bed (c).

Similarly, for particle flow below the obstruction, the vertical velocity profile in the simulation closely followed the theoretical/kinematic value as shown in Figure 58a. Therefore, particle-particle interactions were found not to affect the downstream vertical particle velocity: only drag (Figure 58a). At around 90 mm below the obstruction, both, the simulation and the kinematic overpredict the velocity by ~5.4%. It should be noted that the velocities from the simulation that are plotted in Figure 58a were taken at locations shown in Figure 58b. This calculation of the average particle velocity does not include any particles deeper into the curtain (although this was found to have a minimal effect in previous analysis; c.f. Figure 44).

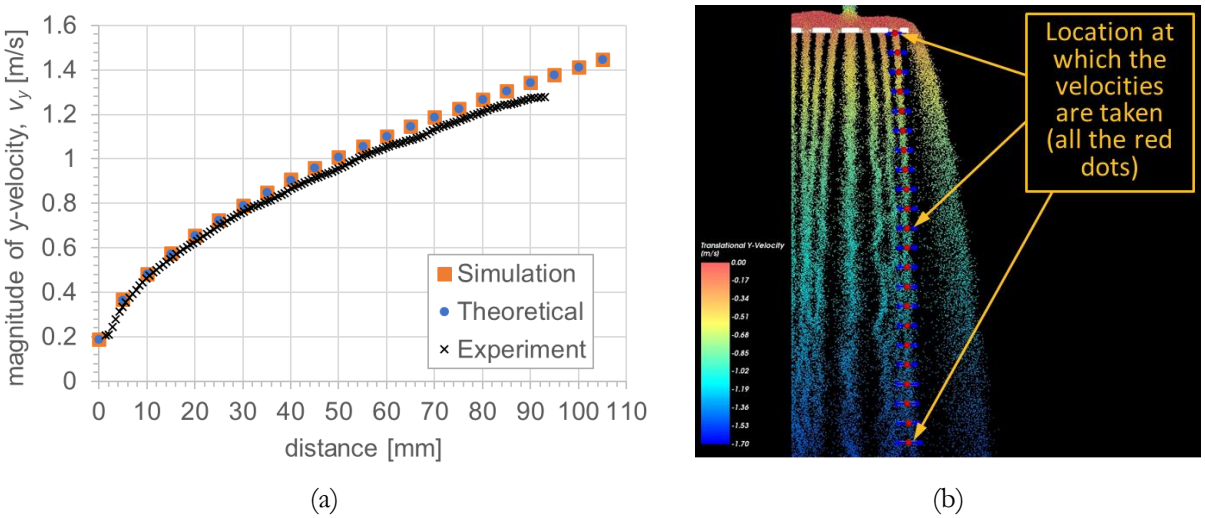

Figure 58. (a) Velocity vs. vertical distance below the obstruction and (b) locations at which the predicted velocities are taken for the plot.

Since significant deviation in the overall particle flow was observed in these simulations, the particle curtain opacity was not calculated and compared as the results would be significantly different than those measured in the experiment. Moreover, excluding drag from the air resulted non-trivial errors in the particle velocity profile downstream of the obstruction.

Ultimately, as can be seen from these preliminary simulations, using a DEM approach via ANSYS Rocky provided a more realistic particle flow behavior compared to using a Eulerian granular flow model (TFM) as described in Section 5.4.1. Additionally, the ability to couple with the CFD package ANSYS Fluent provides a very useful simulation capability. While additional tuning of the granular model is necessary, future work will be utilizing DEM-based models as a key tool in developing the next-generation obstructed flow particle receivers.

6. SUMMARY

This report summarized a recent project aimed at developing and validating the necessary tools to enable more accurate modeling of denser and more complex particle flows in next-generation particle receivers used in concentrating solar power towers. A newly developed CFD/DEM simulation capability was created by coupling existing the modeling and simulation tools Sierra and LAMMPS. This new capability permitted the inclusion of more complex physics for particle drag and particle collisions to model complex flow features expected in next generation receivers.

Two verification tests were executed to evaluate the new modeling capability: a test to ensure conservation of momentum after particle collisions and a test to ensure appropriate qualitative behavior in two closely interacting particles with drag (a modified drafting-kissing-tumbling problem). Both tests supported successful coupling. A model sensitivity study was then executed with the new capability to assess the impact of the uncertainty in DEM model parameters with quantities of interest (QoI) for an obstructed flow particle receiver: particle velocity after an obstruction and particle curtain opacity. The study demonstrated that the impact of the DEM parameters was outweighed by the simulation boundary conditions (e.g. obstruction, particle mass flow rate).

An experimental campaign was undertaken to measure the relevant QoI for an obstructed flow particle receiver that could be leveraged for validation of the modeling capability. A total of 18 experiments were performed varying the obstruction type, the particle mass flow rate, the angle of the obstruction, and the particle fall distance. The particle velocity was measured before and after the obstruction using particle image velocimetry and the particle curtain opacity was measured using line-of-sight measurements of the instantaneous particle positions. Models of these experiments were created using the new simulation capability and evaluated using the measured QoI. Results showed that while the particle velocity downstream of the obstruction was captured by the simulations, the particle curtain opacity was overestimated. Additional physical phenomenon yet unidentified were suspected to have caused the discrepancy between the model and the experiments. Finally, two commercial modeling capabilities were evaluated for this application space using the ANSYS® code suite. Results showed that DEM-based models within ANSYS provided the necessary modeling capabilities for next-generation receiver design.

7. REFERENCES

[1] Office of Energy Efficiency & Renewable Energy; Solar Energy Technologies Office, Generation 3 Concentrating Solar Power Systems (Gen3 CSP) Phase 3 Project Selection, 2021. https://www.energy.gov/eere/solar/generation-3-concentrating-solar-power-systems-gen3-csp-phase-3-project-selection. (Accessed December 13, 2021.

[2] Ho, C.K., 2016, "A review of high-temperature particle receivers for concentrating solar power", Applied Thermal Engineering, 109, pp. 958-969, B. DOI: 10.1016/j.applthermaleng.2016.04.103

[3] Ho, C.K., Sment, J., Albrecht, K.J., Mills, B., Schroeder, N., Laubscher, H., González-Portillo, L.F., Libby, C., Pye, J., Gan, P.G., Wang, Y., Gen 3 Particle Pilot Plant (G3P3) – High-Temperature Particle System for Concentrating Solar Power (Phases 1 and 2), Sandia National Laboratories, November 2021

[4] Mills, B., Shaeffer, R., Yue, L., Ho, C.K., 2020, "Improving Next-Generation Falling Particle Receiver Designs Subject to Anticipated Operating Conditions", ASME 2020 14th International Conference on Energy Sustainability, Virtual Online Conference, June 17–18. DOI: 10.1115/ES2020-1667

[5] Al-Ansary, H., El-Leathy, A., Jeter, S., Djajadiwinata, E., Alaqel, S., Golob, M., Nguyen, C., Saad, R., Shafiq, T., Danish, S., Abdel-Khalik, S., Al-Suhaibani, Z., Abu-Shikhah, N., Haq, M.I., Al-Balawi, A., Al-Harthi, F., 2018, "On-Sun Experiments on a Particle Heating Receiver with Red Sand as the Working Medium", AIP Conference Proceedings, 2033(1), p. 040002 (8 pages). DOI: 10.1063/1.5067038

[6] Siegel, N.P., Ho, C.K., Khalsa, S.S., Kolb, G.J., 2010, "Development and evaluation of a prototype solid particle receiver: On-sun testing and model validation", Journal of Solar Energy Engineering, 132(2), p. 021008 (8 pages). DOI: 10.1115/1.4001146

[7] Thompson, A.P., Aktulga, H.M., Berger, R., Bolintineanu, D.S., Brown, W.M., Crozier, P.S., Veld, P.J.i.t., Kohlmeyer, A., Moore, S.G., Nguyen, T.D., Shan, R., Stevens, M.J., Tranchida, J., Trott, C., Plimpton, S.J., 2022, "LAMMPS - a flexible simulation tool for particle-based materials modeling at the atomic, meso, and continuum scales", Computer Physics Communications, 271, p. 108171. DOI: 10.1016/j.cpc.2021.108171

[8] Ball, R.C., Melrose, J.R., 1997, "A simulation technique for many spheres in quasi-static motion under frame-invariant pair drag and Brownian forces", Physica A: Statistical Mechanics and its Applications, 247(1), pp. 444-472. DOI: 10.1016/S0378-4371(97)00412-3

[9] Edwards, H.C., Stewart, J.R., 2001, "Sierra, a software environment for developing complex multiphysics applications", First MIT Conference on Computational Fluid and Solid Mechanics.

[10] Yue, L., Schroeder, N., Ho, C.K., 2020, "Particle Flow Testing of a Multistage Falling Particle Receiver Concept: Staggered Angle Iron Receiver (StAIR)", ASME 2020 14th International Conference on Energy Sustainability, Virtual Online Conference, June 17–18. DOI: 10.1115/ES2020-1666

[11] Akiki, G., Moore, W.C., Balachandar, S., 2017, "Pairwise-interaction extended point-particle model for particle-laden flows.", Journal of Computational Physics, 351(4), pp. 329-357. DOI: 10.1016/j.jcp.2017.07.056

[12] Yarrington, J.D., 2020,"Numerical and Experimental Analyses of Room and High Temperature Dense, Granular Flows Coupled to Flow Property Measurements for Solar Thermal Energy Storage", Georgia Institute of Technology, p. 134.

[13] Ho, C.K., Romano, J.M.C.D., Yellowhair, J., Siegel, N., Savoldi, L., Zanino, R., 2017, "Characterization of Particle Flow in a Free-Falling Solar Particle Receiver", Journal of Solar Energy Engineering, 139(2), p. 021011 (9 pages). DOI: 10.1115/1.4035258

[14] Mills, B.H., Ho, C.K., Schroeder, N.R., Shaeffer, R., Laubscher, H.F., Albrecht, K.J., 2022, "Design Evaluation of a Next-Generation High-Temperature Particle Receiver for Concentrating Solar Thermal Applications", Energies, 15(5), p. 1657. DOI: 10.3390/en15051657

[15] Brilliantov, N.V., Spahn, F., Hertzsch, J.-M., Pöschel, T., 1996, "Model for collisions in granular gases", Physical Review E, 53(5), pp. 5382-5392. DOI: 10.1103/PhysRevE.53.5382

[16] Mindlin, R.D., 2021, "Compliance of Elastic Bodies in Contact", Journal of Applied Mechanics, 16(3), pp. 259-268. DOI: 10.1115/1.4009973

[17] Luding, S., 2008, "Cohesive, frictional powders: contact models for tension", Granular Matter, 10(4), pp. 235-246. DOI: 10.1007/s10035-008-0099-x

[18] Zhong, H., Lan, X., Gao, J., Zheng, Y., Zhang, Z., 2015, "The difference between specularity coefficient of 1 and no-slip solid phase wall boundary conditions in CFD simulation of gas–solid fluidized beds", Powder Technology, 286, pp. 740-743. DOI: 10.1016/j.powtec.2015.08.055

[19] Saeed, R.S., Saleh, N.S., Alaqel, S., Djajadiwinata, E., Alswaiyd, A., El-Leathy, A., Danish, S.N., Al-Ansary, H., Almutairi, Z., Al-Suhaibani, Z., Sarfraz, M., Jeter, S., 2023, "Frictional characterization of different particulate materials to be used in concentrated solar power system", AIP Conference Proceedings, 2815(1), p. 020013. DOI: 10.1063/5.0149173

[20] Chen, H., Xiao, Y.G., Liu, Y.L., Shi, Y.S., 2017, "Effect of Young's modulus on DEM results regarding transverse mixing of particles within a rotating drum", Powder Technology, 318, pp. 507-517. DOI: 10.1016/j.powtec.2017.05.047

[21] Yan, Z., Wilkinson, S.K., Stitt, E.H., Marigo, M., 2015, "Discrete element modelling (DEM) input parameters: understanding their impact on model predictions using statistical analysis", Computational Particle Mechanics, 2(3), pp. 283-299. DOI: 10.1007/s40571-015-0056-5

DISTRIBUTION

Email—Internal

Name	Org.	Sandia Email Address
Brantley Mills	1514	bramill@sandia.gov
Flint Pierce	1514	fpierce@sandia.gov
Leslie Phinney	1514	lmphinn@sandia.gov
Shaker Saeed Mohammed Alaqel	8923	ssabdul@sandia.gov
Margaret Gordon	8923	megord@sandia.gov
Matthew Sandlin	8923	mjsandl@sandia.gov
Nathan Schroeder	8923	nrschro@sandia.gov
Jeremy Sment	8923	jsment@sandia.gov
Aaron Spieles	8923	ajspiel@sandia.gov
Technical Library	1911	sanddocs@sandia.gov

Email—External

Name	Company Email Address	Company Name
Kamala Raghaven	kamala.raghavan@ee.doe.gov	SETO
Rajgopal Vijaykumar	rajgopal.vijaykumar@ee.doe.gov	SETO
Hany Al-Ansary	hansary@ksu.edu.sa	KSU
Eldwin Djajadiwinata	eldwin.dj@gmail.com	KSU
Rageh S. Saeed	rajehsaad@yahoo.com	KSU

This page left blank

Sandia National Laboratories is a multimission laboratory managed and operated by National Technology & Engineering Solutions of Sandia LLC, a wholly owned subsidiary of Honeywell International Inc. for the U.S. Department of Energy's National Nuclear Security Administration under contract DE-NA0003525.